Karlsruhe Institute of Technology

Institut für Theoretische Festkörperphysik

T-matrix Method for the Analysis of Electromagnetic Scattering

Zur Erlangung des akademischen Grades eines Doktors

der Naturwissenschaften (Dr. rer. nat)

von der KIT- Fakultät für Physik

des Karlsruher Instituts für Technologie (KIT)

genehmigte Dissertation

Von

M.Sc. Radius Nagassa Setyo Suryadharma

am Institut für Theoretische Festkörperphysik

Datum der mündlichen Prüfung :26-07-2019

Referent : Prof. Dr. Carsten Rockstuhl

Koreferent : Prof. Dr. Heinz Kalt

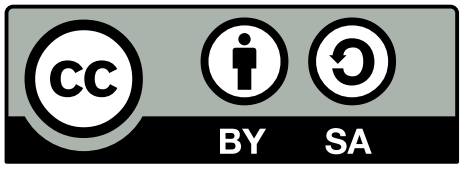

I hereby certify that the work presented in this dissertation, to the best of my knowledge and belief, is original, unless otherwise acknowledged in the text. I have not presented this work, either in whole or part, to a different examination board previously.

Karlsruhe, 10.07.2019,

(Radius Nagassa Setyo Suryadharma)

Abstract

How to analyze optical scattering properties of an object or an ensemble of objects? It is often a nontrivial task to answer this question. There exists analytical formulas to calculate the scattering response of a simple object for a given illumination, and several numerical methods for more complicated structure can be used for the same purpose. However, probing the response of an object for one particular illumination scenario does not give the full picture as, in principle, there can be an infinite number of possible illumination scenarios. It is therefore a tedious task to consider all possible illumination scenarios to analyze the scattering properties of an object. To complicate the problem further, for an ensemble of randomly located and randomly oriented particles, it is almost impossible to predict exactly the response of the entire ensemble, and statistical means to extract observables quantities are needed.

To solve these problems, we rely in this thesis on a modal analysis of the T-matrix of the scatterer to analyze the optical scattering properties of a single object independent from a specific illumination. We also develop means to predict experimentally observables quantities of an ensemble of randomly oriented particles and analyze them in the context of modes sustained by its constituent scatterer. Furthermore, an analysis in the context of an effective medium theory will be used to analyze the sensitivity of a hybrid optical sensor made from a dielectric disk covered with nanoparticles.

The entire work relies on a framework for the modal analysis to analyze scattering properties of an object. To extract the modes from the T-matrix of the considered object, two spectral decompositions of a matrix will be presented. The first spectral decomposition, eigenvalue decomposition, is used to analyze the scattering properties of several objects. Using local and global coordinates formalisms, we show that complementary information can be obtained. To be able to discuss both approaches on the same level, a single, unified theory, to put both formalisms on the same ground will also be presented. This is done by a transformation formalism that converts eigenmodes in local coordinates into eigenmodes in global coordinates and *vice versa*. The second spectral decomposition, singularvalue decomposition, offers orthogonal modes, which in general cannot be provided by the modes obtained from eigenvalue decomposition. The orthogonality is beneficial to design an appropriate incident field for a desired optical response of a scatterer.

After we are done with the scattering analysis of a single particles, we proceed to analyze the optical response of an ensemble of randomly located and randomly oriented scatterers. To simplify the problem, we assume a very diluted solution in our analysis. We show that the experimentally observables quantities can be derived directly from the scattering properties of the constituent scatterer.Starting from this insights, we show that Fano properties, which arise from the coupling between nonorthogonal modes, can be identified in a strightforward manner from the experimentally observable quantities of the ensemble.

In the last part of this thesis, an analysis of an ensemble of nanoparticles around a microdisk is presented. Here, we focus our discussion on the sensitivity of such system, which shows a better performance compared to the traditional full coating approach, making it a promising structure to be used in optical sensing device.

In summary, we presented a theoretical framework to analyze the optical response of an object or ensemble of objects and its possible applications.

Contents

List of Figures

Publications

Publications whose contents are part of this thesis are highlighted in bold.

P.1 **R. N. S. Suryadharma, M. Fruhnert, C. Rockstuhl, and I. Fernandez-Corbaton, "Singular-value decomposition for electromagnetic-scattering analysis", *Physical Review A*, vol. 95 no. 5 p. 053834, 2017.**

P.2 **R. N. S. Suryadharma, M. Fruhnert, I. Fernandez-Corbaton, and C. Rockstuhl, "Studying plasmonic resonance modes of hierarchical self-assembled meta-atoms based on their transfer matrix", *Physical Review B*, vol. 96 no. 4 p. 045046, 2017.**

P.3 **C. Klusmann, R. N. S Suryadharma, J. Oppermann, C. Rockstuhl, and H. Kalt, "Hybridizing whispering gallery modes and plasmonic resonances in a photonic metadevice for biosensing applications", *Journal of the Optical Society of America B*, vol. 34 no. 7 p. D-46-D55, 2017.**

P.4 **R. N. S. Suryadharma and C. Rockstuhl, "Predicting observable quantities of self-assembled metamaterials from the T-Matrix of its constituting meta-atom", *Materials*, vol. 11 no. 2. p. 213, 2018.**

P.5 M. Baginski, E. Tomczyk, A. Vetter, R. N. S. Suryadharma, C. Rockstuhl, and W. Lewandowski, "Achieving highly stable, reversibly reconfigurable plasmonic nanocrystal superlattices through the use of semifluorinated surface ligands", *Chemistry of Materials*, vol. 30 no.22 p.8201-8210, 2018.

P.6 A. Rahimzadegan, D. Arslan, R. N. S. Suryadharma, S. Fasold, M. Falkner, T. Pertsch, I. Staude, and C. Rockstuhl, "Disorder-induced phase transitions in the transmission of dielectric metasurfaces", *Physical Review Letters*, vol. 122 no. 1 p. 015702, 2019.

P.7 **R. N. S. Suryadharma, C. Rockstuhl, O. J. F. Martin, and I. Fernandez-Corbaton, "Quantifying Fano properties in self-assembled metamaterials", *Physical Review B*, vol. 99 no. 19 p. 195416, 2019.**

P.8 M.Symeonidis, R. N. S. Suryadharma, R. Grillo, A. Vetter, T. Scharf, C. Rockstuhl and T. Bürgi, "High-resolution interference microscopy with spectral resolution for the characterization of individual particles and self-assembled meta-atoms ", *Submitted to Optics Express*, 2019.

Conference Contributions

Conference contributions with presentation done by myself are highlighted in bold.

C.1 S. A. Schmid, R. N. S. Suryadharma, M. Fruhnert, C. Klusmann, H. Kalt, and C. Rockstuhl, "Studying the interplay of nanoparticles and dielectric whispering gallery mode resonators using a generalized Mie theory", *DPG Spring Meeting: Dielectric Solids Division 2016*, Regensburg, Germany, March 2016.

C.2 **R. N. S. Suryadharma, M. Fruhnert, I. Fernandez-Corbaton, and C. Rockstuhl, "Multipolar eigenmodes analysis of meta-atom", *DokDok 2016*, Oppurg, Germany, September 2016.**

C.3 C. Klusmann, S. A. Schmid, R. N. S. Suryadharma, C. Rockstuhl,and H. Kalt, "Studying the interplay of nanoparticles and dielectric whispering gallery mode resonators using a generalized Mie theory", *DPG Spring Meeting: Dielectric Solids Division 2017*, Dresden, Germany, March 2017.

C.4 M. Fruhnert, R. N. S. Suryadharma, A. Rahimzadegan, C. Rockstuhl and I. Fernandez-Corbaton, "Studying the Properties of Self-assembled Meta-atoms Based on Their T-matrix", *Meta Conference 2017*, Incheon, South Korea, July 2017.

C.5 **R. N. S. Suryadharma, M. Fruhnert, I. Fernandez-Corbaton and C. Rockstuhl, "Modal Analysis of Meta-atom using T-matrix approach", *International Congress on Artificial Materials for Novel Wave Phenomena Metamaterials 2017*, Marseille, France, August 2017.**

C.6 **R. N. S. Suryadharma and C. Rockstuhl, "Predicting Observable Quantities of Self-Assembled Metamaterials from the T-Matrix of Its Constituting Meta-Atoms", *International Congress on Artificial Materials for Novel Wave Phenomena Metamaterials 2018*, Espoo, Finland, August 2018.**

C.7 M. Symeonidis, R. Nagassa, R. Grillo, T. Scharf, C. Rockstuhl, T. Bürgi, "Engineered nanostructures characterisation by spectral interferometric microscopy", *SPIE OPTO 2019*, San Francisco, United States, February 2019.

C.8 **R. N. S. Suryadharma and C. Rockstuhl, "Predicting Observable Quantities of Self-Assembled Metamaterials from the T-Matrix of Its Constituting Meta-Atoms", *12th Annual Meeting of Photonic Devices*, Berlin, Germany, February 2019.**

C.9 A. Rahimzadegan, D. Arslan, R. N. S. Suryadharma, S. Fasold, M. Falkner, T. Pertsch, I. Staude, and C. Rockstuhl, " Disorder Induced Phase Transition in an Optical Metasurface", *PIERS 2019*, Rome, Italy, June 2019.

Chapter 1

1 Introduction

How to understand light interaction with an ensemble of objects?
and
Can we get something out of it?

These are the two main questions, which I will try to answer throughout this thesis.

The behavior of light upon interaction with a scattering object is quite fascinating. Since ancient times, the interaction between light and matter has been very attractive from different perspectives for humankind. Shiny gemstones are one of the prime example of this fact, which attract many people, even until today. In the course of time, the art-driven approach to understand light has also been accompanied by a deeper understanding of the physics of light. Nowadays, the understanding of light propagation and scattering is one of the main cornerstones of current technology. Optical coherence tomography used as a medical imaging technology,[1,2] high speed optical communication used in telecommunication and data processing,[3–6]and optical sensing device for various purpose[7–11] are just a few examples of optics based technologies developed in the last few decades and which continue to impact our society.

To understand the light propagation and particularly its interaction with a scattering object, the concept of modes is a very powerful tool.[12–14] Technically speaking, a mode is an eigensolution of the corresponding equation that governs the evolution of the system in the absence of any source. In the context of light propagation and scattering, modes are the solution of the wave equation which express the propagation of light in a particular system. Modes are inherent properties of the system, and do not depend on the incident field impinging on the system. However, they can be excited due to coupling with an external incident field. In free space, for example, the associated modes obtained in a Cartesian coordinate system are elliptically polarized plane waves. Any solution to Maxwell's equations can be written as a linear superposition of these modes. The modes also have the great benefit to be analytically tractable. This means that we know the dispersion relation, which describes the evolution of the phase along a principle propagation direction, given that we know the frequency and the angles of propagation relative to that principle direction. This dispersion relation is of paramount importance as some effects, such as diffraction, are emerging features from the different phase accumulation of each plane wave.

However, the concept of modes is not only limited to free space. It can also be applied to non-homogenous media. One example are optical resonators. The understanding of the supported modes enabled us to understand the emission properties from lasers built from these resonators.

In the context of the present thesis, the modes in a scattering situation are considered. Here, some material exists that is localized in its spatial extent and we can ask ourselves, what are the eigenmodes to Maxwell's equations in such situation. As we will see, their understanding will be decisive to explain the features that emerge in the scattering process. Generally, it can be said that understanding the modes of the system translates to understanding the response of the system.

Based on the understanding of the interaction of light and matter, materials with exotic properties that cannot be found in nature in the same frequency range can be designed.[15–20] A prime example would be a bulk material exhibiting magnetic properties at optical frequency. While such material is not available in nature, it can be designed based on the understanding of the modes sustained by the scattering entities from which the material is built. First, one can start by engineering a scatterer to have a dominant magnetic dipole moment using a suitable modal analysis. Ideally, that mode should be excitable from all illumination directions with the same strength, which would imply an isotropy in the scattering responses. After understanding the response of a single scatterer, many of these engineered scatterers can be arranged periodically to obtain a bulk material. In this way, a bulk material with magnetic properties at optical frequency is at hand. The ability to design a desired material property from the level of the individual scatterer, as given in the previous example, opens a plethora of applications previously thought to be impossible. These designed materials are often called metamaterials. These materials usually consist of an ensemble of building blocks, the so called meta-atom. The terminology has been derived in analogy to ordinary materials, that are made from an ensemble of atoms. Initially, metamaterials were frequently fabricated by a periodic arrangement of these meta-atoms and in most cases, top-down nanostructure technology were used. More often, this approach involves lithography techniques.[21–26]

With the advances in colloidal chemistry, metamaterials made from bottom-up techniques started to attract attention in recent years.[27–30] In contrast to top-down approaches, this method usually relies on minimizing the interaction energy between building blocks which form the meta-atom (such as potential energy between building blocks or binding energy of the molecules involved to create the desired meta-atom). Due to this energy minimization as its working principle, this bottom-up approach is often called a self-assembly approach. The attention can be explained partly by the fact that these self-assembled metamaterials can be fabricated in a rather simple way compared to their top-down counterparts and particularly bulk materials are easily at hand. The fabrication process is usually cheaper compared to metamaterials made from top-down approach. Since most often, the available meta-atoms are randomly distributed in space and the meta-atoms are randomly oriented inside a solution, the optical responses of metamaterials made from self-assembly approach are isotropic. All these aspects are quite appealing for a future exploration. However, bottom-up metamaterials have their limitations too. Their isotropic behavior comes at the expense of the uncertainty in the position of the meta-atoms and it is also challenging to obtain metamaterials with a high particle density that allows to encounter the desired dispersion in the material properties of interest. Also, most often, the meta-atom itself can only be fabricated from highly symmetric objects, such as spheres. This lowers the abilities to control the optical response on demand. These facts

are in stark contrast to metamaterials fabricated with a top-down aproach, where the positions of the meta-atoms can be controlled up to few nanometers precision[31–33] and they offer great flexibility to fabricate the shape of meta-atoms upon request.[34,35]

With such rapid progress in fabrication technologies (both top-down and bottom-up approaches), it became clear that the ability to predict the response of the metamaterials is needed. We saw that, in general, metamaterials can be divided into two categories: Periodic structures which are usually fabricated using top-down approaches and isotropic structures which are usually fabricated using bottom-up approaches. The computational method used to predict the response of a given metamaterials depends on their structural form. For periodic structures, the plane wave expansion method[36,37] and finite element method using periodic boundary conditions[38] proved to be quite popular for calculating the response of the associated metamaterials. On the other hand, for a single scatterer or an non periodic ensemble of scatterers, several methods are available. Surface integral method,[39] discrete dipole approximation,[40] finite element method with open boundary condition,[41] and T-matrix method[42] can be used in this case. All of these methods give the ability to predict the response of metamaterials, although an appropriate choice needs to be made depending on the structural form of the desired metamaterials, as previously mentioned before. However, for the case of metamaterials made from self-assembly approaches, it remains an open problem to explain the response from these materials in terms of modes, due to the associated randomness of its constituent meta-atoms. The investigation of this aspect is one of the major goals of this thesis.

The ability to design and fabricate metamaterials brings plethora of new ideas for applications. Among them are perfect absorbers,[43–45] chiral metamaterials for various applications,[46–48] data transfer channels,[49–51] electromagnetic cloaking concepts,[52–54] and sensing devices.[55–57] Among these examples, metamaterials based sensors are quite an interesting application. This is due to the fact that metamaterials can exhibit strong field localization and enhancement. These aspects were beneficial to improve the sensitivity when compared to traditional approaches to implement optical sensing devices. Several specific applications and associated designs have been suggested in the past few years. For example, by using metamaterials to replace metal parts in surface plasmon resonance sensors, an increase of sensing performance was demonstrated.[58] Another example is a novel method of dielectric sensing using epsilon near zero materials.[59] These two are prime examples of the application of metamaterials in sensing area.

Although new developments in sensing using metamaterials have been proposed, the traditional concept of an optical sensing device is still of great importance nowadays. This can be explained by the simple design of these traditional approaches compared to their metamaterials based counterparts that is much more desirable among sensing community and this extra work load in design, unfortunately, is not yet outperformed by the improvement of the performance by metamaterials based sensors. Among the traditional approaches often used in the sensing devices, whispering gallery mode based sensor is one of the prime example.[60] It was shown that a sensor based on a whispering gallery mode enabled the detection at the single molecule level of an IL2 protein[61] or even single viruses.[62] This ability even exceeds the state of the art sensitivity of other sensor, such as chemical based enzyme-linked immunosorbent assay.[63] Recently,

it even enabled the detection of binding event of molecules.[64] Based on these fact, it shows that the traditional concepts of optical sensing devices can offers quite plethora of promising applications. All together, a second goal of this thesis is to explore different sensing scenarios that occur in the context of these scattering process.

1.1 Content of the thesis

In this thesis, as mentioned in the previous section, we will try to answer the two questions presented at the beginning of this chapter. For this purpose, a basic theoretical foundation will be necessary. Therefore, we will dedicate chapter 2 solely to the fundamental concepts, which will be used later on. Since we are dealing with optical waves, it makes sense to depart from Maxwell's equations. From Maxwell's equations, we proceed with the discussion of light scattering at a spherical object. In this case, the incident and scattered fields can be expanded as a linear combination of several vector spherical harmonics with suitable amplitude coefficients.

The connection between scattered and incident field coefficients can be written naturally in form of a matrix operation. Here, the concept of a T-matrix is introduced. The T-matrix will be our main tool to answer the two questions presented at the beginning of this thesis. Due to this reason, it is important to understand the T-matrix in more detail and we continue our discussion with the T-matrix for various scattering scenarios. First, we explain how to calculate the T-matrix of an arbitrary object. This will be followed by the T-matrix formalism for multi-particle systems that allows to discuss the scattering from multiple objects. Different representations of the T-matrix in either local coordinates or global coordinates will be discussed. This is followed by a discussion of the T-matrix formalism when the scatterer is periodically arranged. This basically allows to predict reflection and transmission from an array of the scatterers, once their T-matrix is known. After the introduction of these T-matrix scenarios, we end chapter 2 with the introduction of the theoretical concept to homogenize large number of scatterer using Clausius-Mossoti effective medium theory.

After introducing the fundamental concepts, we move to the modal analysis in chapter 3. As mentioned in the previous section, the modal analysis plays an important role to understand the response of the scatterer. In this chapter, we will discuss modes obtained from the T-matrix of the scatterer. To extract the modes, two kinds of spectral decomposition of the T-matrix will be used. Eigenvalue decomposition decomposes the T-matrix into a set of eigenvalues and its corresponding eigenvectors. We will also discuss the different modes in local coordinates and global coordinate, and pinpoint the advantage and disadvantage of both approaches. This will be followed by a way to transform eigenmodes from local coordinates to global coordinates, and *vice versa*.

After we have accomplished the eigenvalue decomposition, another spectral decomposition, singular value decomposition, is used to extract modes. The main advantage of this method compared to the latter is the fact that singular values always form an orthonormal basis set. However, contrary to eigenvalue decomposition, the singular modes of incident and scattered

fields are, in general, different. Finally, this section will end with the comparison between the modal decomposition obtained using singular value and eigenvalue decompositions of the T-matrix. The results presented in this chapter will serve as tools to understand the response of the scatterer in terms of modes.

Having done the analysis of a single meta-atom, in chapter 4, the response of metamaterials fabricated with a self-assembled approach, which consists of many meta-atoms, will be the main focus. As mentioned in the previous section, the main advantage of metamaterials made from self-assembly method is their isotropy. This is due to the fact that its response does not depend on the direction of the incident field. Since the metamaterials consist of a large number of meta-atoms with different orientation, an averaging method is required to extract the response of any experimentally observable quantity, such as circular dichroism. By extracting the information directly from its T-matrix constituent, we show a fast and direct way to predict the observables directly from the T-matrix of its individual meta-atoms, without the need to do manual averaging.

Armed with this technical expertise and the ability to discuss the response of meta-atoms in terms of modes extracted from the T-matrix as described in chapter 3, we continue with a discussion of Fano resonances and a way to quantify them in the context of self-assembled metamaterials. Here, due to the fact that Fano resonances usually are described as coupling between different modes, we introduce a mode cross coupling parameter to quantify the Fano contribution to the observable response. The results presented here will allow to design isotropic metamaterials, which can be used for various purposes.

In the last chapter, i.e. chapter 5, we discuss another application of the T-matrix method. Here, we will explore the functionality of optical sensing devices. We start by first introducing several parameters related to optical sensors. In continuation from these basics, we analyze the sensing performance of dielectric resonators that sustain whispering gallery modes. With such whispering gallery modes, a high quality factor can be achieved, which is very beneficial to assure a good readout of the optical resonances. This, however, comes at the expense of a small sensitivity. In an extension, we describe afterwards optical sensors based on metallic nanoparticle that support the excitation of localized surface plasmon polaritons. Contrary to dielectric based resonators, better sensitivity can be achieved at the expense of a lower quality factor.

Based on the previous two distinct systems, we continue the discussion by combining both resonators in a hybrid system. We show that an engineering trade-off exists between readability and sensitivity. We focus on a system where a whispering gallery mode sustained by a microdisk hybridizes with a localized surface plasmon polariton sustained by gold nanoparticles. We show that the sensitivity of the system can be enhanced compared to the bare microdisk resonator.

After a lengthy discussion with the aim to answer the two questions presented in the beginning, the last chapter will be dedicated to conclude our discussion and will provide a short outlook to further fields of applications, which can benefit from the methods developed in this thesis.

Chapter 2

2 Theoretical Background

In this chapter, we will introduce several important theoretical aspects that will be used later on in this thesis. In the first section, we will present the linear scattering problem of an electromagnetic field by a sphere. The scattering of the electromagnetic field is a direct consequence of the interface conditions between two different materials. This fact can be deduced directly from Maxwell's equations, which govern the interaction between light and matter. By expanding the field in an appropriate basis set which satisfies the orthogonality condition, the scattering of an object can be expressed conveniently in form of a matrix operation. The matrix operator, which links the incident and the scattered field coefficients, will be called the T-matrix. This matrix will be the main working engine of this thesis. Following the introduction of the T-matrix, we will continue our discussion with the procedure to calculate the T-matrix of an arbitrary object by considering multiple illumination scenarios.

In principle, the T-matrix can be used to describes the scattering of light at multiple objects. This fact will be the main focus of the second section. Here, the addition theorem, which transforms the basis set in one coordinate system into the basis set in another coordinate system, will be the main tool used to formulate the multiple scattering formalism in the local coordinate system of each scatterer. With this description, the T-matrix in local coordinates, which links the original incident and the scattered fields at each individual scatterer, can be defined in a straightforward way. This will be followed by the transformation of the T-matrix in local coordinates into the T-matrix in global coordinates, and *vice versa* using the addition theorem of the respective basis set.

Finally, we will dedicate the last section of this chapter to describes an effective medium approach. Here, the main emphasis will be given to Clausius-Mossoti effective medium theory, which will be used in the later chapters.

2.1 Scattering of an electromagnetic field by a spherical object

In this section, we will review the Maxwell equations and the interface conditions for an electromagnetic field. Afterwards, the solution for the scattering of an incident field by a spherical object will be discussed. For this purpose, Vector Spherical Harmonics (VSHs), which form an orthogonal basis set, appear naturally as the eigensolutions of Maxwell's equation in a spherical coordinate system. Finally, we will introduce the T-matrix notation for the scattering problem by a sphere.

2.1.1 Maxwell's equations and the interface conditions of electromagnetic fields

Scattering of light is basically an electromagnetic wave phenomenon. As most of the electromagnetic phenomena can be described accurately by Maxwell's equations, we will dedicate this section to take a look back at Maxwell's equations, which will be the cornerstone of our theoretical foundations later on.

Maxwell's equations in a homogenous medium are:

$$\begin{aligned} \nabla \cdot \widetilde{\mathbf{D}}(\mathbf{r},t) &= \rho(\mathbf{r},t), \quad \nabla \times \widetilde{\mathbf{E}}(\mathbf{r},t) = -\frac{\partial \widetilde{\mathbf{B}}(\mathbf{r},t)}{\partial t}, \\ \nabla \cdot \widetilde{\mathbf{H}}(\mathbf{r},t) &= 0, \qquad\quad \nabla \times \widetilde{\mathbf{H}}(\mathbf{r},t) = \widetilde{\mathbf{J}}(\mathbf{r},t) + \frac{\partial \widetilde{\mathbf{D}}(\mathbf{r},t)}{\partial t}, \end{aligned} \tag{2.1}$$

where $\widetilde{\mathbf{E}}(\mathbf{r},t)$, $\widetilde{\mathbf{H}}(\mathbf{r},t)$, $\widetilde{\mathbf{D}}(\mathbf{r},t)$, and $\widetilde{\mathbf{B}}(\mathbf{r},t)$ denote the electric field, magnetic field, electric flux density, and magnetic flux density, respectively. $\mathbf{r}$ and t denote the position and time dependency, while the source terms $\widetilde{\mathbf{J}}(\mathbf{r},t)$ and $\rho(\mathbf{r},t)$ denote current and charge density.[65] We use the symbol $\widetilde{\cdot}$ to denote the time functional dependency of a function.

By Fourier transforming the time dependency t into its reciprocal space ω, i.e. $\widetilde{\mathbf{E}}(\mathbf{r},t) = \int \mathbf{E}(\mathbf{r},\omega)e^{-i\omega t}d\omega$, we can recast Maxwell's equations in frequency domain as:

$$\begin{aligned} \nabla \cdot \mathbf{D}(\mathbf{r},\omega) &= \rho(\mathbf{r},\omega), \quad \nabla \times \mathbf{E}(\mathbf{r},\omega) = i\omega\mathbf{B}(\mathbf{r},\omega), \\ \nabla \cdot \mathbf{H}(\mathbf{r},\omega) &= 0, \qquad\quad \nabla \times \mathbf{H}(\mathbf{r},t) = \mathbf{J}(\mathbf{r},\omega) - i\omega\mathbf{D}(\mathbf{r},\omega). \end{aligned} \tag{2.2}$$

To link the magnetic and electric field densities, the constitutive relations are needed. These relations, for a linear, isotropic, local and dispersive media, are:

$$\mathbf{D}(\mathbf{r},\omega) = \varepsilon(\mathbf{r},\omega)\mathbf{E}(\mathbf{r},\omega), \quad \mathbf{B}(\mathbf{r},\omega) = \mu(\mathbf{r},\omega)\mathbf{H}(\mathbf{r},\omega), \tag{2.3}$$

where $\varepsilon(\mathbf{r},\omega)$ and $\mu(\mathbf{r},\omega)$ are the permittivity and permeability of the material. By plugging these constitutive relations into Maxwell's equations, and by assuming a homogenous medium with no additional currents or charges present as a source, the following Helmholtz equations can be derived:

$$\nabla^2\mathbf{E}(\mathbf{r},\omega) + k^2(\omega)\mathbf{E}(\mathbf{r},\omega) = 0, \tag{2.4}$$

$$\nabla^2\mathbf{B}(\mathbf{r},\omega) + k^2(\omega)\mathbf{B}(\mathbf{r},\omega) = 0, \tag{2.5}$$

where $k(\omega)$ is the wavevector of the electromagnetic field, defined as:

$$k^2(\omega) = \omega^2\varepsilon(\omega)\mu(\omega). \tag{2.6}$$

Usually, it is much more convenient to write the relative permittivity, $\varepsilon_\mathrm{r}(\omega)$, and relative permeability, $\mu_\mathrm{r}(\omega)$, with respect to the permittivity and permeability in vacuum, that is, $\varepsilon_\mathrm{r}(\omega) = \frac{\varepsilon(\omega)}{\varepsilon_0}$

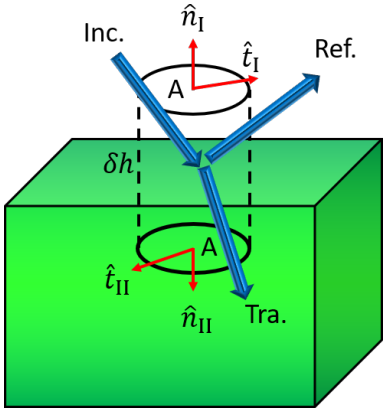

Figure 2.1 *An electromagnetic field propagating in different media, denoted by Inc., Ref., and Tra. for incident, reflected and transmitted field respectively. Here* $\hat{\mathbf{n}}$ *and* $\hat{\mathbf{t}}$ *denote normal and tangential components of the field, while the subscripts 1 and 2 denote the medium. A is the area of integration described in eq. 2.7 and the volume in the corresponding equation is denoted by* $V = \delta h \times A$.

and $\mu_r(\omega) = \frac{\mu(\omega)}{\mu_0}$, where the subscript 0 denotes the value in vacuum. Throughout the following discussions, we will refer to $\varepsilon_r(\omega)$ and $\mu_r(\omega)$ as $\varepsilon(\omega)$ and $\mu(\omega)$ respectively. This will simplify the notation used in this thesis.

In reality, the infinite homogenous medium never exists. For this reason, ones need to solve Maxwell's equations with physical parameters $\varepsilon(\omega)$ and $\mu(\omega)$ which depend on the spatial position. This can be a very tedious task to do directly. To simplify the problem, one can decompose the entire space into several discrete spatial domains in which the material indeed is homogenous. Then, the fields in the media adjacent to the interface are linked by certain equations. These linking equations can be obtained by applying Green's and Stokes's theorems to the Maxwell equations, which result in the integral form of Maxwell's equations. For a source-free medium, they are:

$$\begin{aligned} \oint_S \mathbf{D}(\mathbf{r},\omega)\cdot d\mathbf{A} &= 0, \\ \oint_S \mathbf{B}(\mathbf{r},\omega)\cdot d\mathbf{A} &= 0, \\ \oint_S \mathbf{E}(\mathbf{r},\omega)\cdot d\mathbf{l} &= \iint i\omega\mathbf{B}(\mathbf{r},\omega)\cdot d\mathbf{A}, \\ \oint_S \mathbf{H}(\mathbf{r},\omega)\cdot d\mathbf{l} &= \iint i\omega\mathbf{D}(\mathbf{r},\omega)\cdot d\mathbf{A}, \end{aligned} \tag{2.7}$$

where $\mathbf{A}$ and $\mathbf{l}$ denote the area and the line of the integration,respectively.

Now, consider two semi-infinite medium as described in Fig. 2.1. We need to inspect Eqs. 2.7 and apply them to the situation sketched in Fig. 2.1. By considering the case of a very thin cylinder, that is, $\delta h \to 0$, the following continuity equations, which govern the field at the

interface between two media, can be deduced:

$$\begin{aligned}
\mathbf{E}_{\mathrm{I}}^{\hat{\mathrm{t}}}(\mathbf{r}_0,\omega) - \mathbf{E}_{\mathrm{II}}^{\hat{\mathrm{t}}}(\mathbf{r}_0,\omega) &= 0,\\
\mathbf{D}_{\mathrm{I}}^{\hat{\mathrm{n}}}(\mathbf{r}_0,\omega) - \mathbf{D}_{\mathrm{II}}^{\hat{\mathrm{n}}}(\mathbf{r}_0,\omega) &= \sigma_{\mathrm{s}},\\
\mathbf{B}_{\mathrm{I}}^{\hat{\mathrm{n}}}(\mathbf{r}_0,\omega) - \mathbf{B}_{\mathrm{II}}^{\hat{\mathrm{n}}}(\mathbf{r}_0,\omega) &= 0,\\
\mathbf{H}_{\mathrm{I}}^{\hat{\mathrm{t}}}(\mathbf{r}_0,\omega) - \mathbf{H}_{\mathrm{II}}^{\hat{\mathrm{t}}}(\mathbf{r}_0,\omega) &= j_{\mathrm{s}}.
\end{aligned} \tag{2.8}$$

where the superscript $\hat{t}$ and $\hat{n}$ denote the tangential and normal components of the associated field. Here, σ_{s} and j_{s} denote surface charge and current density, respectively. As can be seen from the sketch in Fig. 2.1, the field in region I and II are:

$$\begin{aligned}
\mathbf{S}_{\mathrm{I}}(\mathbf{r}_0,\omega) &= \mathbf{S}_{\mathrm{Inc}}(\mathbf{r}_0,\omega) + \mathbf{S}_{\mathrm{Ref}}(\mathbf{r}_0,\omega),\\
\mathbf{S}_{\mathrm{II}}(\mathbf{r}_0,\omega) &= \mathbf{S}_{\mathrm{Tra}}(\mathbf{r}_0,\omega).
\end{aligned} \tag{2.9}$$

Here, $\mathbf{S}(\mathbf{r}_0,\omega)$ can be either electric, magnetic, electric flux density or magnetic flux density, depending on the equation described in Eq. 2.8.

2.1.2 Mie theory

After discussing Maxwell's equations and the interface conditions, in this section we will discuss the most simple 3D case of a scattering problem: scattering by a spherical object. For this, one needs to solve the Maxwell equations in a spherical coordinate system. The solutions in this coordinate system are called vector spherical harmonics (VSH), $\mathbf{M}_{\mathrm{mnk}}^{(\mathrm{i})}(\mathbf{r},\omega)$. These solutions are:[65]

$$\mathbf{M}_{\mathrm{mn1}}^{(\mathrm{i})}(\mathbf{r},\omega) = \nabla \times \mathbf{r}\psi_{\mathrm{mn}}^{(\mathrm{i})}(\mathbf{r},\omega), \tag{2.10}$$

$$\mathbf{M}_{\mathrm{mn2}}^{(\mathrm{i})}(\mathbf{r},\omega) = \frac{1}{k}\nabla \times \mathbf{M}_{\mathrm{mn1}}^{(\mathrm{i})}(\mathbf{r},\omega), \tag{2.11}$$

where:

$$\psi_{\mathrm{mn}}(\mathbf{r},\omega) = e^{i\mathrm{m}\phi} \cdot P_{\mathrm{n}}^{\mathrm{m}}(\cos\theta) \cdot z_{\mathrm{n}}^{(\mathrm{i})}(kr). \tag{2.12}$$

Here, n is a positive integer number and m is an integer number which can take values between -n to n. The superscript denotes the choice of the radial spherical function, either spherical Bessel (superscript 1) or spherical Hankel (superscript 3) function. $P_{\mathrm{n}}^{\mathrm{m}}$ denotes the associated Legendre function, k is the wavenumber in the respective medium, and ϕ and θ are the azimuthal and the polar angles, respectively. Since VSHs form an orthogonal basis set, any field can be written as a linear superposition of this basis set. For a scattering problem, one is interested in the scattered field for a given incident field. As previously mentioned, by using the fact that the VSH are orthogonal basis set, the scattered and the incident fields can be

decomposed as:

$$\mathbf{E}_{\mathrm{sca}}(\mathbf{r},\omega) = \sum_{\mathrm{p}=1}^{2}\sum_{\mathrm{n}=1}^{\mathrm{N}}\sum_{\mathrm{m}=-\mathrm{n}}^{\mathrm{n}} a_{\mathrm{mnp}}\mathbf{M}^{(3)}_{\mathrm{mnp}}(\mathbf{r},\omega), \tag{2.13}$$

$$\mathbf{E}_{\mathrm{inc}}(\mathbf{r},\omega) = \sum_{\mathrm{p}=1}^{2}\sum_{\mathrm{n}=1}^{\mathrm{N}}\sum_{\mathrm{m}=-\mathrm{n}}^{\mathrm{n}} p_{\mathrm{mnp}}\mathbf{M}^{(1)}_{\mathrm{mnp}}(\mathbf{r},\omega). \tag{2.14}$$

Here, a_{mnp} and p_{mnp} denote the linear coefficients used to expand the scattered and the incident fields, and p denotes the parity of the VSH function, where $p = 1$ ($p = 2$) denote the electric (magnetic) response of the scatterer. Using these expressions, the optical cross-sections of the scatterer can be written in very convenient forms:[66]

$$\sigma_{\mathrm{sca}} = \frac{4\pi}{k_{\mathrm{b}}^2}\sum_{\mathrm{p}=1}^{2}\sum_{\mathrm{n}=1}^{\mathrm{N}}\sum_{\mathrm{m}=-\mathrm{n}}^{\mathrm{n}} |a_{\mathrm{mnp}}|^2, \tag{2.15}$$

$$\sigma_{\mathrm{ext}} = \frac{4\pi}{k_{\mathrm{b}}^2}\sum_{\mathrm{p}=1}^{2}\sum_{\mathrm{n}=1}^{\mathrm{N}}\sum_{\mathrm{m}=-\mathrm{n}}^{\mathrm{n}} \mathrm{Re}\left(p^*_{\mathrm{mnp}}a_{\mathrm{mnp}}\right), \tag{2.16}$$

$$\sigma_{\mathrm{abs}} = \sigma_{\mathrm{ext}} - \sigma_{\mathrm{sca}}, \tag{2.17}$$

where σ_{sca}, σ_{ext} σ_{abs} are the scattering, extinction and absorption cross-sections, respectively. k_{b} denotes the wavenumber in the medium where the cross-sections are calculated.[66]

For the simple case under consideration, i.e. scattering by a sphere, there exists an analytical solutions for the expansion coefficients of the scattered field. By applying the interface conditions expressed in Eq. 2.8, the following relation can be derived:[67]

$$a_{\mathrm{mnp}} = A_{\mathrm{np}}p_{\mathrm{mnp}}, \tag{2.18}$$

where

$$A_{\mathrm{np}}(\omega) = \frac{\mu_{\mathrm{sph}}e_{\mathrm{p}}^2 z_{\mathrm{n}}^{(1)}(\eta x)[x z_{\mathrm{n}}^{(1)}(x)]' - \mu_{\mathrm{sph}} z_{\mathrm{n}}^{(1)}(x)[\eta x z_{\mathrm{n}}^{(1)}(\eta x)]'}{\mu_{\mathrm{b}}e_{\mathrm{p}}^2 z_{\mathrm{n}}^{(1)}(\eta x)[x z_{n}^{(3)}(x)]' - \mu_{\mathrm{sph}} z_{\mathrm{n}}^{(3)}(x)[\eta x z_{\mathrm{n}}^{(1)}(\eta x)]'}, \tag{2.19}$$

$$x = \frac{\omega}{c}\sqrt{\varepsilon_{\mathrm{b}}(\omega)\mu_{\mathrm{b}}(\omega)}R, \tag{2.20}$$

$$\eta = \sqrt{\frac{\varepsilon_{\mathrm{sph}}(\omega)\mu_{\mathrm{sph}}(\omega)}{\varepsilon_{\mathrm{b}}(\omega)\mu_{\mathrm{b}}(\omega)}}, \tag{2.21}$$

$$e_{\mathrm{p}} = \begin{cases} \eta & \mathrm{p} = 1, \\ 1 & \mathrm{p} = 2. \end{cases} \tag{2.22}$$

Here, subscript b and sph denote the background and sphere, and R denotes the radius of the sphere. Equation 2.18 can also be cast in a matrix form, yielding:

$$\begin{bmatrix} a_1 & 0 & \cdots & 0 & 0 \\ 0 & a_1 & & 0 & 0 \\ \vdots & & \ddots & & \vdots \\ 0 & 0 & 0 & b_{n-1} & 0 \\ 0 & 0 & 0 & 0 & b_n \end{bmatrix} \begin{pmatrix} p_{1,-1,1} \\ p_{1,0,1} \\ \vdots \\ p_{n-1,n,2} \\ p_{n,n,2} \end{pmatrix} = \begin{pmatrix} a_{1,-1,1} \\ a_{1,0,1} \\ \vdots \\ a_{n-1,n,2} \\ a_{n,n,2} \end{pmatrix}, \tag{2.23}$$

or in a more compact form:

$$\overline{T} \left| p \right\rangle = \left| a \right\rangle . \tag{2.24}$$

Here, $\overline{T}$ is called the T-matrix of the scatterer.[42] It links the incident and the scattered fields of an object. Note that, although we start our discussion with VSH, the basis set of the T-matrix can be any arbitrary orthogonal functions. In this thesis, however, we will focus in our discussion on the VSH as our basis set.

2.2 Scattering formalism of an arbitrary object

In the previous section, the formalism of the T-matrix for a single sphere has been described. In general, a T-matrix is an operator which links the incident field and the scattered field coefficients of a scatterer. It depends on the shape and material parameters, but it does not depend on the incident field. For this reason, the T-matrix provides a convenient way to describe the scattering behavior of any scatterer. It is, therefore, desirable to be able to compute the T-matrix of an arbitrary object. As opposed to a sphere considered in the previous section, it is very hard and almost impossible to get the analytical formula for the components of the T-matrix for any arbitrary structure. In this section, we will review a method to calculate the T-matrix using the known incident and scattered fields of an arbitrary object for some selected illuminations.[68]

Since the VSH form an orthogonal basis set, any arbitrary incident field hitting an object and its scattered field can be decomposed into VSH. To obtain the linear coefficients of the incident and the scattered field, it is necessary to project the corresponding field into the corresponding

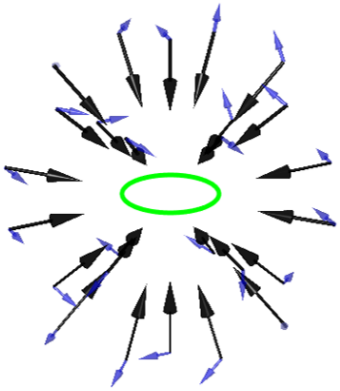

Figure 2.2 *Schematic figure of illumination scenarios to obtain the T-matrix of an arbitrary object, a torus in this case. Here, an object is illuminated by several incident fields with different polarization (deep blue arrow) and wavevector (black arrow).*

VSH. In mathematical term,

$$a_{\mathrm{mnp}} = \frac{\int \mathbf{M}^{*(\mathrm{i})}_{\mathrm{mnp}}(\mathbf{r},\omega)\cdot\mathbf{E}(\mathbf{r},\omega)dA}{\int \mathbf{M}^{*(\mathrm{i})}_{\mathrm{mnp}}(\mathbf{r},\omega)\cdot\mathbf{M}^{(\mathrm{i})}_{\mathrm{mnp}}(\mathbf{r},\omega)dA}. \tag{2.25}$$

Here, A denotes any arbitrary area enclosing the scatterrer. By varying the incident field, as shown schematically in Fig. 2.2, and then calculating the coefficients of the scattered field and the incident field for different scenarios, the following matrix equation will hold:

$$\overline{T}\left(\begin{array}{cccc}\left|p^{1}\right\rangle & \left|p^{2}\right\rangle & \cdots & \left|p^{\mathrm{n}-1}\right\rangle & \left|p^{\mathrm{n}}\right\rangle\end{array}\right) = \left(\begin{array}{cccc}\left|a^{1}\right\rangle & \left|a^{2}\right\rangle & \cdots & \left|a^{\mathrm{n}-1}\right\rangle & \left|a^{\mathrm{n}}\right\rangle\end{array}\right) \tag{2.26}$$

$$\overline{T}\,\overline{p} = \overline{a}, \tag{2.27}$$

where $\left|p^{\mathrm{i}}\right\rangle$ and $\left|a^{\mathrm{i}}\right\rangle$ denote the VSH coefficients of the incident and the scattered fields for a particular illumination scenario i, respectively. Matrices $\overline{p}$ and $\overline{a}$ are matrices which contain $\left|p^{\mathrm{i}}\right\rangle$ and $\left|a^{\mathrm{i}}\right\rangle$. In general, as long as the number of rows of matrix $\overline{p}$ is larger than the number of rows of matrix $\overline{T}$, Eq. 2.27 is invertible, meaning that:

$$\overline{T} = \overline{a}\,\overline{p}^{R}, \tag{2.28}$$

where the superscript R denotes the right inverse of the matrix, $\overline{p}^{R} = \overline{p}^{\dagger}\left(\overline{p}\,\overline{p}^{\dagger}\right)^{-1}$.[69]

2.3 Scattering formalism of multiple objects

After the T-matrix of a single object is obtained, here we will show how to obtain the T-matrix of an ensemble of scatterers. For this purpose, we have to understand the scattering process of each individual scatterer inside the ensemble, which will be the main topic in section 2.3.1. The total response of the ensemble then can be deduced directly from its individual constituent by employing the translation operator from each local coordinate into a single coordinate system, which will be the main idea of section 2.3.2.

2.3.1 Local coordinates formalism

The scattering problem of a scatterer in an ensemble is technically the same as in the case of the scattering problem of single object in a homogenous media. The main difference lies in the incident field. In a homogenous media, the incident field only consists of the incident field that originated from the outside of the system. On the other hand, for a scatterer in an ensemble of scatterers, the scattered field from other scatterers need to be taken into account. This fact can be written in a mathematical form as:

$$\mathbf{E}_{\mathrm{inc}}^{\mathrm{tot,l}}(\mathbf{r},\omega) = \mathbf{E}_{\mathrm{inc}}^{\mathrm{ori,l}}(\mathbf{r},\omega) + \sum_{\mathrm{j}\neq\mathrm{l}} \mathbf{E}_{\mathrm{sca}}^{\mathrm{j}}(\mathbf{r},\omega). \tag{2.29}$$

Here, the superscript tot, ori, and sca denote the total incident, original incident field from outside ensemble and scattered field, respectively. The schematic representation of this fact can be seen in Fig. 2.3. The superscript l denotes the index of the scatterer. In the literature, there are many methods to solve multiple scattering problem, where the incident field on each particle can be written according to Eq. 2.29. Among them, Born approximation,[70,71] vector dyadic formalism using integral operator[72] and Green's function in multiple scattering theory[73] are some of the most commonly used ones. Here, we will focus ourselves on the T-matrix formalism as described in[74] and P.2.

The first important step is how to formulate the basis set, in our case, VSH, in a different coordinate system. This can be done using the addition theorem of VSH. To clarify the index used, here we spell out the parity index p described in the previous section, and rewrite our VSHs as:

$$\mathbf{M}_{\mathrm{mn1}}^{(\mathrm{i})}(\mathbf{r},\omega) = \mathbf{M}_{\mathrm{mn}}^{(\mathrm{i})}(\mathbf{r},\omega), \qquad \mathbf{M}_{\mathrm{mn2}}^{(\mathrm{i})}(\mathbf{r},\omega) = \mathbf{N}_{\mathrm{mn}}^{(\mathrm{i})}(\mathbf{r},\omega), \tag{2.30}$$

whereas the expansion coefficients are:

$$a_{\mathrm{mn1}} = a_{\mathrm{mn}}, \quad a_{\mathrm{mn2}} = b_{\mathrm{mn}}, \tag{2.31}$$

$$p_{\mathrm{mn1}} = p_{\mathrm{mn}}, \quad p_{\mathrm{mn2}} = q_{\mathrm{mn}}. \tag{2.32}$$

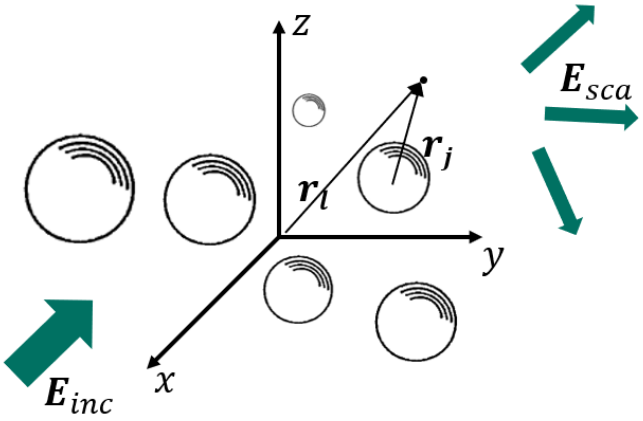

Figure 2.3 *The scattering of multiple objects. Here, the location of the center of mass of an object* j *relative to the origin of coordinate system is denoted by* $\mathbf{r}_\mathrm{j}$.

These relations mean that for a single scatterer, the associated T-matrix can be written as:

$$\begin{pmatrix} T_{11} & T_{12} \\ T_{21} & T_{22} \end{pmatrix} \begin{pmatrix} p \\ q \end{pmatrix} = \begin{pmatrix} a \\ b \end{pmatrix}. \tag{2.33}$$

The diagonal components, T_{11} and T_{22}, describe the transformation of VSH with the same parity (electric to electric and magnetic to magnetic), while the off diagonal components, T_{12} and T_{21}, describe the coupling between different parity (electric to magnetic and magnetic to electric).

The addition theorems for vector spherical harmonics are:[75–77]

$$\begin{aligned} \mathbf{M}^{(1)}_{\mathrm{nm}}(\mathbf{r}_\mathrm{j},\omega) &= \sum_{\nu}^{\infty}\sum_{\mu=-\nu}^{\nu} A^{\nu\mu}_{nm}(\mathrm{l},\mathrm{j},\omega)\mathbf{M}^{(3)}_{\nu\mu}(\mathbf{r}_\mathrm{l},\omega) + \mathrm{B}^{\nu\mu}_{\mathrm{nm}}(\mathrm{l},\mathrm{j},\omega)\mathbf{N}^{(3)}_{\nu\mu}(\mathbf{r}_\mathrm{l},\omega), \\ \mathbf{N}^{(1)}_{\mathrm{nm}}(\mathbf{r}_\mathrm{j},\omega) &= \sum_{\nu}^{\infty}\sum_{\mu=-\nu}^{\nu} B^{\nu\mu}_{nm}(\mathrm{l},\mathrm{j},\omega)\mathbf{M}^{(3)}_{\nu\mu}(\mathbf{r}_\mathrm{l},\omega) + \mathrm{A}^{\nu\mu}_{\mathrm{nm}}(\mathrm{l},\mathrm{j},\omega)\mathbf{N}^{(3)}_{\nu\mu}(\mathbf{r}_\mathrm{l},\omega), \end{aligned} \tag{2.34}$$

where $\mathbf{r}_\mathrm{l}$ and $\mathbf{r}_\mathrm{j}$ denote the position of the referential corrdinate system.

Technically speaking, these addition theorems can be seen as the transformation of VSHs from one coordinate system to VSHs in another coordinate system. Using this coordinate

transformation, the incident field coefficients at particle l therefore can be written as

$$\begin{aligned} P^{\mathrm{j}}_{\mathrm{nm}}(\omega) &= p^{\mathrm{j}}_{\mathrm{nm}}(\omega) - \sum_{\mathrm{l}\neq\mathrm{j}}^{U}\sum_{\nu=1}^{\infty}\sum_{\mu=-\nu}^{\nu} a^{\mathrm{l}}_{\nu\mu}(\omega)A^{\mathrm{nm}}_{\nu\mu}(\mathrm{l},\mathrm{j},\omega) + \mathrm{b}^{\mathrm{l}}_{\nu\mu}(\omega)\mathrm{B}^{\mathrm{nm}}_{\nu\mu}(\mathrm{l},\mathrm{j},\omega), \\ Q^{\mathrm{j}}_{\mathrm{nm}}(\omega) &= q^{\mathrm{j}}_{\mathrm{nm}}(\omega) - \sum_{\mathrm{l}\neq\mathrm{j}}^{\mathrm{U}}\sum_{\nu=1}^{\infty}\sum_{\mu=-\nu}^{\nu} a^{l}_{\nu\mu}(\omega)B^{\mathrm{nm}}_{\nu\mu}(\mathrm{l},\mathrm{j},\omega) + \mathrm{b}^{\mathrm{l}}_{\nu\mu}(\omega)\mathrm{A}^{\mathrm{nm}}_{\nu\mu}(\mathrm{l},\mathrm{j},\omega). \end{aligned} \tag{2.35}$$

Here, $P^{\mathrm{j}}_{\mathrm{nm}}$ and $Q^{\mathrm{j}}_{\mathrm{nm}}$ are the total incident field coefficients at scatterer j, and U is the total number of scatterer. to simplify the notation, we will drop the ω dependency in the argument of each variable, but bear in mind that each of them always depends on ω. The scattered field from each scatterer can be obtained by solving the self consistent equations:

$$\begin{aligned} a^{\mathrm{j}}_{\mathrm{nm}} &= \sum_{\alpha=1}^{\infty}\sum_{\beta=-\alpha}^{\alpha} T_{11}^{\mathrm{j},\alpha\beta\mathrm{nm}}P^{\mathrm{j}}_{\alpha\beta} + T_{12}^{\mathrm{j},\alpha\beta\mathrm{nm}}Q^{\mathrm{j}}_{\alpha\beta}, \\ b^{\mathrm{j}}_{\mathrm{nm}} &= \sum_{\alpha=1}^{\infty}\sum_{\beta=-\alpha}^{\alpha} T_{21}^{\mathrm{j},\alpha\beta\mathrm{nm}}P^{\mathrm{j}}_{\alpha\beta} + T_{22}^{\mathrm{j},\alpha\beta\mathrm{nm}}Q^{\mathrm{j}}_{\alpha\beta}. \end{aligned} \tag{2.36}$$

By writing the above equations in matrix form:

$$\begin{pmatrix} |a_{\mathrm{all}}\rangle \\ |b_{\mathrm{all}}\rangle \end{pmatrix} = \begin{pmatrix} \overline{\tau}_{11} & \overline{\tau}_{12} \\ \overline{\tau}_{21} & \overline{\tau}_{22} \end{pmatrix} \left[\begin{pmatrix} |p_{\mathrm{all}}\rangle \\ |q_{\mathrm{all}}\rangle \end{pmatrix} - \begin{pmatrix} \overline{A} & \overline{B} \\ \overline{B} & \overline{A} \end{pmatrix} \begin{pmatrix} |a_{\mathrm{all}}\rangle \\ |b_{\mathrm{all}}\rangle \end{pmatrix} \right], \tag{2.37}$$

where

$$\begin{pmatrix} |a_{\mathrm{all}}\rangle \\ |b_{\mathrm{all}}\rangle \end{pmatrix} = \begin{pmatrix} |a\rangle^1 \\ \vdots \\ |a\rangle^n \\ |b\rangle^1 \\ \vdots \\ |b\rangle^n \end{pmatrix}, \quad \begin{pmatrix} |p_{\mathrm{all}}\rangle \\ |q_{\mathrm{all}}\rangle \end{pmatrix} = \begin{pmatrix} |p\rangle^1 \\ \vdots \\ |p\rangle^n \\ |q\rangle^1 \\ \vdots \\ |q\rangle^n \end{pmatrix}, \tag{2.38}$$

$$\overline{\tau}_{\mathrm{ij}} = \begin{pmatrix} \overline{T}^{1}_{\mathrm{ij}} & \overline{0} & \cdots & \cdots & \cdots & \overline{0} \\ \overline{0} & \overline{T}^{2}_{\mathrm{ij}} & & & & \vdots \\ \vdots & & \ddots & & & \vdots \\ \vdots & & & \ddots & & \vdots \\ \vdots & & & & \overline{T}^{\mathrm{N}-1}_{\mathrm{ij}} & \overline{0} \\ \overline{0} & \cdots & \cdots & \cdots & \overline{0} & \overline{T}^{\mathrm{N}}_{\mathrm{ij}} \end{pmatrix}, \tag{2.39}$$

$$\overline{X} = \begin{pmatrix} \overline{0} & \overline{X}_{1\to 2} & \overline{X}_{1\to 3} & \ddots & \ddots & \overline{X}_{1\to \mathrm{N}} \\ \overline{X}_{2\to 1} & \overline{0} & \overline{X}_{2\to 3} & \ddots & \ddots & \overline{X}_{2\to \mathrm{N}} \\ \ddots & \ddots & \ddots & \ddots & \ddots & \ddots \\ \ddots & \ddots & \ddots & \ddots & \ddots & \ddots \\ \ddots & \ddots & \ddots & \ddots & \overline{0} & \ddots \\ \overline{X}_{\mathrm{N}\to 1} & \overline{X}_{\mathrm{N}\to 2} & \cdots & \cdots & \cdots & \overline{0} \end{pmatrix}. \tag{2.40}$$

Here, $\overline{\tau}_{\mathrm{ij}}$ denotes the sub-supermatrix containing the sub-T-matrix of every scatterer in the ensemble and $\overline{X}$, where X can be either A or B. They describe the transformation of VSHs from the local coordinate system of one scatterer to the coordinate system of another scatterer. Equation 2.37 can be rewritten in the form of:

$$\begin{pmatrix} |a_{\mathrm{all}}\rangle \\ |b_{\mathrm{all}}\rangle \end{pmatrix} = \left[\begin{pmatrix} \overline{I} & \overline{0} \\ \overline{0} & \overline{I} \end{pmatrix} + \begin{pmatrix} \overline{\tau}_{11} & \overline{\tau}_{12} \\ \overline{\tau}_{21} & \overline{\tau}_{22} \end{pmatrix} \begin{pmatrix} \overline{A} & \overline{B} \\ \overline{B} & \overline{A} \end{pmatrix} \right]^{-1} \begin{pmatrix} \overline{\tau}_{11} & \overline{\tau}_{12} \\ \overline{\tau}_{21} & \overline{\tau}_{22} \end{pmatrix} \begin{pmatrix} |p_{\mathrm{all}}\rangle \\ |q_{\mathrm{all}}\rangle \end{pmatrix}, \tag{2.41}$$

$$\begin{pmatrix} |a_{\mathrm{all}}\rangle \\ |b_{\mathrm{all}}\rangle \end{pmatrix} = \overline{\tau} \begin{pmatrix} |p_{\mathrm{all}}\rangle \\ |q_{\mathrm{all}}\rangle \end{pmatrix}. \tag{2.42}$$

The above equation links the scattering coefficients of individual particles in the ensemble with the incident field coefficients at every individual particles. The matrix $\overline{\tau}$ can be called the T-matrix in local coordinates due to this fact.

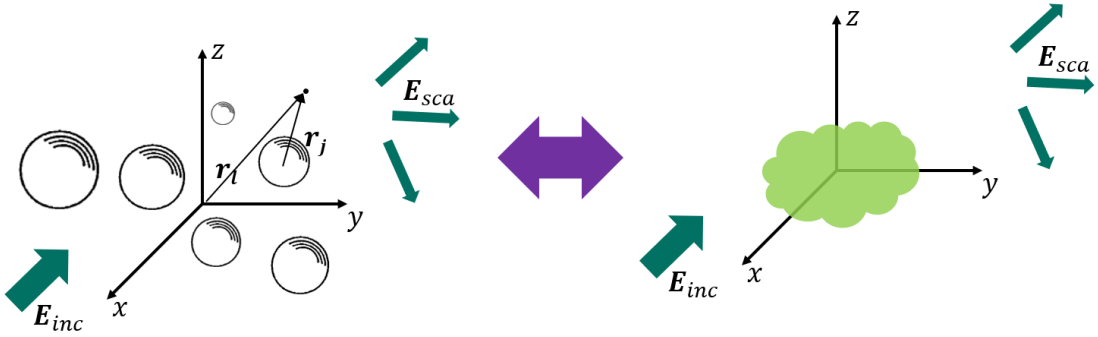

Figure 2.4 *The transformation from local coordinate T-matrix into global coordinate T-matrix. The transformation can be considered as considering all scatterer as an "effective scatterer" located at certain location* $\mathbf{r}_\mathrm{e}$*. Here, operator W described in Eq. 2.43 can be considered as an operator which translates the position of each particle* $\mathbf{r}_\mathrm{j}$ *to a single point in space* $\mathbf{r}_\mathrm{e}$*.* $\mathbf{E}_\mathrm{inc}$*, and* $\mathbf{E}_\mathrm{sca}$ *denote incident and scattered fields, respectively.*

2.3.2 Global coordinates formalism

To define several experimental parameters, such as cross-sections, it is important to describe the scattering coefficients in a single coordinate system. The T-matrix in local coordinates, while it is useful to describe the scattering of multiple objects, cannot provide the cross-sections of the whole structure directly. Moreover, often the effective response of the ensemble is much more sought compared to the individual scattering response of a constituent particle. Based on these requirements, it is important to be able to describe everything in terms "effective" T-matrix in a single coordinate system. We will call this the T-matrix in global coordinates based on the fact that everything is described in a single, i.e. a global, coordinate system.

To transform the coordinate system from different local position of each scatterer into one single coordinate system, the addition theorem of VSHs, as described in Eq. 2.34, needs to be applied. In this case, we need to transform VSHs from all local coordinate of each scatterer into a single referential coordinate in space, as can be seen in Fig. 2.4. This can be done by using matrix multiplication:

$$\overline{T} = \overline{W}\ \overline{\tau}\ \overline{W}^{L}, \tag{2.43}$$

where $\overline{W}$ denotes a matrix which contains translation operator from local coordinate of each scatterer to a single point in space. For this particular reason, this matrix therefore is:

$$\overline{W} = \begin{pmatrix} A_1^{1\to\mathrm{e}} & A_1^{2\to\mathrm{e}} & \cdots & A_1^{n\to\mathrm{e}} & B_1^{1\to\mathrm{e}} & B_1^{2\to\mathrm{e}} & \cdots & B_1^{n\to\mathrm{e}} \\ B_1^{1\to\mathrm{e}} & B_1^{2\to\mathrm{e}} & \cdots & B_1^{n\to\mathrm{e}} & A_1^{1\to\mathrm{e}} & A_1^{2\to\mathrm{e}} & \cdots & A_1^{n\to\mathrm{e}} \end{pmatrix}. \tag{2.44}$$

2.4 Clausius-Mossotti homogenization theory

In this section, a theoretical foundation of mixing rules will be introduced. Mixing rules play an important rule as they provide a simplified analysis when dealing with a large number of particles inside a certain volume. Here, we will focus our discussion on the Clausius-Mossotti homogenization theory. This homogenization theory will be used in the later chapters in this thesis to simplify the analysis of the response of the system. The main assumption of this theory is that the size of the inclusions is much smaller compared to the wavelength, such that the incident electromagnetic field cannot probe the details of the structure. This means that the incident electromagnetic field can only see the "effective" response of the whole ensemble. Note that, however, many other more advanced mixing rules exist, which will not be the scope of this section.

As previously described in section 2.1.1, the induced electric field inside the medium can be described as in Eq. 2.3. In homogenization theory, it is therefore desirable to obtain the polarization of the inclusions. For a linear material, the induced polarization due to the external electric field can be written as:

$$\mathbf{p}(\omega) = \alpha(\omega)\mathbf{E}_{\mathrm{e}}(\omega), \tag{2.45}$$

where $\alpha(\omega)$ is the polarizability and $\mathbf{E}_{\mathrm{e}}(\omega)$ is the external electric field. Using this fact, the average polarization inside the material, $\langle \mathbf{P}(\omega) \rangle$ can be written as:

$$\langle \mathbf{P}(\omega) \rangle = n\mathbf{p}(\omega), \tag{2.46}$$

where n is dipole density in the materials. Using dipole approximation, for a sphere with volume V, the polarizability (in dipole limit) can be obtained from Mie coefficients,

$$\alpha(\omega) = -\frac{\sqrt{12\pi}i}{cZ(\omega)k(\omega)} A_{11}(\omega), \tag{2.47}$$

where Z is the impedance of background medium, defined as $Z(\omega) = \frac{\varepsilon(\omega)}{\mu(\omega)}$, and A_{11} is the Mie coefficient described in Eq. 2.19.

Now, since the polarizability of a single sphere is obtained, the average electric flux density, $\langle \mathbf{D}(\omega) \rangle$, can be written as:

$$\langle \mathbf{D}(\omega) \rangle = \varepsilon_{\mathrm{eff}}(\omega)\mathbf{E}_{\mathrm{ext}}(\omega) = \varepsilon_{\mathrm{b}}(\omega)\mathbf{E}_{\mathrm{ext}}(\omega) + \langle \mathbf{P}(\omega) \rangle, \tag{2.48}$$

where $\langle \mathbf{P}(\omega) \rangle$ is the average polarization of the inclusions and $\varepsilon_{\mathrm{eff}}(\omega)$ is the effective permittivity of the ensemble, which is the main focus of this section.

To obtain the effective permittivity, we need to know the exact expression of $\langle \mathbf{P}(\omega) \rangle$. This parameter is connected to dipole moment density in the mixture, $\langle \mathbf{P}(\omega) \rangle = n\mathbf{p}(\omega)$, where n

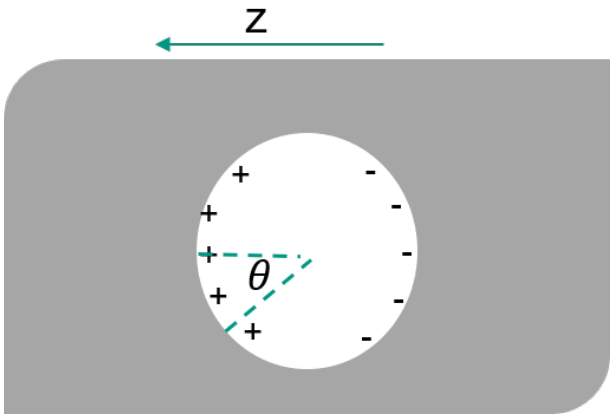

Figure 2.5 *A schematic representation of calculation of the field in an imaginary spherical cavity in a uniformly polarized medium. The medium is assumed to be a homogenous medium.*

is the dipole moment density. For a very diluted scenario, we can imagine the incident field as the original incident field. However, by taking a step further, i.e. higher density, the main challenge now lies on the fact that one cannot assume the inclusion incident field is the same as the external field. For this, ones need to take the Born approximation up to the first order, that is:

$$\mathbf{E}_{\mathrm{e}}(\mathbf{r},\omega) = \mathbf{E}^{\mathrm{inc}}_{\mathrm{ori}}(\mathbf{r},\omega) + \mathbf{E}^{\mathrm{inc}}_{1}(\mathbf{r},\omega), \tag{2.49}$$

where $\mathbf{E}_{\mathrm{e}}(\mathbf{r},\omega)$ denotes the total incident field at one particle, and the subscripts on the right side denote the original incident field (ori), incident field from other particle after one scattering event (1). For the correction term, one can imagine a field due to polarization charges on the surface of an imaginary cavity, as seen in Fig. 2.5.[78] The surface charge density on the surface of the cavity is $\langle \mathbf{P}(\omega) \rangle \cos\theta$, where P is the polarization. the electric field at the center of the spherical cavity of radius f, $\mathbf{E}_{\mathrm{cent}}(\omega)$, is therefore

$$\mathbf{E}_{\mathrm{cent}}(\omega) = \frac{1}{4\pi\varepsilon_{\mathrm{b}} f^2} \int_0^{\pi} (2\pi f \sin\theta)(a d\theta)(\langle \mathbf{P}(\omega) \rangle \cos\theta)(\cos\theta) = \frac{1}{3\varepsilon_{\mathrm{b}}} \langle \mathbf{P}(\omega) \rangle . \tag{2.50}$$

Using this correction term, the Born approximation in Eq. 2.49 can be written as:

$$\mathbf{E}_{\mathrm{e}}(\mathbf{r},\omega) = \mathbf{E}^{\mathrm{inc}}_{\mathrm{ori}}(\mathbf{r},\omega) + \frac{1}{3\varepsilon_{\mathrm{b}}} \langle \mathbf{P}(\omega) \rangle . \tag{2.51}$$

By combining Eqs. 2.48 and 2.51, the average permittivity can be written as:

$$\varepsilon_{\mathrm{eff}}(\omega) = \varepsilon_{\mathrm{b}}(\omega) + \frac{n\alpha(\omega)}{1 - n\alpha(\omega)/3\varepsilon_{\mathrm{b}}(\omega)}, \tag{2.52}$$

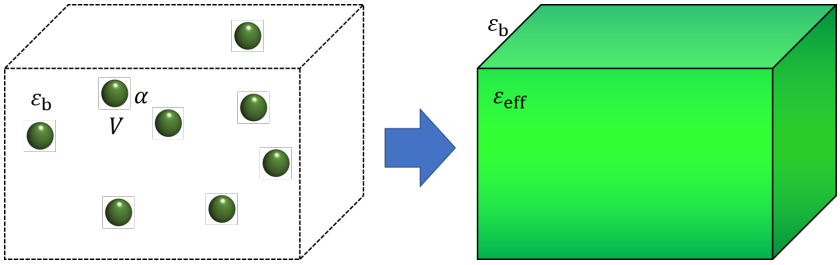

Figure 2.6 *An imaginary box which contains several identical subwavelength spheres with volume V. Here, the total response of the particles in the box can be imagined as response from a homogenous box with effective permittivity* ε_{eff}.

which is the Clausius-Mossotti formula. The same procedure can also be repeated to calculate the effective permeability of the medium, yielding:

$$\mu_{\text{eff}}(\omega) = \mu_b(\omega) + \frac{n\alpha_m(\omega)}{1 - n\alpha_m(\omega)/3\mu_{\text{b}}(\omega)}, \tag{2.53}$$

where

$$\alpha_m(\omega) = -\frac{\sqrt{12\pi}i}{Z(\omega)k(\omega)} A_{12}(\omega). \tag{2.54}$$

2.5 Summary

Finally, we arrived at the end of the second chapter of this thesis. In this chapter, the basics of the electromagnetic wave theory in form of Maxwel's equations was briefly discussed. This was followed by the description of the scattering of light at a spherical object, something that has been described in the Mie theory. The T-matrix was also introduced, followed by its representation in local and global coordinate system. At the end of the chapter, effective medium theory using Clausius-Mosoti approach was discussed.

Using all of these contents, the basic theoretical foundations for the next chapters had been discussed. We will emphasize the important theoretical frameworks described in this chapter here and list their applications in the subsequent chapters.

The T-matrix description in local coordinates, as described in section 2.3.1, will be used to extract individual modes of an electromagnetic scatterer in section 3.1.2. On the other hand, the T-matrix in global coordinates, described in section 2.3.2, will be the main tool of most of the content of this thesis. The spectral decompositions of this matrix will be used to describe the collective modes of meta-atoms (3.1.1, 3.2), extracting the observable quantities of bulk self-assembled metamaterials made of identical meta-atoms(4.1), and discussing the Fano properties of metamaterials made from self-assembled technique (4.2). Finally, Clausius-Mossotti homogenization theory (section 2.4) will be used to analyze the origin of the modes in

section 3.1.2 and hybridizing plasmonic nanoparticles with whispering gallery mode resonator for sensing application in section 5.2.

Chapter 3

3 Modal Analysis of an Electromagnetic Scatterer

After having discussed the theoretical background in the previous chapter, we are ready for some more practical applications. In this chapter, we will discuss the properties of an electromagnetic scatterer in terms of modes. In the first section, the description of modes obtained from an eigenvalue decomposition of the T-matrix will be discussed. This is followed by the decomposition of the scattering cross-section into eigenmodes of scatterer. The same procedure will be applied to both global and local coordinate T-matrices, as described in the previous chapter. These procedures offer complementary information about the modes, namely the individual modes sustained by each subsystem of the scatterer and the collective modes of the entire system itself. In the end of this section, a link between eigenmodes in global and local coordinates will be presented, showing that one description can be transformed to the other description quite conveniently.

The second section of this chapter will be dedicated to modes obtained from the singularvalue decomposition of the T-matrix. In contrast to the modes obtained from the eigenvalue decomposition, modes from singularvalue decomposition are always orthogonal to each other. This fact results in the dissapearance of cross-coupling terms when discussing scattering cross-section of scatterer. Finally, a comparison between the decomposition of scattering cross-section into singularmodes and eigenmodes will be provided, shedding light from different perspective when discussing Fano resonances of a scatterer.

The content of this chapter is mostly based on P.1 (section 3.2) and P.2 (section 3.1).

3.1 Eigenvalue decomposition

Generally, understanding the optical response of a scatterer is a tedious task, as infinitely many different responses can appear. This corresponds to the infinite number of possibilities to choose an incident field. Due to this reason, it is important to develop a framework where the analysis of the optical properties of scatterers can be made in a simple way and particularly independent of the chosen illumination. Here, the concept of modes plays an important role to understand the response of the structure.

As in other branches of physics, analytical solutions of modes only exist for very basic objects, such as a sphere. In the field of scattering, since the problem happens in an unbounded domain,

the identification of the modes is challenging since the corresponding operator associated with the problem is non-Hermitian.[79] In this sense, several approaches have been developed to obtain the modes of electromagnetic scattering to describe the optical properties of the structure. Singular expansion methods using integral operators allow to compute modes from a perfectly conducting scatterer.[80] Another approach is called characteristics mode approach, which is developed by solving a weighted eigenvalue problem based on the impedance matrix obtained from the method of moments.[81,82] Eigenmode analysis using an integral approach based on volumetric method of moments was also proposed to address scattering problem of dielectric and plasmonic system.[83,84] This was followed by the spectral decomposition using an eigenvalue method of the interaction matrix obtained within coupled dipole approximation[85,86] as well as an inverse scattering matrix analysis in the Fourier modal method.[87] Poles in the complex frequency plane of the scattering matrix[88] and from integral operator[89] were also proposed. Another spectral decomposition, that is, eigenvalues[90P.2] and singularvalues [P.1] of the T-matrix, were also introduced. Finally, quasi-normal modes[91–93] were proposed to deduce the modes of the scattering structure of interest.

Based on the development discussed in the previous paragraph, we can conclude that there are many methods to extract the modes of the system. In this thesis, we will discuss the modes obtained from the T-matrix. As the T-matrix contains the complete information of the scatterer, this implies that all information of the modes should be contained in the T-matrix of the corresponding scatterer. For this reason, an eigenvalue decomposition (EVD) of the T-matrix can be used to extract the modes of the scatterer. It reads as:

$$\overline{T} = \overline{X}\,\overline{E}\,\overline{X}^{-1}, \tag{3.1}$$

where

$$\overline{X} = \begin{pmatrix} |\mathbf{x}_1\rangle & |x_2\rangle & \cdots & \left|x_{\mathrm{j}-1}\right\rangle & \left|x_{\mathrm{j}}\right\rangle \end{pmatrix}, \tag{3.2}$$

$$\overline{E} = \begin{pmatrix} \eta_1 & 0 & \cdots & 0 & 0 \\ 0 & \eta_2 & \cdots & 0 & 0 \\ 0 & \vdots & \ddots & \vdots & 0 \\ 0 & 0 & \cdots & \eta_{\mathrm{j}-1} & 0 \\ 0 & 0 & \cdots & 0 & \eta_{\mathrm{j}} \end{pmatrix}. \tag{3.3}$$

Here, $\overline{X}$ is a matrix which contains eigenvectors ($|x\rangle$) and $\overline{E}$ is a diagonal matrix where each entry denotes an eigenvalue (η) of $\overline{T}$. The EVD of the T-matrix can also be written as:

$$\overline{T}\,|x_{\mathrm{i}}\rangle = \eta_{\mathrm{i}}\,|x_{\mathrm{i}}\rangle\,. \tag{3.4}$$

By comparing the above equation with the T-matrix definition, $\overline{T}\left|p\right\rangle = \left|a\right\rangle$, we can see that eigenvector, which contains the multipolar components of the eigenmode, appear on both sides.

3.1.1 Eigenvalue decomposition in global coordinates

The T-matrix in global coordinates offers the information on how "effective" an ensemble of objects scatters a particular incident field. In this sense, it describes the collective/effective response of the scatterers, which made the whole ensemble interact with the incident field. Thus, it can be said that the eigenmodes obtained from T-matrix in global coordinates are "collective eigenmodes" of the ensemble of the scatterers.

After clarifying the terminology, it is time to analyze the scattering response of an ensemble of scatterers in terms of collective eigenmodes. Here, emphasis will be put on the scattering cross-section of the system. The scattering cross-section (σ_{sca}) can be obtained from the scattering coefficients. In matrix form, this relation read as:

$$\sigma_{\mathrm{sca}} = \frac{4\pi}{k_{\mathrm{b}}^2}\left\langle a|a\right\rangle = \frac{4\pi}{k_{\mathrm{b}}^2}\left\langle p\right|\overline{T}^{\dagger}\,\overline{T}\left|p\right\rangle, \tag{3.5}$$

where k_{b} is the wavevector of the background medium, superscript † denotes the transpose conjugate of the matrix while $\left|a\right\rangle$ and $\left|p\right\rangle$ are the vectors that contain the scattering and incident field coefficients, respectively. The notation $\left\langle a\right|$ denotes the transpose conjugate of the vector. In the following we use the identity:

$$\overline{T}^{\dagger} = \left(\overline{X}\,\overline{E}\,\overline{X}^{-1}\right)^{\dagger} = \overline{X}^{-1\dagger}\,\overline{E}^{\dagger}\,\overline{X}^{\dagger} = \overline{Y}\,\overline{E}^{\dagger}\,\overline{Y}^{-1} \tag{3.6}$$

where $\overline{Y} = \overline{X}^{-1\dagger}$ is the matrix which contains the eigenvectors of $\overline{T}^{\dagger}$. That is true since the following identity exists:

$$\overline{Y}^{\dagger}\,\overline{X} = \overline{X}^{\dagger}\,\overline{Y} = \overline{I}. \tag{3.7}$$

Here, $\overline{I}$ is an identity matrix. By employing this fact, the following biorthogonality relations can be derived:

$$\sum_{\mathrm{j}}\left|y_{\mathrm{j}}\right\rangle\left\langle x_{\mathrm{j}}\right| = \sum_{\mathrm{j}}\left|x_{\mathrm{j}}\right\rangle\left\langle y_{\mathrm{j}}\right| = \overline{I}. \tag{3.8}$$

Now the scattering cross-section can be written as:

$$\sigma_{\mathrm{sca}} = \frac{4\pi}{k_{\mathrm{b}}^2}\left\langle p\right|\overline{T}^{\dagger}\,\overline{I}\,\overline{T}\,\overline{I}\left|p\right\rangle. \tag{3.9}$$

$$\sigma_{\mathrm{sca}} = \frac{4\pi}{k_{\mathrm{b}}^2}\left\langle p\right|\overline{T}^{\dagger}\sum_{\mathrm{j}}\left|y_{\mathrm{j}}\right\rangle\left\langle x_{\mathrm{j}}\right|\overline{T}\sum_{\mathrm{i}}\left|x_{\mathrm{i}}\right\rangle\left\langle y_{\mathrm{i}}|p\right\rangle. \tag{3.10}$$

By using the definition in Eq. 3.4, the following equation can be obtained:

$$\sigma_{\mathrm{sca}} = \frac{4\pi}{k_{\mathrm{b}}^2} \sum_{\mathrm{j}} \sum_{\mathrm{i}} \eta_{\mathrm{i}} \eta_{\mathrm{j}}^{*} \left\langle p \middle| y_{\mathrm{j}} \right\rangle \left\langle y_{\mathrm{i}} \middle| p \right\rangle \left\langle x_{\mathrm{j}} \middle| x_{\mathrm{i}} \right\rangle . \tag{3.11}$$

The above equation tells us that the scattering cross-section can be decomposed in terms of eigenmodes of the T-matrix. η_{i}, which denotes the eigenvalue of eigenvector i, denotes the strength of the mode. Due to this fact, we will call this term the modal strength of the respective eigenmode. The second and third terms, $\langle p|y_{\mathrm{i}}\rangle$ and $\langle y_{\mathrm{i}}|p\rangle$, denote the projection of the incident field onto the eigenmode i sustained by the structure. The multiplication of these terms, $\langle p|y_{\mathrm{i}}\rangle \langle y_{\mathrm{i}}|p\rangle$, will be called projection parameter c_{i}^2. Finally the fourth term $\left\langle x_{\mathrm{i}} \middle| x_{\mathrm{j}} \right\rangle$ denotes the cross coupling term between mode i and mode j. The extinction cross-section can be derived in the same way, yielding:

$$\sigma_{\mathrm{ext}} = \mathrm{Re} \left(\sum_{\mathrm{i}} \sum_{\mathrm{j}} \eta_{\mathrm{j}} \left\langle y_{\mathrm{j}} \middle| p \right\rangle \langle p|y_{\mathrm{i}}\rangle \left\langle x_{\mathrm{i}} \middle| x_{\mathrm{j}} \right\rangle \right) . \tag{3.12}$$

Here, we see that, the extinction cross-section can also be expressed using the terms discussed previously. In this case, however, the modal strength only appears once, and the value inside the summation, in general is a complex function. However, the only important information from this complex function is it's real part, which is the extinction cross-section.

Due to the fact that eigenvalues are calculated independently at each frequency, a mode tracking algorithm is needed to deduce the same mode at different frequencies. We track the modes by calculating all eigenvalues for a small number of frequencies, α, frequencies that are spectrally very close to each other. Typically, $\alpha = 5$ is used for our purpose. The eigenvalues are then assigned to a specific mode upon visual inspection. Following this, an automatic procedure is applied to track the modes at the next frequency. The previously known modes at several lower frequencies are fitted with polynomial order of $\alpha - 2$. The corresponding mode for the next frequency is the mode with an eigenvalue that is closest to the extrapolated eigenvalue obtained from such fitting. In the case of degenerate mode, further efforts need to be put in place to track the modes. Here, we apply the inner product between the degenerate modes at the next frequency and the frequency before it. The maximum value of the inner product between these eigenvectors denotes then which pair belong to the same mode. These procedures allow us to link the newly calculated eigenvalues of the same mode for different frequencies.

After we are done with the theoretical framework of the decomposition of cross-sections in term of eigenmodes of the structure, we will show several examples to better understand the concept of the eigenmodes obtained from the T-matrix of an ensemble of the scatterers. The simplest structure one can imagine is a sphere. Here, we consider a gold nanosphere with radius of 90 nm. The background is vacuum with $\varepsilon_{\mathrm{b}} = 1$. Throughout this thesis, unless otherwise

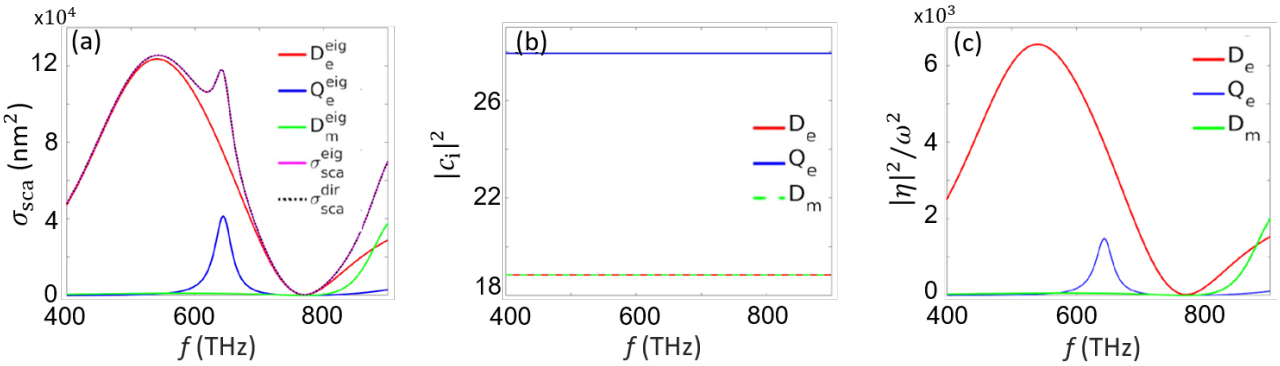

Figure 3.1 *(a) Decomposition of the scattering cross-section of a gold sphere with a radius of 90 nm into the eigenmodes obtained from T-matrix of the scatterer. (b) Projection parameter of the incident plane wave onto eigenvector of each mode, and (c) modal strength of each eigenmodes.* $D_{\mathrm{e}}^{\mathrm{eig}}$, $Q_{\mathrm{e}}^{\mathrm{eig}}$ $D_{\mathrm{m}}^{\mathrm{eig}}$ *denote the values associated with electric dipole, electric quadrupole and magnetic dipole modes, while* $\sigma_{\mathrm{sca}}^{\mathrm{eig}}$ *and* $\sigma_{\mathrm{sca}}^{\mathrm{dir}}$ *denote the values of the scattering cross-section obtained from summation of the contributions of all modes and direct calculation, respectively. Adapted from P.2*

stated, the permittivity of gold is described by a Drude model:

$$\varepsilon_{\mathrm{Au}} = \varepsilon_{\infty} - \frac{\omega_p^2}{\omega(\omega + i\gamma)}. \tag{3.13}$$

where $\varepsilon_{\infty} = 9$, $\hbar\omega_p = 9$ eV, and $\hbar\gamma = 0.05$ eV.[94] The main reason we consider a Drude model is due to the fact that it provide smooth dependency over all frequency range of interest.

The T-matrix of a spherical object is a diagonal matrix, where the diagonal components are the Mie coefficients of the sphere, as can be seen in Eq. 2.23. As the matrix is already diagonalized, the modal strength of each mode corresponds to the Mie coefficient and the associated eigenvectors correspond to the different VSHs. This considered sphere supports 3 notable modes in the frequency range of interest (400-900 THz), as shown in Fig. 3.1 (a). From the constribution of each eigenmode to the scattering cross-section, it can be deduced that the electric dipole mode is the one that contributes most to the scattering cross-section. The resonance frequency of the electric dipole is at 520 THz, while for the electric quadrupole mode it is at 650 THz. The magnetic dipole mode has its resonance frequency at even higher frequencies, outside our frequency range of interest. Here, we also compare the values obtained from Eq. 3.11, and they match perfectly. The effect of the excitation field can be seen from the projection parameter c_{i}^2, as shown in Fig. 3.1 (b). Here, we plot the projection parameter of each mode. It can be deduced that the incident field can excite the electric quadrupole more easily than other modes. Finally, the multiplication of modal strength and projection parameter results in the contribution of each mode to the scattering cross-section, as can be seen in Fig. 3.1 (a).

The next structure that is slightly more complicated is a dimer made by two identical spheres.

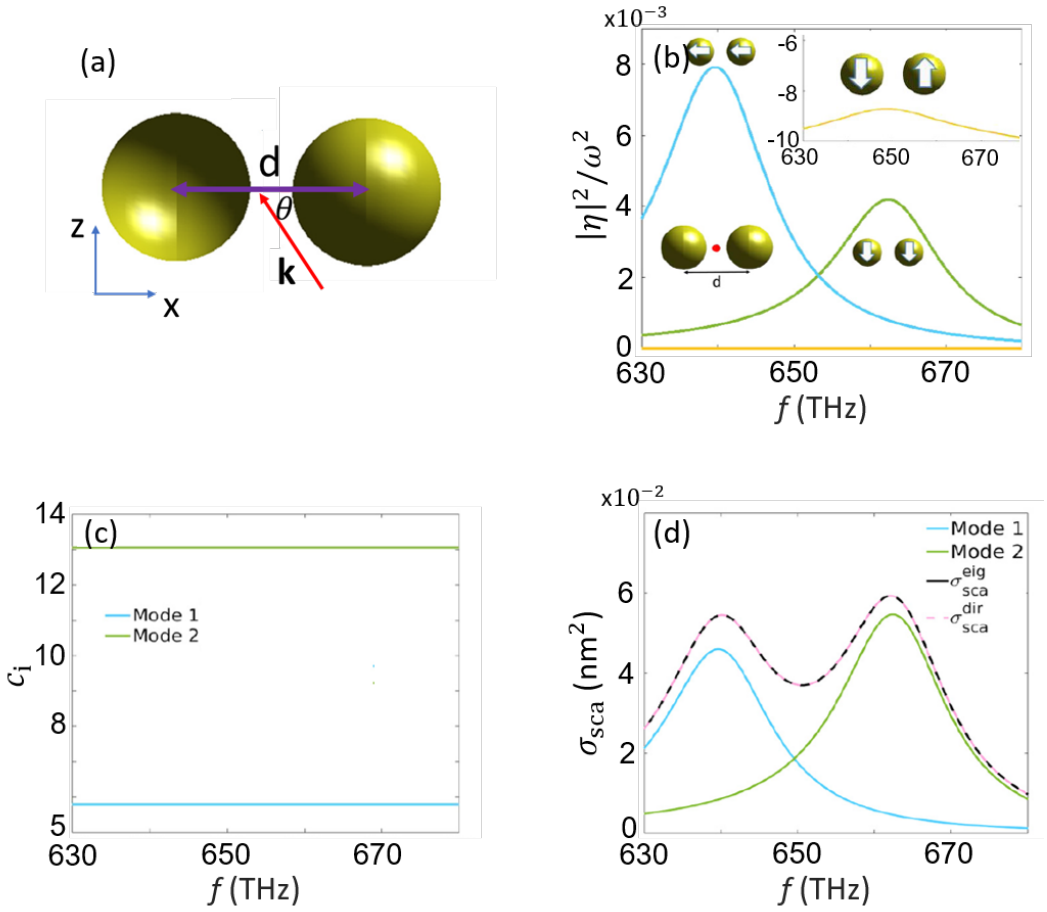

Figure 3.2 *(a) The scattering scenario of the dimer structure. Here, The incident wavevector lies in x-z plane and it makes an angle θ with respect to the x axis, such that $\tan\theta = \frac{2}{3}$. (b) Modal strength obtained using the T-matrix in global coordinate system. The inset shows the magnetic dipole mode in logarithmic scale that is much smaller in magnitude when compared to the collective modes that give rise to an electric dipole moment in either x- or z- direction. (c) Projection parameter of the incident plane wave onto the eigenvector of each mode and (d) decomposition of the scattering cross-section into the modes obtained from the T-matrix in global coordinate system. Comparison to direct solution is also shown here and a perfect agreement is found. Adapted from P.2*

Here, we consider gold nanospheres with a radius of 3 nm placed in vacuum. In contrast to the previous discussion, we choose a small sphere in our consideration due to the reason that it's response can be described by quasi-static approximation. This approximation will be used later on to compare the modes obtained from the T-matrix with the modes obtained from hybridization theory.[94] As the size of the spheres is so small,we can also restrict our attention to a T-matrix in dipole approximation, i.e. the T-matrix is expanded up to both electric and magnetic dipolar order. To study the contribution of different modes to the scattering response from such a dimer structure, we choose the magnetic field of the incident field to be oriented in y direction, while it's wavevector lies in x-z plane and making an angle θ. In particular, we

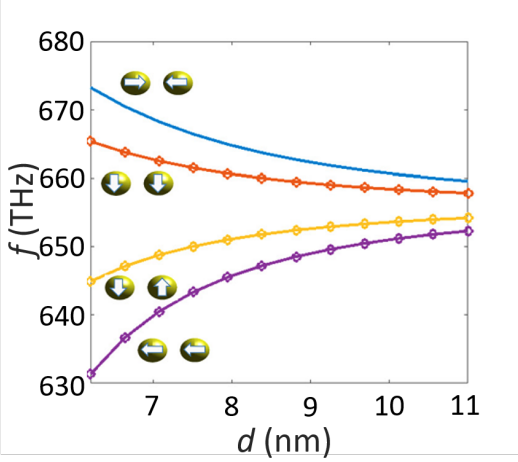

Figure 3.3 *Comparison of the resonance frequency of each mode obtained by using the T-matrix in global coordinates (dot) and hybridization theory(straight lines). Adapted from P.2.*

choose θ such that $\tan\theta = \frac{2}{3}$. The sketch of this problem can be seen in Fig. 3.2 (a).

Figure 3.2 (b) shows the modal strength of each mode of the dimer considered here. Here, we choose the origin of our coordinate system to be the point of highest symmetry, as denoted by the red dot in Fig. 3.2 (b). Three distinct modes can be observed. Two dominant modes correspond to the modes where the electric dipoles in the individual spheres point in the same direction. They have relatively strong modal strength compared to the third mode. These modes correspond to bright modes, which can be excited easily with an external incident field. On the other hand, the third mode, where the electric dipoles in each individual sphere point in opposite directions corresponds to a magnetic dipole mode in the global coordinate system. This mode is shown in the inset of Fig. 3.2 (b), where the amplitude is plotted in a logarithmic scale. It can be seen that this mode has a very small modal strength (approximately 10^{-6} smaller compared to the other two modes), which means that this mode is very weak compared to the other modes. Due to this fact, this mode is also sometimes called dark mode.

The projection parameter from the incident plane wave onto each mode is shown in Fig. 3.2 (c). Because the incident electric field has a component in both x and the z direction, both of the corresponding dominant modes shown in Fig. 3.2 (b) can be excited. Finally, by multiplying the results obtained in Fig. 3.2 (b) and (c), the modal decomposition of σ_{sca} is shown in Fig. 3.2 (d). Here, by decomposing the response, the origin of each peaks can be attributed to the corresponding modes. We also show here a perfect agreement of the scattering cross-section obtained from full wave simulations and the modal decomposition. This emphasis particularly the point that it is fully sufficient to consider these two dipolar modes to express the properties of the entire system.

A further validation of the modes obtained from the T-matrix in global coordinates can be made by comparing the resonance frequency of each modes with the resonance frequency obtained from a hybridization theory. In quasi-static approximation, the resonance frequency

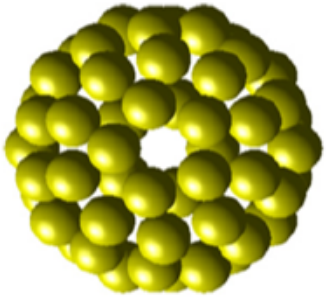

Figure 3.4 *Geometry of the considered cluster of spheres made from 60 spheres with radius of 20 nm. Here, the spheres are placed on top of a spherical surface with a radius of 76 nm. Adapted from P.2.*

of each mode can be written as:[94]

$$\omega_{\mathrm{res}} = \frac{\omega_{\mathrm{p}}}{\sqrt{2+\varepsilon_{\mathrm{b}}}}\sqrt{\frac{1+g}{1+\eta g}}, \tag{3.14}$$

where ω_p is gold plasma frequency. η is a permittivity dependent variable, defined as:

$$\eta = \frac{\varepsilon_b - 1}{\varepsilon_b + 2}, \tag{3.15}$$

while g describes the geometry, and it is defined as

$$g = \frac{vR^3}{d^3}. \tag{3.16}$$

Here, v can be -2, -1, 1, or 2, depending on each sphere dipole configuration of the dimer structure.[94] Figure 3.3 shows this comparison. As previously discussed, the T-matrix in global coordinates supports three distinct eigenmodes in dipole approximation (N=1). These three modes, which appear in global coordinates as effective electric dipole modes (purple and red dots) and one magnetic dipole mode (orange dots), appear naturally here. Their resonance frequencies match exactly with the resonance frequency obtained from hybridization theory when we vary the separation between the two spheres. The fourth mode obtained from hybridization theory (blue line), however, is missing. This is due to the fact that this particular dipole configuration, translates to a mode that is characterized by a strong electric quadrupolar mode with respect to the point of highest symmetry. Since we have been limiting ourselves to a dipole approximation in expressing the T-matrix, this electric quadrupolar mode, naturally, will not appear.

Having done the analysis for the more simpler structures and having demonstrated the kind of insights we can obtain from such analysis, we consider another structure more relevant to the

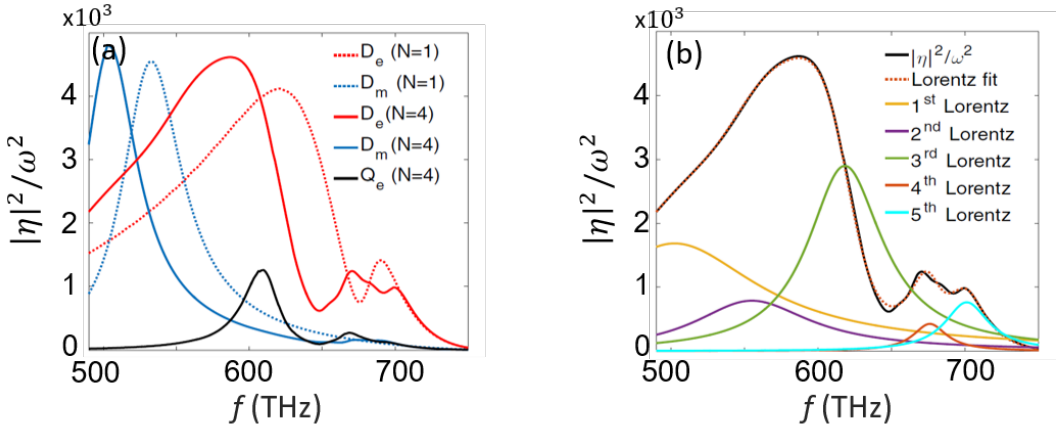

Figure 3.5 *(a) Frequency dependent modal strength of the three dominant modes obtained from the EVD of the T-matrix of meta-atom. We distinguish a mode which has dominant electric dipole (red), dominant magnetic dipole (blue) and electric quadrupole (black) moments. The dashed lines correspond to the results obtained by using dipole approximation, while solid lines are the results obtained using N=4. (b) Lorentzian decomposition of electric dipole mode with N=4. The decomposition into Lorentzians is done by employing Eq. 3.17. Adapted from P.2.*

scope of this thesis: a cluster made from 60 identical gold nanospheres, as shown in Fig. 3.4. Here, the radius of each gold nanosphere is 20 nm. They are arranged on top of a virtual sphere with a radius of 76 nm and the background refractive index is chosen to be vacuum ($\varepsilon_\mathrm{b} = 1$). These nanoparticles are ordered according to Ref,[95] such that the arrangement is highly symmetric. This symmetry is done to preserve the degeneracy of eigenmodes, which will ease the theoretical analysis. The point in space considered as central and to which the T-matrix in global coordinates refers to corresponds to the the center of mass of all spheres. The T-matrix in global coordinates is calculated by first applying Eq. 2.41 for each sphere, and then transforming such T-matrix in local coordinates to a new center coordinate by using Eq. 2.43.

Due to the fact that the structure cannot be considered in quasi-static regime anymore, higher order expansion terms need to be considered in expressing the T-matrix. By using the EVD of the T-matrix in global coordinates, the versatility of this approach will be highlighted. Figure 3.5 (a) shows the modal strength of the structure considered by taking into account higher order modes (N=4) and compares it with the modal strength obtained using dipole approximation (N=1). Here, D_e and D_m are modes with dominant electric and magnetic dipoles contribution, respectively. When considering N=1, the modes only have dipole (electric and magnetic) contribution. For magnetic dipole, the resonance frequency is found to be around 550 THz. For the electric dipole mode, in contrast to the magnetic dipole mode, the frequency dependent modal strength is composed of a profile of several resonances and the functional dependency is more complex. Next, by using higher order correction (N=4), the resonance positions of both electric and magnetic dipole modes are shifted to lower frequencies. In the case of the magnetic dipole mode, it is shifted to 520 THz. The same behavior can also be observed for electric dipole dominant mode. A higher order mode, a quadrupole mode, also

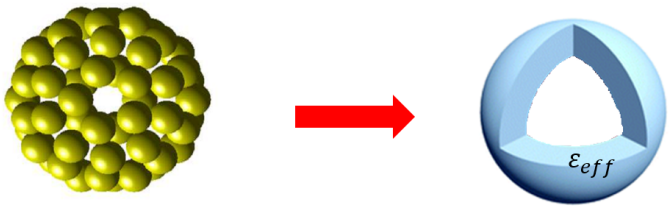

Figure 3.6 *Effective medium description of the cluster of spheres described in this section. Here, the ensemble of spheres can be replaced by a homogenous medium with an effective permittivity* ε_{eff}*. The inner and outer radius of the effective core-shell structure are 76 and 116 nm, which correspond to the minimum and maximum distance between the surface of each sphere with the center of the cluster.*

appears (black line) with its dominant resonance frequency around 620 THz. This fact suggests that dipole approximation is not valid anymore when we consider larger structures which support higher order modes.

To explore the origin of the different resonances in the electric dipole mode in more details, we fit it's corresponding modal strength with a coherent sum of several Lorentzian oscillators, as can be seen in Fig. 3.5 (b). Each of these oscillators corresponds to a specific resonance sustained by the meta-atom in the specific dipolar scattering channel. This decomposition can be written in mathematical form as:

$$f(\omega) = \omega^2 \left| \sum_{\mathrm{n}=1}^{\mathrm{L}} \frac{f_n}{\omega_{\mathrm{n}} - \omega^2 - i\gamma_{\mathrm{n}}\omega} \right|^2 . \tag{3.17}$$

Each oscillator is characterized by its amplitude f_{n}, its resonance frequency ω_{n} and linewidth γ_{n}. The multiplication factor ω^2 appears from the scaling of the modal strength as introduced previously.

It can be deduced that the electric mode can actually be decomposed into 5 different resonances. By doing the same fitting to the magnetic dipole mode, the profile can be reproduced by a single Lorentazian oscillator with resonance frequency of 500.9 THz. This suggests that the magnetic mode only consists of a single resonance.

The underlying physics of these Lorentzians can be explained in a quite simple way. Instead of tracking the contribution of each sphere one by one, we can consider the ensemble of gold nanoparticles as an effective medium with a permittivity expressed by the Clausius-Mosotti effective medium theory as presented in section 2.4. This homogenization procedure is described in Fig. 3.6. Instead of considering each nanoparticle, we consider our structure as a core-shell structure, where its core (with permittivity of 1) is surrounded by a homogenous medium with effective permittivity ε_{eff}. The effective permittivity of this shell is plotted in Fig. 3.7. In the same figure, we also plot the necessary permittivity of the shell material at which the layered sphere supports a plasmonic resonance in dipole approximation. This can be derived from

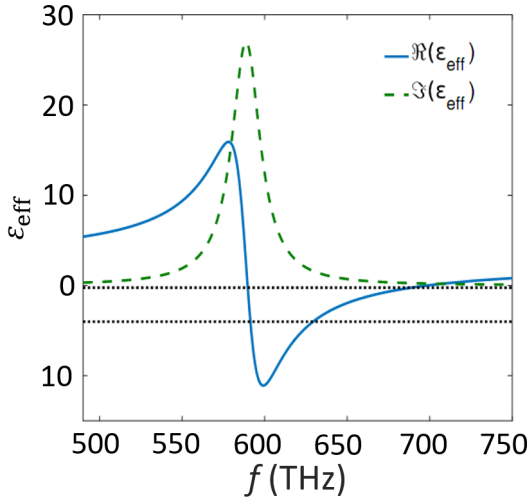

Figure 3.7 *Effective permittivity of a medium made of gold nanospheres embedded in vacuum. The filling fraction is 42.78%, which corresponds to the filling fraction of gold nanospheres described in Fig. 3.6. The black dotted lines represent the necessary permittivity required for the resonance condition of plasmonic mode in the layered sphere in dipole approximation, as described in Eq. 3.18. Adapted from P.2.*

Fröhlich condition for layered sphere,[96] and it is expressed as:

$$\varepsilon_s = -\frac{\varepsilon_c + 4 + 2\beta(\varepsilon_c + 1) \pm \sqrt{[\varepsilon_c + 4 + 2\beta(\varepsilon_c + 1)]^2 - 16\varepsilon_c(1-\beta)^2}}{4(1-\beta)^2}, \tag{3.18}$$

where

$$\beta = \frac{R_c^3}{R_s^3}. \tag{3.19}$$

Here, ε_s and ε_c denote the permittivity of the shell and core, while R_s and R_c denote the inner and outer radius of the core-shell structure. In our cluster, the inner radius corresponds to the shortest distance from the surface of each sphere to the center of mass, while the outer radius corresponds to the longest distance from the surface of each sphere to the center of mass.

It can be deduced from the data presented in Fig. 3.7, that the third (618 THz) and fifth (701 THz) Lorentzian resonances match closely to the two possible plasmonic resonance frequencies supported by the shell described in Eq. 3.18. Due to the fact that the absorption is quite weak around these frequencies, these resonances are well resolved. In contrast, the resonances around 600 THz happen in a spectral region where the absorption of the effective shell material is quite high. This fact prevents these resonances to have notable modal strength in the total response.

Besides these two plasmonic resonances, we also observe two further resonances that are supported at frequencies where the value of the shell effective permittivity is positive. This fact

suggests that the first Lorentzian (502.6 THz) and the second Lorentzian (555.3 THz) correspond to the dipolar Mie type resonance in the core-shell structure, which require a positive permittivity for their excitation. The last Lorentzian (676.6 THz) is dominantly electric quadrupole in origin, as its resonance is quite close to one of the peaks of electric quadrupole mode. This is because our cluster is not spherically symmetric, as it is composed of several nanoparticles. This means that, the corresponding T-matrix is not a diagonal matrix, and mixing between different VSHs in one mode is to be expected. Overall, this Lorentzian mode is weakly excited.

The same effective medium analysis can be made for the magnetic dipole mode. In this case, the positive effective permittivity of the shell material is the one who is responsible for this resonance. Overall, by using the effective medium approach, we can track the origin of the mode resonance positions of the cluster of spheres, which act as our meta-atom example, as described here.

In this section, we have shown that the modal description based on the eigenvalue decomposition of the T-matrix in global coordinates provides a convenient way to understand the response of the meta-atom. It was particularly the decomposition of the scattering cross-section into the contribution of each mode that enabled us to understand the response based on the modes of the corresponding meta-atom. However, using the T-matrix in global coordinates means we lost detailed information about the behavior of individual subsystem, as at the end, using the T-matrix in global coordinates, we can only probe the effective response of an ensemble of the scatterer. On the other hand, the information of the subsystem is contained in the T-matrix in local coordinates, which will be the main focus of the next section.

3.1.2 Eigenvalue decomposition in the local coordinates

In the previous section, we discussed how to obtain collective eigenmodes of the ensemble of the scatterers. This approach, however, cannot shed light on the response of the individual building blocks of the scatterer, as we only study the entire response of the whole structure. Often, it is also quite useful to understand the behavior of each individual constituent in the ensemble. This makes it desirable to obtain the eigenmodes of the individual constituent while it is interacting with other scatterers in the system. In this sense, the consideration of the T-matrix in local coordinates, which describes the response of individual scatterer in an ensemble, would be a more suitable element for the modes extraction. We will refer to the eigenmodes extracted from the T-matrix in local coordinates as individual modes due to the fact that it describes the eigenmodes of individual scatterer in the ensemble.

Before we proceed further, it is important to be able to decompose the optical response of the structure in terms of these individual eigenmodes. Comparable to the previous section, we will also only focus on the scattering cross-section in this section. Using operator $\overline{W}$, which contains the information of the coordinate system of each subsystem (as described in Eq. 2.43),

and combining it with Eq. 3.5, the following equation can be derived:

$$\sigma_{\mathrm{sca}} = \frac{4\pi}{k_{\mathrm{b}}^2} \left\langle p \right| \overline{W}^{L\dagger}\, \overline{\tau}^{\dagger}\, \overline{W}^{\dagger}\, \overline{W}\, \overline{\tau}\, \overline{W}^{L} \left| p \right\rangle . \tag{3.20}$$

And since $\overline{W} \left| p \right\rangle = \left| p^{\mathrm{loc}} \right\rangle$, where $\left| p^{\mathrm{loc}} \right\rangle$ is the incident field in the local coordinates of the system, the following equation can be deduced:

$$\sigma_{\mathrm{sca}} = \frac{4\pi}{k_{\mathrm{b}}^2} \left\langle p^{\mathrm{loc}} \right| \overline{\tau}^{\dagger}\, \overline{W}^{\dagger}\, \overline{W}\, \overline{\tau} \left| p^{\mathrm{loc}} \right\rangle . \tag{3.21}$$

By using the same approach as described in the previous section, we arrive at:

$$\sigma_{\mathrm{sca}} = \frac{4\pi}{k_{\mathrm{b}}^2} \sum_{\mathrm{j}} \sum_{\mathrm{i}} \eta_{\mathrm{i}}^{\mathrm{loc}} \eta_{\mathrm{j}}^{\mathrm{loc}*} \left\langle p^{\mathrm{loc}} \middle| y_{\mathrm{j}}^{\mathrm{loc}} \right\rangle \left\langle y_{\mathrm{i}}^{\mathrm{loc}} \middle| p_{\mathrm{i}}^{\mathrm{loc}} \right\rangle \left\langle x_{\mathrm{i}}^{\mathrm{loc}} \right| \overline{W}^{\dagger}\, \overline{W} \left| x_{\mathrm{j}}^{\mathrm{loc}} \right\rangle . \tag{3.22}$$

Here, superscript loc denotes the corresponding value in the local coordinates system. In contrast to Eq. 3.11, the cross term in Eq. 3.22 contains the information of the position of each scatterer in $\overline{W}^{\dagger}\overline{W}$. This can be understood easily as the description of the modes from one coordinate system to the other coordinate system needs to be transformed first to the respective coordinate system of the other scatterer.

Following the discussion in the previous section, the terms in Eq. 3.22 describes the modal strength (η_{i}), the projection parameter ($\left\langle p^{\mathrm{loc}} \middle| y_{\mathrm{j}}^{\mathrm{loc}} \right\rangle$), and the cross coupling between the modes i and j ($\left\langle x_{\mathrm{i}}^{\mathrm{loc}} \right| \overline{W}^{\dagger}\, \overline{W} \left| x_{\mathrm{j}}^{\mathrm{loc}} \right\rangle$) in the local coordinates of each scatterer, respectively. Note that, in the case of single particle system, the value of $\overline{W}^{\dagger}\, \overline{W}$ is an identity matrix, and the decomposition in the local coordinates system is exactly the same as in the corresponding global coordinates system.

In extension to the aspects discussed in the previous section, we will start by considering again the dimer structure, as described in Fig. 3.2 (a). By using the formalism in local coordinates and limit ourselves in dipole approximation, the modal strength of each mode from this structure can be obtained, as shown in Fig. 3.8 (a). In contrast to the modes obtained from the T-matrix in global coordinates, 4 distinct modes can be observed. The fourth mode, which doesnt appear in the global coordinates formalism, corresponds to a mode where the electric dipole orientations in each sphere point in opposite directions, forming an electric quadrupole in global coordinates. Since we limit ourselves to the dipole approximation, this mode did not appear when expressing the T-matrix in the global coordinate system in dipole approximation. However, when expressing the problem in the T-matrix in local coordinates and using dipole approximation, this mode can be observed as it can be expressed in a suitable excitation of the electric dipoles in each sphere. Another notable difference is the value of modal strength that is comparable now for each of the modes. This can be explained with the expression of the problem in local coordinates while relying mostly on the electric dipole moments in each

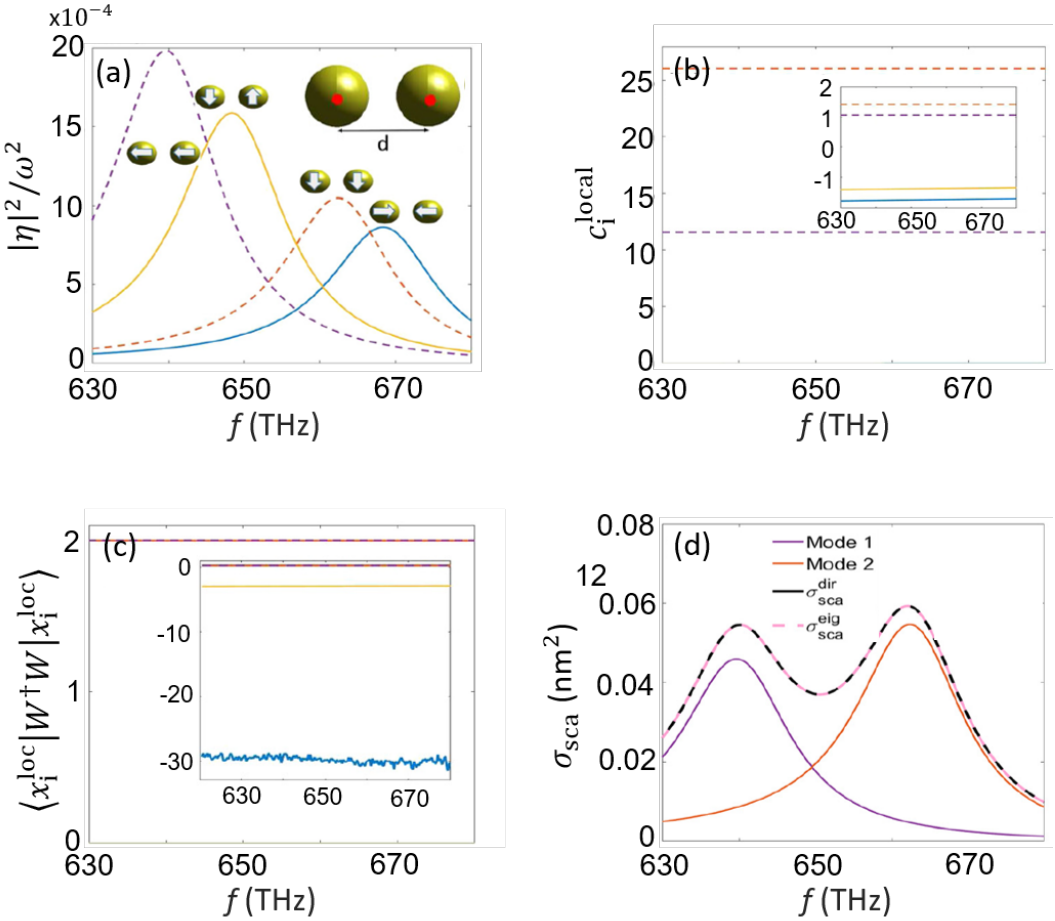

Figure 3.8 *(a) Modal strength of each modes obtained from the T-matrix in local coordinates. The red dots denote the center of the coordinate systems used to calculate the T-matrix of each sphere. (b) Projection parameter of the incident field described in Fig. 3.2 (a) onto the eigenmode of the T-matrix. (c) Self coupling term* $\left\langle x_i^{loc}\middle|\,\overline{W}^\dagger\;\overline{W}\,\middle|x_i^{loc}\right\rangle$ *for each eigenmode. The inset shows the same values in a logarithmic scale. (d) The decomposition of the scattering cross-section into the contribution from each eigenmode of the structure in local coordinates. Comparison to direct solution is also shown here and a perfect agreement is found. Adapted from P.2.*

sphere, that tend to be comparable.

Figure 3.8 (b) shows the projection of the incident plane wave onto each of the modes. It can be observed that the projection parameter in the local coordinates system for the modes denoted by purple and orange colors are several order of magnitudes larger compared to the other two modes. This means that these two modes can be excited easily by using the plane wave described in Fig. 3.8 (a). This is not surprising considering the fact that for these modes, the dipoles in each sphere are excited in phase and the incident field across the particle shows nearly no phase variation. The modes where the dipoles are oriented out of phase are therefore only weakly excitable.

Next, we also show the contribution of the coupling term, which constitutes the last term in Eq. 3.22. Here, contrary to the coupling term from the EVD of the T-matrix in the global coordinates, which is described in Eq. 3.11, the coupling term will not be one for the same mode. This is because the additional operator $\overline{W}^{\dagger}\overline{W}$, in general is not a unitary operator. This operator is a unitary matrix if and only if the number of coordinate system is one, which correspond to the global coordinate T-matrix. Due to the fact that this coupling term is not one even when considering the same mode, we will call this term a self-coupling term. The contribution from the self-coupling term of each mode, $\left\langle x_{\mathrm{i}}^{\mathrm{loc}} \middle| \overline{W}^{\dagger}\ \overline{W} \middle| x_{\mathrm{i}}^{\mathrm{loc}} \right\rangle$ are presented in Fig. 3.8 (c). The self coupling terms of the modes denoted by red and purple color, are quite large (several order of magnitudes) compared to that of the other two modes. For the electric quadrupole mode, however, the self-coupling term is almost zero, suggesting that the signature originated from this mode in the scattering cross-section might be very weak. This is because, according to Eq. 3.22, the contribution from each mode depends on three factors: modal strength, projection parameter, and coupling term. As the first and last terms are independent parameters that do not depend on the incident field, they denote the intrinsic properties of the scatterer. For this mode to appear in the scattering cross-section, careful tuning of incident field is required to balance the effect of the self-coupling term.

Finally, by multiply the results described in Figs. 3.8 (a)-(c), the contribution of each mode to the scattering cross-section can be obtained, as shown in Fig. 3.8 (d). Here, we focus only on the purple and red modes, as their corresponding projection parameters and self-coupling terms are several order of magnitudes larger compared to the other modes. When multiplying all factors, we only need to consider these two modes, as the result of the multiplication will be dominant compared to the other two. Based on these results, it is possible to track the origin of the peaks observed in the scattering cross-section to the resonance position of the two dominant modes involved.

As in the previous section, here we will also validate the spectral positions of the modes obtained from the T-matrix in local coordinates with the resonance frequencies as predicted from the hybridization theory. For this purpose, in Fig. 3.9, we show the comparison between the resonance frequency of each mode for different interparticle separations and the resonance positions obtained from hybridization theory as described in Eq. 3.14. We observe that the resonance frequency of all four distinct modes obtained from EVD of the T-matrix in local coordinates matches perfectly with the resonance frequency obtained from hybridization theory. Also, the mode that was missing in Fig. 3.3 (denoted by blue line) can also be observed due to the fact that the T-matrix in local coordinates describes the multipolar component of each individual constituent in the ensemble with the necessary accuracy.

After introducing the method and clarifying its range of applicability, now we will apply the approach of the modal analysis using EVD of T-matrix in local coordinates to a meta-atom of interest. For this purpose, as our building block, we consider the cluster of spheres mentioned in previous section (as described in Fig. 3.4), and in particular we will consider a dimer structure made of two of such clusters, as described in Fig. 3.10. The T-matrix in global coordinates of each cluster is calculated first, as described in the previous section. By using this "effective"

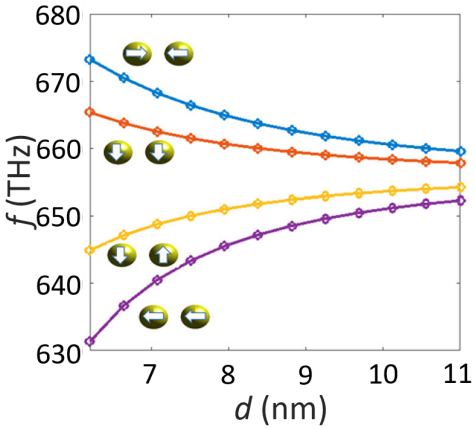

Figure 3.9 *Comparison of the resonance frequency of each mode obtained by using the T-matrix in local coordinates (dot) and hybridization theory (straight lines) for various center to center distances d. Adapted from P.2.*

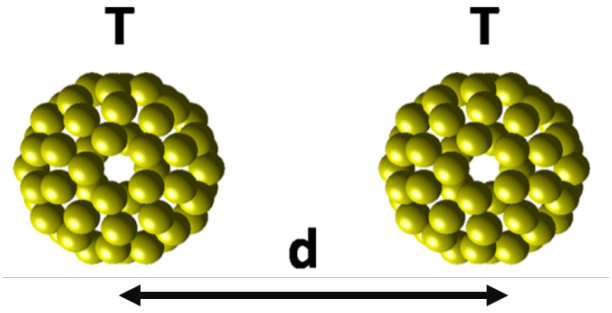

Figure 3.10 *Schematic description of two clusters of spheres spearated by a distance d which are considered in this section. Each cluster is made from 60 gold nanoparticles, and each is modelled by calculating the T-matrix with respect to their center of mass. This T-matrix is later used to build T-matrix in local coordinates. Adapted from P.2.*

T-matrix and employing Eq. 2.41, the T-matrix in local coordinates of two clusters can be obtained. This allows us to build in our analysis on the effective T-matrix of the cluster of spheres.

We will focus in this discussion on the hybridization of the modes with a dominant electric or magnetic dipolar contribution obtained by using expansion order 4 for the T-matrix in the global coordinate system of each cluster, as discussed in the previous section. The corresponding modes are denoted by straight blue and red lines in Fig. 3.5 (a). For this purpose, we present in Fig. 3.11 all four possible scenarios of modes hybridization of dipole modes of two identical cluster of spheres. Each mode of the isolated cluster will split into four different modes. Note that, these hybridized modes are always either electric or magnetic dipole modes in the local

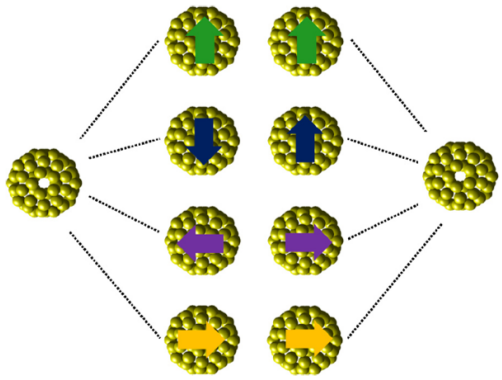

Figure 3.11 *Different possible mode hybridization scenarios for dipole modes of two clusters of spheres. Adapted from P.2.*

coordinates of each cluster. These modes always correspond to an in phase and out of phase excitation of the dipole moments in each individual cluster. The dipoles can be arranged parallel or perpendicular with respect to the connecting axis. Due to different coupling strength between these two clusters, the spectral positions of these modes depend heavily on the distance between the clusters. We will examine the modal strengths for a fixed distance first before proceeding further with the modal strengths for various distances.

The corresponding strength of the modes sustained by two cluster of spheres that are coupled at a distance of 301 nm are shown in Fig. 3.12. These modal strength have been obtained when considering the T-matrix of the coupled system in local coordinates. It can be seen that the degenerate modes (electric dipole and magnetic dipole modes) from the single cluster of spheres split into four different modes, as was also observed for the case of dimer structure. For the modes that emerge from the coupling of the magnetic dipolar modes supported in each of the clusters (shown in the dashed lines in the figure), the response is rather simple to analyze, as the modal strengths that emerge upon hybridization still retain a Lorentzian shape. For the modes that emerge from the coupling of the electric dipolar modes supported in each of the clusters (shown in the solid lines in the figure), however, a much more complex behavior can be observed. This can be attributed to the fact that for a single cluster, the associated mode has been composed of five different resonances, as discussed in the previous section. All these different resonances tend to couple and to split simultaneously, which further complicates the discussion. Further understanding is only possible if we decompose the response again using Eq. 3.17.

By fitting the modal strength of the electric modes with Eq. 3.17, the resonance frequency of each Lorentzian can be obtained. We only focus on three most dominant Lorentzian modes, which occur at lower frequencies, as shown in Fig. 3.13 (a). The resonance frequencies of these fitted modes as a function of the distance are shown in Fig. 3.13 (a). Most notably, we observe an oscillating behavior in these resonance frequencies with respect to the distance between the two clusters. These oscillations can be attributed to constructive and destructive interference

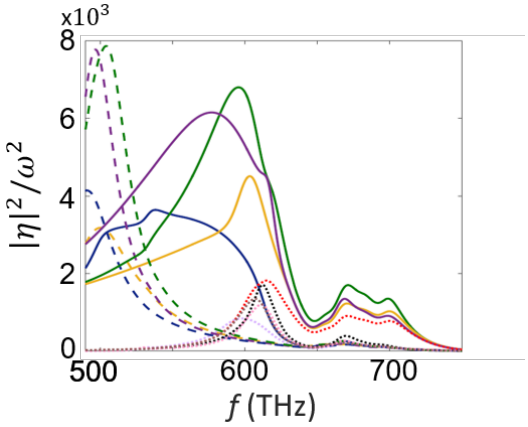

Figure 3.12 *Modal strength of each hybridized mode of two clusters of spheres with center to center distance of 301 nm. The solid (dashed) lines correspond to electric (magnetic) dipole modes, while the dotted ones show the hybridized electric quadrupole modes. The color of the dipole modes correspond to the modes described in Fig. 3.11. Adapted from P.2.*

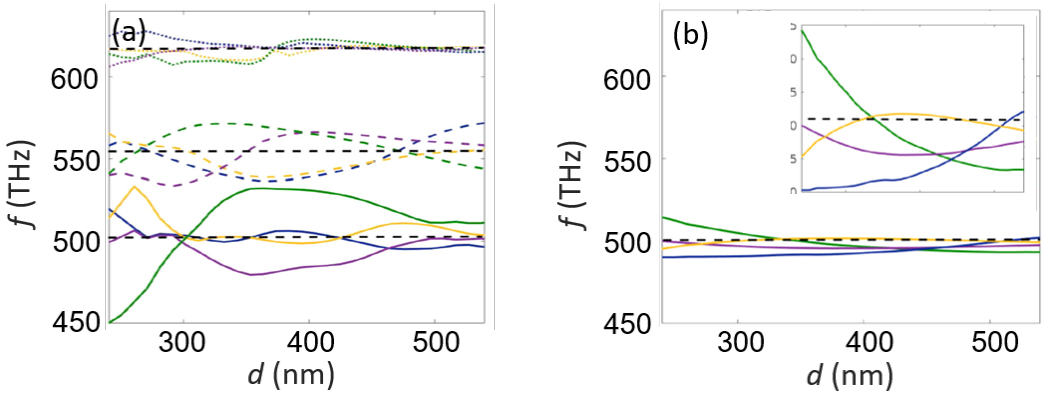

Figure 3.13 *Resonance positions of (a) three most dominant Lorentzians from the decomposition of the hybridized electric dipole modes and (b) Hybridization of magnetic dipole modes. The color of dipole modes correspond to the modes described in Fig. 3.11, while the black dashed line correspond to the resonance frequencies of the individual cluster. Adapted from P.2.*

between scattered waves from one cluster to another cluster that affects the eigenmodes, i.e. they get renormalized due to the interaction. On the other hand, Fig. 3.13 (b) shows the resonance positions of magnetic dipole modes as a function of distance between clusters. The same oscillation behavior can be observed, albeit at much smaller strength. The argument as discussed for electric dipole modes can also be applied here. The oscillation patterns are the result of the constructive and destructive interference of the waves from both clusters. For this case, it is the fields from a magnetic dipole mode that mutually interact with each other.

By comparing Fig. 3.13 (a) and (b), we can see that the distance plays quite an important role here. The impact for electric dipole modes is much stronger compared to its magnetic

counterparts. This can be seen easily from the resonance oscillations of the coupled clusters when compared to the resonance positions of the isolated cluster. They are shown in dashed lines in the figure. Whereas the resonance frequency of the dominant electric modes can shift by up to 90 THz, the magnetic modes shift only up to 25 THz. The resonance frequencies of the hybrid magnetic modes are less sensitive and less dispersive to the coupling of its nearest neighbor compared to its electric counterparts. The similar effect has also been observed in Ref[97] and then theoretically explained in Ref.[98] In these prior publications, spatial disorder had been introduced into periodically arranged meta-atoms, where each meta-atom exhibits both electric and magnetic resonance. When comparing the magnetic and electric response, the magnetic resonance indeed was quite insensitive against the disorder of the system. The reason for this reduced sensitivity can be attributed to the dominant contribution of nonradiative losses to the magnetic resonance. When comparing the total losses, less scattered field is generated for the case of magnetic resonance compared electric resonance case. This results in the effective dispersion of magnetic permeability of the metasurface is generally independent on the degree of the disorder. In our case, due to the fact that similar behavior can be observed, this means that in the case of an ensemble of meta-atom, when operated at their magnetic resonance frequency, virtually they do not see their nearest neighbors. This implies that the magnetic response of the metamaterials made from these meta-atoms does not degrade upon tight packaging. Large filling fractions can be realized without detrimental effect to its magnetic response. This is an important conclusions obtained from the analysis presented here towards the realization of densely packed self-assembled meta-atom. Keep in mind, however, this will not apply to the electric resonances that are shown previously to be quite sensitive to the presence of a nearest neighbor.

Here, we have shown that the EVD of a T-matrix in local coordinates provides a convenient way to analyze the coupling between different modes supported in each of the entity that makes up the scatterer. We have shown how to analyze the scattering cross-section of a dimer structure by decomposing it into the contribution of each mode. In contrast to modal analysis using collective modes obtained from EVD of the T-matrix in global coordinates, a self-coupling terms need to be taken into account for individual modes obtained here. We have also shown a way to understand the hybridization between modes beyond quasi-static approximation. For a large scatterer/meta-atom, an oscillating behavior of resonance frequency of each mode can be observed. This behavior can be attributed to the constructive and destructive interference of the electromagnetic waves from different scatterers that affect the eigenmodes. Finally, we have also shown that the coupling between magnetic modes is generally quite weak. This is an encouraging finding for the fabrication of metamaterials with high filling fraction, as the magnetic response of each meta-atom is almost preserved.

3.1.3 Link between collective modes and individual modes

After establishing the description of the scattering cross-sections in terms of collective modes and individual modes of an object that contributes to a larger assembly, one may asks the

following questions:

-Is there any connection between the eigenmodes in local and global coordinates?

-Is it possible to describe the modal strength obtained from the T-matrix in global coordinates into the T-matrix in local coordinates and *vice versa*?

To answer these questions, let us analyze the decomposition of the T-matrix in local coordinates in more detail. The EVD of the T-matrix in local coordinates can be written as:

$$\overline{\tau}\overline{X}_{\text{loc}} = \overline{X}_{\text{loc}}\ \overline{E}_{\text{loc}}. \tag{3.23}$$

Since $\overline{W}^L\ \overline{W} = \overline{I}$, by multiplying both sides of the above equation by $\overline{W}$, we have:

$$\overline{W}\ \overline{\tau}\ \overline{W}^L\ \overline{W}\ \overline{X}_{\text{loc}} = \overline{W}\ \overline{X}_{\text{loc}}\ \overline{E}_{\text{loc}}, \tag{3.24}$$

$$\overline{T}\ \overline{W}\ \overline{X}_{\text{loc}} = \overline{W}\ \overline{X}_{\text{loc}}\ \overline{E}_{\text{loc}}. \tag{3.25}$$

Now, by decomposing the T-matrix in global coordinates,

$$\overline{T}\ \overline{W}\ \overline{X}_{\text{loc}} = \overline{W}\ \overline{X}_{\text{loc}}\ \overline{E}_{\text{loc}}, \tag{3.26}$$

multiplying both sides with $\overline{W}^L$,

$$\overline{T}\ \overline{W}\ \overline{X}_{\text{loc}}\ \overline{W}^L = \overline{W}\ \overline{X}_{\text{loc}}\ \overline{W}^L\ \left[\overline{W}\ \overline{E}_{\text{loc}}\overline{W}^L\right], \tag{3.27}$$

and taking the EVD of the matrix in the braket, $\overline{W}\ \overline{E}_{\text{loc}}\overline{W}^L = \overline{Z}\ \overline{A}\ \overline{Z}^{-1}$, we arrive at:

$$\overline{T}\ \overline{W}\ \overline{X}_{\text{loc}}\ \overline{W}^L\ \overline{Z} = \overline{W}\ \overline{X}_{\text{loc}}\ \overline{W}^L\ \overline{Z}\ \overline{A}. \tag{3.28}$$

By looking at Eq. 3.28, it can be concluded that:

$$\overline{X}_{\text{glo}} = \overline{W}\ \overline{X}_{\text{loc}}\ \overline{W}^L\ \overline{Z}, \tag{3.29}$$

$$\overline{E}_{\text{glo}} = \overline{A} = \overline{Z}^{-1}\overline{W}\ \overline{E}_{\text{loc}}\overline{W}^L\ \overline{Z}. \tag{3.30}$$

Equations 3.29 and 3.30 show that eigenvalues and eigenvectors transformation from local to global coordinates depend on the translation operator $\overline{W}$. The matrices $\overline{Z}^{-1}\overline{W}$ and $\overline{W}^L\ \overline{Z}$ can be considered as the transformation operators, which map the modal strength from local coordinates of the individual scatterer into modal strength of the entire structure in the global coordinates. Using the same procedure, the transformation of eigenvectors and modal strength from global to local coordinates system can also be derived. The corresponding transformations are:

$$\overline{X}_{\text{loc}} = \overline{W}^L\ \overline{X}_{\text{glo}}\ \overline{W}\ \overline{V}, \tag{3.31}$$

$$\overline{H}_{\text{loc}} = \overline{V}^{-1}\, \overline{W}^{L}\, \overline{H}_{\text{glo}}\, \overline{W}\, \overline{V}, \tag{3.32}$$

where $\overline{V}$ is the eigenvectors of matrix $\overline{W}^{L}\, \overline{H}_{\text{glo}}\, \overline{W}$.

3.2 Singularvalue decomposition

In the previous section, we discussed the modes obtained from the EVD of the T-matrix. We saw that the eigenmodes obtained from such method will, in general, form a non-orthogonal basis set. This is a direct consequence from the fact that the T-matrix is a non-Hermitian matrix. This fact results in cross-coupling between the modes, as described in Eq. 3.11 or 3.22, when describing the response of the ensemble upon excitation with a plane wave. These cross terms made the decomposition of the scattering cross-section to grow quadratically with respect to the number of modes involved, as each mode has the possibility to interact with every other mode.

In this section, we will use another spectral decomposition of a matrix, that is, Singular Value Decomposition (SVD).[99] Contrary to the previous section, we will only consider the T-matrix in global coordinate for the rest of this section. In contrast to EVD, the SVD decomposes the T-matrix using two different basis sets. Mathematically speaking, the SVD of the T-matrix is

$$\overline{T} = \overline{U}\, \overline{\Sigma}\, \overline{V}^{\dagger}, \tag{3.33}$$

where $\overline{U}$ and $\overline{V}$ are singular matrices, which are orthonormal in their own space, and $\overline{\Sigma}$ is a diagonal, positive semi-definite matrix, where its diagonal components are the singular value of matrix $\overline{T}$. As in the case of EVD, the singular matrices $\overline{U}$, $\overline{\Sigma}$, and $\overline{V}$, can be written as:

$$\begin{aligned}
\overline{U} &= \begin{pmatrix} |u_1\rangle & |u_2\rangle & \cdots & \left|u_{j-1}\right\rangle & \left|u_j\right\rangle \end{pmatrix}, \\
\overline{\Sigma} &= \begin{pmatrix} |\sigma_1\rangle & |\sigma_2\rangle & \cdots & \left|\sigma_{j-1}\right\rangle & \left|\sigma_j\right\rangle \end{pmatrix}, \\
\overline{V} &= \begin{pmatrix} |v_1\rangle & |v_2\rangle & \cdots & \left|v_{j-1}\right\rangle & \left|v_j\right\rangle \end{pmatrix}.
\end{aligned} \tag{3.34}$$

Here, the singular vectors $|v_{\text{i}}\rangle$ and $|u_{\text{i}}\rangle$ are just the eigenvectors of $T^{\dagger}T$ and $TT^{\dagger}$, respectively. On the other hand, the entries of singular value matrix σ_{i} are the eigenvalues of $T^{\dagger}T$ or $TT^{\dagger}$. Using the fact that singular matrices are unitary matrices, the above decomposition can also be written as

$$\overline{T}\, |v_{\text{i}}\rangle = \sigma_{\text{i}}\, |u_{\text{i}}\rangle\,. \tag{3.35}$$

From the above equation, the singular vector $|v_{\text{i}}\rangle$ and $|u_{\text{i}}\rangle$ can be interpreted as the singular modes of the incident and the scattered fields, respectively. The physical interpretation from the above equation is that the transformation from singular modes of the incident field into

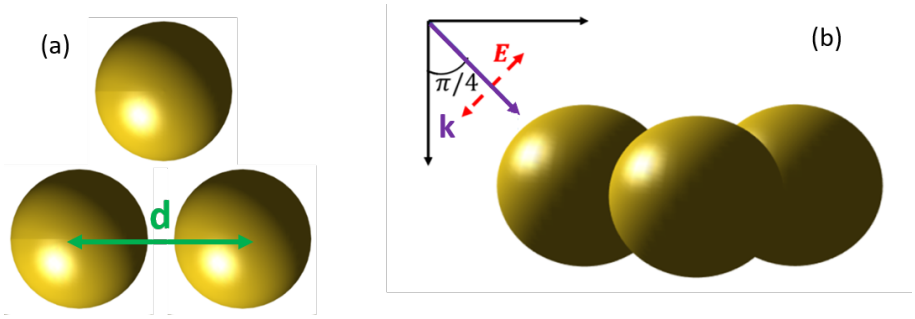

Figure 3.14 *(a) The schematic representation of the trimer structure considered in this section. The trimer consists of three identical gold nanoparticles with radius of 50 nm arranged in an equilateral triangle. The relative distance of each spheres (center to center), d, is 120 nm. (b) Side view of the trimer structure and the schematic representation of the incident field. Here, the red dashed lines (blue dashed) denotes the electric field polarization (direction of propagation). Adapted from P.1.*

singular modes of the scattered field, while the respective singular value denotes the scaling of the transformation.

Using SVD, the scattering cross-section can be written as

$$\sigma_{\text{sca}} = \frac{4\pi}{k_{\text{b}}^2} \langle p | \, \overline{T}^{\dagger} \overline{T} \, | p \rangle = \frac{4\pi}{k_{\text{b}}^2} \langle p | \, \overline{V} \, \overline{\Sigma} \, \overline{\Sigma} \, \overline{V}^{\dagger} \, | p \rangle \, . \tag{3.36}$$

From the above decomposition, the scattering cross-section can be written in summation form as

$$\sigma_{\text{sca}} = \frac{4\pi}{k_{\text{b}}^2} \sum_{\text{j}} \sigma_{\text{j}}^2 \left| \left\langle v_{\text{j}} \middle| p \right\rangle \right|^2 . \tag{3.37}$$

We can argue from Eq. 3.37 that σ_{j} can be interpreted as the modal strength of the singular modes, as this value do not depend on the incident field. This fact make it suitable to investigate properties inherent to the scatterer, i.e. properties detached from the actual incident field. If the structure cannot support a particular mode, for example, magnetic quadrupole, then the singular value which corresponds to this mode is negligible. On the other hand, the inverse is also true, if the structure supports several modes, then the singular values of the corresponding modes will be noticeable. By using these facts, it is possible to deduce which modes are dominant in a particular scatterer. If we look carefully at Eq. 3.37, compared to EVD analysis described in Eq. 3.11, no interference term appears. This is the direct consequence from the fact that SVD produces orthogonal basis sets. In consequence, SVD allows us to express the scattering cross-section with a minimal number of necessary terms.

Having finished the theoretical derivations, now it is the time to apply this type of decomposition to a specific example. Figure 3.14 (a) shows the considered trimer structure we will use as an example in this section. The trimer is made from three identical gold nanoparticles with a radius of 50 nm. These particles are arranged in an equilateral triangle. The center to center distance between gold nanoparticles is 120 nm. The permittivity of gold used here is

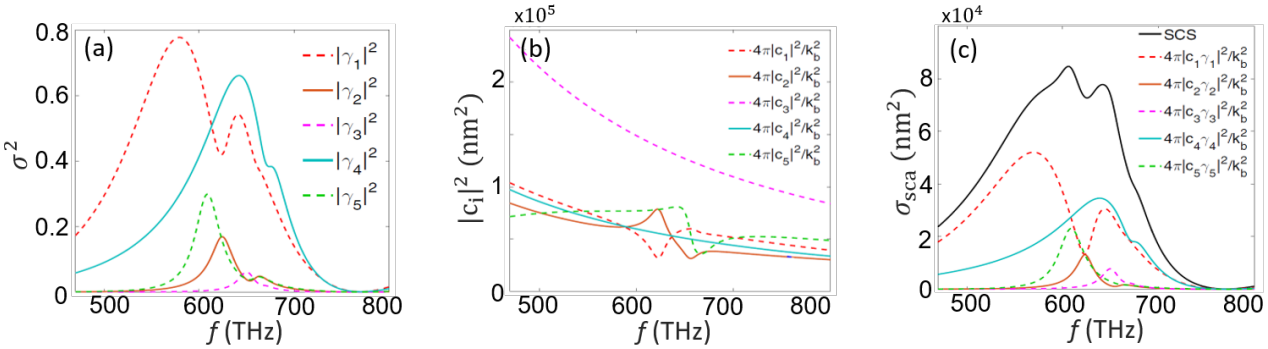

Figure 3.15 *(a) Modal strength of five dominant singular modes of trimer structure considered in this section. (b) The projection coefficients of the incident plane wave,* $|c_i|^2 = |\langle v_j | p \rangle|^2$. *(c) Decomposition of the scattering cross-section (black) into five dominant singular modes (colored). Adapted from P.1.*

given by the same Drude model as described in Eq. 3.13. The structure is illuminated with a plane wave that makes an angle of $\pi/4$ with respect to the trimer plane, as shown in Fig. 3.14 (b). The incident plane wave is polarized with its electric field as illustrated in Fig. 3.14 (b). To achieve an accuracy larger than 99 % in the spectral range of interest, we use N=4 as our expansion order. Here, the T-matrix is calculated with respect to the center of mass of the trimer structure.

Due to the fact that singular values are calculated independently at each frequency, we need a mode tracking algorithm to track the modes, as was also the case for EVD. Due to the fact that singular modes form an orthonormal basis set, we can track the modes by calculating the inner product of a selected mode at a frequency f_i and all the modes at the next frequency f_{i+1}. As the mode should change adiabatically, if frequency f_{i+1} is chosen quite close to frequency f_i, the same mode can be deduced as the mode from frequency f_i when it has the maximum inner product with the mode from frequency f_{i+1}.

As discussed before, the main strength of the SVD method lies in its ability to produce orthonormal modes. Here, we will show the implications of this aspect. For the sake of clarity, we only consider 5 most dominant singular modes, denoted by their largest singular value with respect to that of other modes, which are not shown here (larger than 10 times), as shown in Fig. 3.15 (a). As previously mentioned, singular values are properties of the scatterer, and they do not depend on the incident field impinging on the scatterer. We observe that two singular modes are very dominant (denoted by cyan and red colors) compared to the other modes. This fact suggests that these two modes will be dominant modes of the scatterer, which will most likely appear in the scattered field. The aforementioned conclusion, however, need to be taken with care. The projection of the incident field onto the singular modes of the incident field, v_i, has to be taken into account as well. Therefore, Fig. 3.15 (b) shows the projection of the incident field into singular modes of the incident field. As this component heavily depends on the incident field, there is an unlimited number of possibilities for this component. Both parameters (singular value and projection parameter) are needed to completely understand the

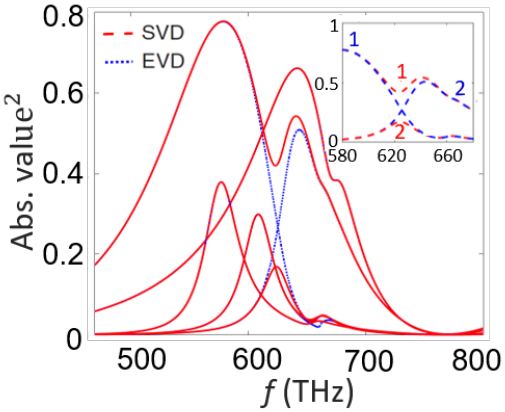

Figure 3.16 *Comparison of the modal strength obtained from SVD (red) and EVD (blue) of the T-matrix of trimer structure shown in Fig. 3.14. The inset shows different trends of the two states in the spectral region of interest, where a crossing occurs between eigenvalue, and avoided crossing for singular values. Adapted from P.1.*

response of the scatterer with a chosen incident field. This is shown in Fig. 3.15 (c), where we show the decomposition of scattering cross-section into different singular modes which are obtained from SVD approach. Due to the fact that all modes are orthogonal to each other, there's no need to consider any interference between these modes, making it easier to analyse the response. This can be attributed to the fact that the final scattering cross-section is simply the sum of the individual contribution from each mode, as described in Eq. 3.11. This results in a minimum number of terms needed, making it much more simple and appealing than EVD.

For some special cases, the absolute value of SVD and EVD will agree with each other (for example, a diagonal matrix or a Hermitian matrix). In general, however, eigenvalues and singular values of a matrix can exhibit different behaviors, as can be seen in Fig. 3.16. Here, we plot the absolute value of the singular value and the eigenvalue of the T-matrix of our trimer structure. at low and high frequencies, we observe quite similar behavior between these two values. In a specific frequency range of interest, however, they exhibit quite different behavior. Two eigenvalues are crossing around 630 THz, while for the case of singular value, an avoided crossing is observed. Due to this fact, we will put emphasis on these pairs of singular values and eigenvalues.

To understand different behavior of SVD and EVD of the pairs discussed before, further investigation of the eigenmodes and the singular modes are needed. Due to the fact that singular modes are always orthogonal, it makes sense to check the orthogonality of the eigenmode pair. By taking the inner product of both eigenmodes, mode nonorthogonality between mode 1 and 2 can be defined as:

$$\alpha_{12} = \frac{|\langle x_1|x_2\rangle|^2}{\langle x_1|x_1\rangle \langle x_2|x_2\rangle}. \tag{3.38}$$

If the modes are orthogonal to each other, the value of α_{12} will be 0. If both modes are parallel to

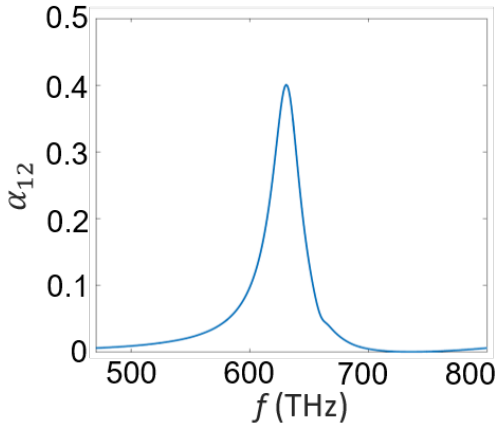

Figure 3.17 *Mode nonorthogonality of the two crossed eigenmodes. The peak observed here corresponds to the frequency where the crossing (avoided crossing) of eigenvalues (singular values) is observed. Adapted from P.1.*

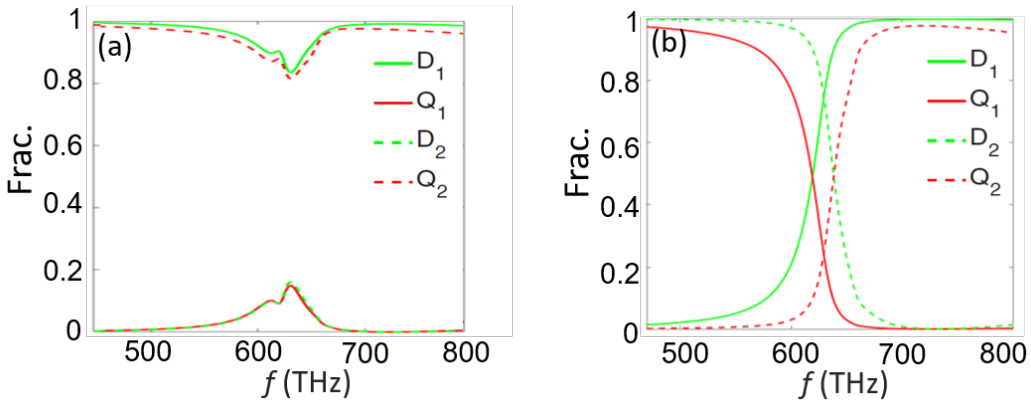

Figure 3.18 *Multipolar components of the (a) singular mode and (b) eigenmode described in the inset of Fig. 3.16. Here, D_1, D_2, Q_1, and Q_2 denote the electric dipolar and electric quadrupolar components as described in Eqs. 3.39 ans 3.40. Adapted from P.1.*

each other, the value of α_{12} is 1. The mode nonorthogonality of the selected pair of eigenmodes is shown in Fig. 3.17. The nonorthogonality between the two eigenmodes reaches its maximum at 629.3 THz, exactly where the crossing point of both modes is observed in Fig. 3.16. As the frequency goes further away, the mode nonorthogonality between mode 1 and 2 is decreases. This suggests that the modes are orthogonal to each other at lower and higher frequencies.

To understand the origin of the different behavior of the modal strength obtained from EVD and SVD of the T-matrix, we present in Fig. 3.18 the comparison of multipolar decomposition of selected modes in Fig. 3.16. We define the total moment for both of them by extracting the multipolar contribution of the corresponding modes. This extraction can be done by taking the

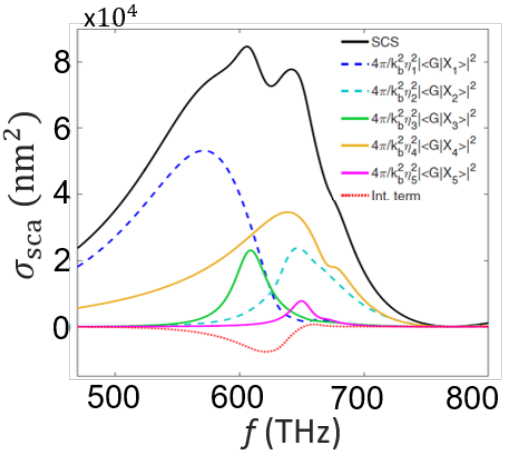

Figure 3.19 *Decomposition of the scattering cross-section (black) into eigenmodes (dashed and solid colored). Due to the coupling between nonorthogonal modes, the interference term between eigenmodes is also appearing here (red dotted). Adapted from P.1.*

VSH coefficients, Z, from the respective eigenvector or singular vector, as

$$D_{\mathrm{i}} = \sum_{\mathrm{m}=1}^{3} |Z^{\mathrm{i}}_{1\mathrm{m}1}|^2 \tag{3.39}$$

and

$$Q_{\mathrm{i}} = \sum_{\mathrm{m}=1}^{5} |Z^{\mathrm{i}}_{2\mathrm{m}1}|^2. \tag{3.40}$$

Here, D_{i}, Q_{i}, and Z^{i} denote the total electric dipole, total electric quadrupole, and the components of the eigenvectors or singular vectors. They are related to $\mathbf{N}_{\mathrm{mnk}}(\mathbf{r}, \theta, \phi)$ of eigenmodes or singular modes i, respectively. In Fig. 3.18 (a) we show the modal decomposition of the singular modes. We observed that the multipolar composition in both singular modes undergo a change around 630 THz, exactly at the avoided crossing frequency which is observed in Fig. 3.16. On the other hand, Fig. 3.18 (b) shows that for eigenmode 1, the eigenmode undergoes an adiabatic evolution from an electric dipole-dominant mode into an electric quadrupole-dominant mode while going from higher frequencies to lower frequencies. The opposite happens for eigenmode 2. This eigenmode undergoes a transition from an electric quadrupole dominant mode into an electric dipole dominant mode. For these eigenmodes, In the frequency range of 550-650 THz, both of them are starting to mix and both modes simultaneously have an electric dipole and electric quadrupole contributions around these frequencies. This transition from an electric dipole mode into an electric quadrupole mode and *vice versa* for both modes is the origin of the mode non-orthogonality behavior observed in Fig. 3.17. So basically their modal contents in this transitional region is the reason for the nonortogonality between these two modes.

Finally, the comparison of the scattering cross-section decomposition using EVD is given in

Fig. 4.24. Here, the comparison is made relative to Fig. 3.15 (c), where the same had been shown for SVD. In the case of the SVD, since the modes form an orthonormal basis set, no interference between the modes can be observed. For EVD, however, an interference effect can be observed, which is the result of cross coupling between the modes that occurs in certain ranges of frequencies (red dashed line). This is a direct consequence from the nonorthogonality of the modes (as observed in Fig. 3.17). This was described previously as Fano resonance in the literature.[85,86] Usually, Fano feature appears as a dip in the scattering cross-section, as can be seen in Fig. 4.24. Fano features are usually explained as the interference between two or more nonorthogonal modes. By using SVD, however, different way of thinking can be used to explain the observable features. Due to the fact that no interference effects emerge by default because all the modes are orthogonal, Fano features cannot be described as modes interference. Instead, it is the spectral dispersion of a specific singular mode. In the trimer case we studied, for example, the mode denoted by the singular value γ_1 in Fig. 3.15 (b) can be associated with Fano features. This means that Fano feature is an inherent properties of a single singular mode, in contrast to the results of the coupling between different modes. We now point out an advantage of using singular vectors instead of using eigenvectors. This advantage is the direct consequence of their orthogonality. The orthogonality of the singular vectors allows us to identify which illuminations cause an independent excitation of the object. For a specific spectral feature of the scattering cross-section, which corresponds to γ_1, one would have to use the corresponding singular vector (g_1) as the incident electromagnetic field. Here, we highlight that this is the only possible case of illumination scenario for such purpose. This is in stark contrast to an excitation with eigenmodes. To illustrate this point, assume we wish to use an incident field built out of the two involved eigenvectors of the T-matrix (x_1 and x_2). First, we would require the knowledge of the appropriate relative phase between them. Moreover, there would be no guarantee that the desired modes is the only modes excited by the illumination field (it will probably excite another mode which corresponds to γ_2 as well). When designing structures with strong Fano features, it might be beneficial to consider only a single quantity that is clearly given by the singular value of a specific mode. Moreover, carefully tuning the illumination to let it agree with the associated singular mode in the expansion of the incident field, might allow to observe spectrally very sharp features.

In this section, we have shown another way to extract modes from the T-matrix of a scatterer, by using singular value decomposition. In contrast to the eigenvalue decomposition, the modes obtained are always orthogonal. This is beneficial to the analysis, as less number of terms are required compared to the modes obtained from the eigenvalue decomposition. We show different spectral behavior of modal strength obtained from SVD and EVD, where a crossing or avoided crossing can be observed. These behavior can be attributed to the nonorthogonality of the eigenmodes. Finally, we put forward an argument why Fano resonances are an inherent property of singular modes, in contrast to the eigenmodes formalism, where it is the result of cross-coupling between different nonorthogonal modes.

3.3 Basis independent modes

In the previous section, we discuss the physical meaning of an eigenvalue and a singular value of the T-matrix. We come to the conclusion that they denote the modal strength of a particular mode, that is, how easy a mode can be excited, independent of the incident field. On the other hand, the projection parameter, $\langle p|x\rangle$ in case of EVD or $\langle p|v\rangle$ in case of SVD, depends on the incident field impinging upon a scatterer. So far, we used VSH as our basis set to describe the modes of our scatterer. However, since the T-matrix can also be written in any orthogonal basis set, one might ask the question about these two values (modal strength and projection parameter). Are they depend on the chosen basis set of the T-matrix, or are they independent parameters? To answer this question, we will dedicate the discussion in this section to describe the modes obtained from the T-matrix of a scatterer in different basis set of the T-matrix.

First, we consider two T-matrices which describe the same scatterer, but written in different basis set. One T-matrix, $\overline{T}_{\mathrm{a}}$, written in one particular basis set, i.e. VSH, and the other T-matrix, $\overline{T}_{\mathrm{b}}$, written in another basis set, i.e. plane waves. The transformation between these bases can be written as a matrix operation,

$$\overline{\zeta}\,|\alpha\rangle = |\beta\rangle\,, \tag{3.41}$$

where $\overline{\zeta}$ is a matrix which describes the transformation, and α and β are the basis set of the T-matrices. In case of orthonormal basis set, meaning that:

$$|\gamma\rangle\langle\gamma| = \overline{I}, \tag{3.42}$$

where $|\gamma\rangle$ can be either $|\alpha\rangle$ or $|\beta\rangle$, the operator $\overline{\zeta}$ will be a unitary operator,$\overline{\zeta}\ \overline{\zeta}^{\dagger} = \overline{I}$. The transformation between $\overline{T}_{\mathrm{a}}$ to $\overline{T}_{\mathrm{b}}$ then can be written as:

$$\overline{T}_{\mathrm{a}} = \overline{\zeta}\ \overline{T}_{\mathrm{b}}\ \overline{\zeta}^{\dagger}. \tag{3.43}$$

Now, let us consider the decomposition using EVD for both $\overline{T}_{\mathrm{a}}$ and $\overline{T}_{\mathrm{b}}$.

$$\overline{T}_{\mathrm{a}} = \overline{X}_{\mathrm{a}}\ \overline{E}_{\mathrm{a}}\ \overline{X}_{\mathrm{a}}^{-1}, \tag{3.44}$$

$$\overline{T}_{\mathrm{b}} = \overline{X}_{\mathrm{b}}\ \overline{E}_{\mathrm{b}}\ \overline{X}_{\mathrm{b}}^{-1}. \tag{3.45}$$

By employing Eq. 3.41, the eigenvectors of $\overline{T}_{\mathrm{a}}$ can be written as

$$\overline{X}_{\mathrm{a}} = \overline{\zeta}\ \overline{X}_{\mathrm{b}}. \tag{3.46}$$

By rewriting Eq. 3.43 into EVD,

$$\overline{X}_{\mathrm{a}}\ \overline{E}_{\mathrm{a}}\ \overline{X}_{\mathrm{a}}^{-1} = \overline{\zeta}\ \overline{X}_{\mathrm{b}}\ \overline{E}_{\mathrm{b}}\ \overline{X}_{\mathrm{b}}^{-1}\overline{\zeta}^{\dagger}, \tag{3.47}$$

and using the property of unitary operator and Eq.!3.46, we arrive at

$$\overline{E}_{\mathrm{a}} = \overline{E}_{\mathrm{b}}. \tag{3.48}$$

This prove that modal strength from EVD is a basis independent quantity. The same can also be derived for projection parameter of EVD. Using the similar derivations, the same conclusions can also be drawn for the modal strengths and the projection parameters obtained from SVD. Based on these, we stress here that both parameters are basis independent quantities, and the modes we discuss here are also valid for other basis sets. This is an important fact, since this means that the modes sustained by a scatterer, which can be described by any basis set, always end up describing the same mode, irrespective of the basis set chosen to describes the modes, provided that the corresponding basis sets are orthonormal.

3.4 Summary

In this chapter, we have shown that the analysis of the optical responses from meta-atoms can be done conveniently by decomposing the response in terms of modes. Using EVD, collective modes of the scatterer can be obtained from the T-matrix in global coordinates. Subsequently, by applying EVD to a T-matrix in local coordinates, individual modes can be defined. Here, the eigenvalue denotes the modal strength of the modes while the eigenvector contains multipolar information of the modes.

On the other hand, using SVD, an orthogonal set of modes can be defined. As opposed to EVD, the modes obtained from SVD resulted in singular modes of incident field and singular modes of scattered field. Here, singular value of the T-matrix can be interpreted as modal strength of the corresponding singular modes. Finally, a comparison between modes obtained from EVD and SVD has been shown and different interpretation of Fano resonance can be made depending on the choices of modes definition. Finally we have shown that the mode descriptions we presented in this chapter are basis independent modes.

Some of the results presented here will be used as ingredients in the next chapter. The discussion of Fano-resonance in section 4.2 will heavily be based on modes which are defined in this chapter.

Chapter 4

4 Optics of Self-assembled Metamaterials

In this chapter, we will discuss the application of the T-matrix method to discuss the properties of metamaterials fabricated using self-assembly techniques. In the first section, we will dedicate our discussion to the experimentally observable parameters characterizing the optical response of bulk metamaterials fabricated using self-assembly techniques. In particular, we show, given a sufficient dillution, how they can be extracted directly from the T-matrix of the individual meta-atom constituent if an unpolarized illumination is considered. Following this discussion, we will continue with the discussion of the experimentally observable quantities, which explicitly depend on the polarization of incident field. The polarization dependent parameters will also be extracted from the T-matrix of its constituent meta-atom.

In the second section of this chapter, we will discuss the observables features of Fano resonances in metamaterials fabricated using self-assembly techniques. By employing the modal decomposition introduced in the previous chapter, we will quantify Fano properties of self-assembled metamaterials. For that we rely on a description of the optical response of self-assembled metamaterials in terms of mode-coupling of its constituent meta-atom.

The content of this chapter is mostly based on P.4 (section 4.1) and P.7 (section 4.2.1).

4.1 Extracting the experimental parameters from the T-matrix of meta-atom

In general, metamaterials fabrication can be divided into two distinct fabrication methods, top-down and bottom-up approaches.[100] In top-down approaches, the structure is fabricated from an exact image/data. It starts mostly from a bulk material into which the desired geometry is engraved using a suitable technology. Most often, this is done with lithography-based approaches, such as electron beams,[101,102] ion beams[103,104] or direct laser writing[24,35] procedure. In all of these cases, the shape and position of each meta-atom are usually well-defined in a deterministic sense during the design process and these design parameters are then realized in the fabrication.

On the other hand, bottom-up approaches usually rely on done by using chemical based approach, such as colloidal chemistry. Most often, they exploit the minimization of the interaction energy between ingredients of the meta-atom (such as chemical potential,[105] electrostatic potential,[106] template based approach[107,108] and so on) to cause the formation of a more complicated structures out of basic ingredients. For that reason, bottom-up approaches are often called

self-assembly approaches. The reason why colloidal chemistry i.e. essentially small metallic nanoparticles, is used is also quite simple. Generally, a strong response of the emerging materials is desirable. This prompts to exploits resonances in the optical response. As we do not have control over the precise structural arrangement of the material to be fabricated, bottom-up metamaterials cannot rely on resonances induced by, e.g., a periodic arrangement of a weakly scattering structure. Instead, the basic building blocs themselves should already offer the desired resonant scattering properties. Here, small metallic nanoparticles are perfect candidates. Due to high density of free electrons, localized surface plasmon polaritons can be induced at discrete frequencies, where the interaction is strongly enhanced with the external illumination. By arranging these nanoparticles in more complicated shapes give rise to the scattering effects that are at stake in this chapter. However, due to the random nature of this fabrication process, the resulting meta-atoms are usually limited to highly symmetric objects and the metamaterials are, most likely, isotropic.[100]

The theoretical analysis of the optical response of metamaterials made from top-down approaches is often quite straightforward, because each meta-atom fabricated with this method has well-defined form and position.[36,109–111] Due to this reason, a well defined incident field and its polarization state can be used to extract the experimentally observable quantities of such metamaterials, as described in Fig. 4.1 (a). Additionally, they are usually also periodically arranged in space, which allows us to focus in the analysis on a single unit cell only and exploiting some periodic boundary conditions. This is obviously a huge simplification. On the other hand, metamaterials fabricated using bottom-up approaches always end up with much larger uncertainty in the position and the orientation of the meta-atoms.[27,112,113] Due to this limitation, the averaging procedure is often used to describe the optical response of the entire ensemble by using rotational averaging procedure.[114,115] This approach is valid in the case of strongly diluted meta-atoms. The validity can be attributed to the fact that since the distance between meta-atoms is very large, the interaction between meta-atoms can be ignored in the lowest order approximation. This can be understood from the Born approximation point of view, where the incident field at one particle can be written as:

$$\mathbf{E}^{\mathrm{inc}}_{\mathrm{total}}(\mathbf{r},\omega) = \mathbf{E}^{\mathrm{inc}}_{\mathrm{ori}}(\mathbf{r},\omega) + \mathbf{E}^{\mathrm{inc}}_{1}(\mathbf{r},\omega) + \mathbf{E}^{\mathrm{inc}}_{2}(\mathbf{r},\omega) + \cdots \tag{4.1}$$

where $\mathbf{E}^{\mathrm{inc}}_{\mathrm{total}}(\mathbf{r},\omega)$ denotes the total incident field at one particle, and the subscripts on the right side denote the original incident field (ori), incident field from other particle after one scattering event (1), two scattering events (2), and so on. In case of very diluted scenario, we assume that the first term $\mathbf{E}^{\mathrm{inc}}_{\mathrm{ori}}(\mathbf{r},\omega)$ is enough to describes the incident field. For higher density, higher order corrections need to be taken into account, which is outside of the scope of this thesis.

For the case of very diluted metamaterials, the rotationally averaged properties can be used to describe the optical response of the metamaterials made from self-assembly approach, as shown in Fig. 4.1 (b). This is done by calculating the response over all possible directions of the incident field and then averaging these responses with respect to the number of illuminations. This

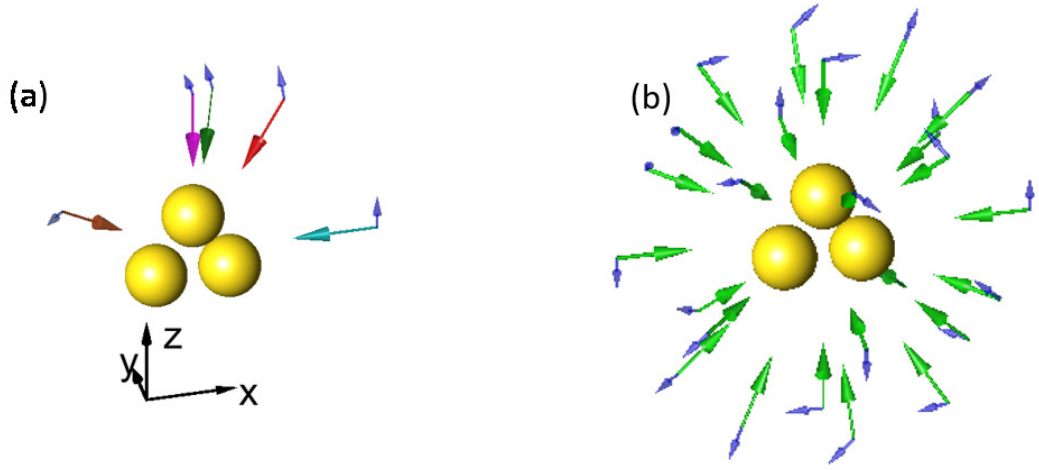

Figure 4.1 *(a) Illustration of different incident fields of a single meta-atom, a trimer structure in this case. (b) Multiple incident field scenarios to describe the response of metamaterials made from self-assembly approach. In a zeroth order approximation, the response can be deduced by taking a rotatonally average value over all possible illumination and polarization directions. For each incident field, the blue semitransparent arrow denotes the electric field, while other color denotes its wavevector. Adapted from P.7.*

approach, however, is often time consuming and computationally expensive. This is because one needs to calculate the optical response from all directions and then average it. To overcome this limitation, in this section, we will show that it is possible to extract the experimental parameters directly from the T-matrix of the meta-atom itself, as discussed in P.4.

4.1.1 Incident field is unpolarized

It is quite common in an experimental set up, and especially in real life, that the incident field has no definite polarization. It is therefore desirable to be able to predict the optical response in a scenario of the incident field is randomly polarized, or in other words, the average response of randomly polarized incident fields is considered. For this purpose, we will show that the rotationally averaged responses can be deduced directly from the T-matrix of the constituent meta-atom without the need to do manual averaging procedure.

First, let us start from a single illumination scenario, where the incident field is a plane wave with a certain propagation direction k. The scattering cross-section ($\sigma_{\mathrm{sca}}^{\mathrm{k}}$) resulted from this incident field can be written as:[66,116]

$$\sigma_{\mathrm{sca}}^{\mathrm{k}} = \frac{4\pi}{k_{\mathrm{b}}^2} \left\langle a^{\mathrm{k}} \middle| a^{\mathrm{k}} \right\rangle , \tag{4.2}$$

where superscript k denotes the index for a particular illumination k and k_{b} denotes the

wave number inside the background medium, which is defined as $k_\mathrm{b} = \frac{2\pi n_\mathrm{b}}{\lambda_0}$, where λ_0 is the wavelength of the electromagnetic field in vacuum and n_b is the background refractive index. By employing the T-matrix definition as written in Eq. 2.24, we arrive at the following equation:

$$\sigma_\mathrm{sca}^\mathrm{k} = \frac{4\pi}{k_\mathrm{b}^2} \left\langle p^\mathrm{k} \right| \overline{T}^\dagger \, \overline{T} \left| p^\mathrm{k} \right\rangle . \tag{4.3}$$

In a next step we transform the inner product as described above into the outer product of a matrix:[77]

$$\sigma_\mathrm{sca}^\mathrm{k} = \frac{4\pi}{k_\mathrm{b}^2} \mathrm{Tr} \left[\overline{T}^\dagger \, \overline{T} \left| p^\mathrm{k} \right\rangle \left\langle p^\mathrm{k} \right| \right], \tag{4.4}$$

where $\mathrm{Tr}[\cdots]$ denotes the trace of a matrix. Rewriting the above equation in compact form, we arrive at

$$\sigma_\mathrm{sca}^\mathrm{k} = \frac{4\pi}{k_\mathrm{b}^2} \mathrm{Tr}[\overline{T}^\dagger \, \overline{T} \, \overline{X}^\mathrm{k}], \tag{4.5}$$

where $\overline{X}^\mathrm{k} = \left| p^\mathrm{k} \right\rangle \left\langle p^\mathrm{k} \right|$. The above equation expresses the scattering cross-section for a specific illumination in matrix form. By taking the average across multiple illumination scenarios, the following equation will hold:

$$\sigma_\mathrm{sca}^\mathrm{aver} = \frac{4\pi}{k_\mathrm{b}^2} \frac{1}{\mathrm{K}} \sum_{\mathrm{k}=1}^{\mathrm{K}} \mathrm{Tr}[\overline{T}^\dagger \, \overline{T} \, \overline{X}^\mathrm{k}] = \frac{4\pi}{k_\mathrm{b}^2} \mathrm{Tr} \left[\overline{T}^\dagger \, \overline{T} \frac{1}{\mathrm{K}} \sum_{\mathrm{k}=1}^{\mathrm{K}} \, \overline{X}^\mathrm{k} \right]. \tag{4.6}$$

Since the vector matrix $\left| p^\mathrm{k} \right\rangle$ is a normalized vector composed of the expansion coefficients of the incident field, for a random polarization scenario, this vector will be a random, normalized vector. Using this fact and by assuming that K is a very large number, the following relation will hold:[117]

$$\frac{1}{\mathrm{K}} \sum_{\mathrm{k}=1}^{\mathrm{K}} \overline{X}^\mathrm{k} = \overline{I}, \tag{4.7}$$

where $\overline{I}$ is the identity matrix. Using this fact, the rotationally averaged scattering cross-section can be written as:

$$\sigma_\mathrm{sca}^\mathrm{aver} = \frac{4\pi}{k_\mathrm{b}^2} \mathrm{Tr}[\overline{T}^\dagger \, \overline{T}]. \tag{4.8}$$

The rotationally averaged extinction cross-section can also be derived in the same way. First, we start from the definition of the extinction cross-section:

$$\sigma_\mathrm{ext}^\mathrm{k} = \frac{4\pi}{k_\mathrm{b}^2} \, \mathrm{Re} \left(\left\langle p^\mathrm{k} \right| a^\mathrm{k} \right\rangle \Big) = \frac{4\pi}{k_\mathrm{b}^2} \, \mathrm{Re} \left(\left\langle p^\mathrm{k} \right| | \overline{T} \left| p^\mathrm{k} \right\rangle \right). \tag{4.9}$$

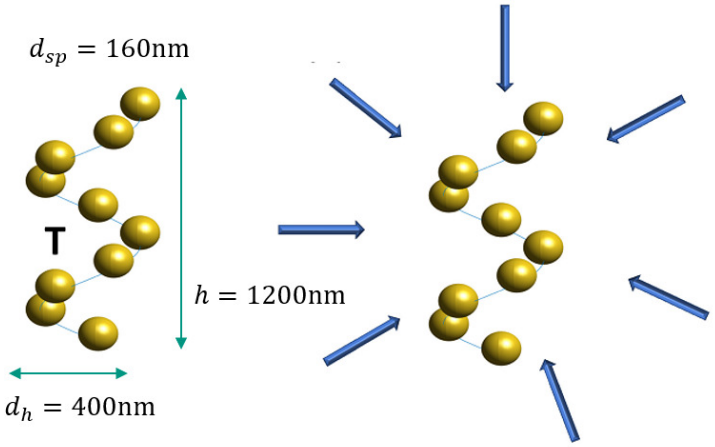

Figure 4.2 *Illustration of the considered helical meta-atom used as structural example in this section. The averaging is done either by direct extraction from the T-matrix (left) or with multiple incident field scenarios. The meta-atom consists of 10 gold nanoparticles with a radius of 80 nm arranged in a helix and embedded in water. The helix has a total height of 1200 nm and a radius of 200 nm. It consists of 2 pitches. Adapted from P.4.*

While following the same procedure as described above, we end up at:

$$\sigma_{\text{ext}}^{\text{aver}} = \frac{4\pi}{k_{\text{b}}^2} \operatorname{Re} \operatorname{Tr}[\overline{T}]. \tag{4.10}$$

Since the absorption cross-section is defined as $\sigma_{\text{abs}} = \sigma_{\text{ext}} - \sigma_{\text{sca}}$, the average absorption cross-section can be written as:

$$\sigma_{\text{abs}}^{\text{aver}} = \frac{4\pi}{k_{\text{b}}^2} \operatorname{Re} \left(\operatorname{Tr}[\overline{T} \ \{\overline{I} - \overline{T}\}^{\dagger}] \right). \tag{4.11}$$

After we are done with the derivations of the average properties, now it is time to compare the values obtained from these derived formulas with the results obtained from manually averaging the response of meta-atom. For this purpose, we will consider 10 identical gold nanoparticles with radius of 80 nm arranged in a helix with two pitches as our meta-atom. The distance among neighboring gold nanoparticles along the helix is always identical. The helix has a total height of 1200 nm and a radius of 200 nm, as shown in Fig. 4.2. This chosen meta-atom is immersed in a water solution with background refractive index, n_{b}, of 1.33. To achieve a good convergence of the parameter extraction from the T-matrix, we use the expansion order $N = 4$. The obtained results will then be compared to the results obtained from the manual averaging procedure, which is done for different number of illuminations (NI). We use in the manual averaging procedure, either 1600 or 12100 plane waves for the illumination. The incident fields are always plane waves and their direction of propagation is randomly chosen. These random directions of propagation are generated by using a random number generator to generate two parameters, the polar (θ) and azimuthal (ϕ) angles. The polar angle can be any real number

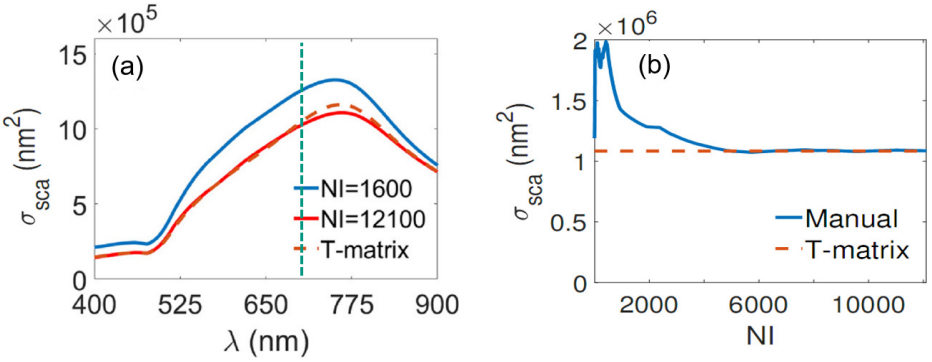

Figure 4.3 *(a) Rotationally averaged scattering cross-section calculated by two different numbers of incident field scenarios, as denoted by the blue and red line.The comparison is made with values obtained directly from the T-matrix (brown dashed line), showing a good agreement for a sufficient large number of incident field scenarios. (b) Convergence analysis of rotationally averaged scattering cross-section at one selected wavelength (730 nm). The brown dashed line denotes the value obtained from T-matrix. Adapted from P.4.*

between $-\frac{\pi}{2}$ to $\frac{\pi}{2}$, while the azimuthal angle can be any real number between 0 to 2π. Using these parameters, we define the incident field direction $\mathbf{k}$ as $\mathbf{k} = [k_\mathrm{x}\ k_\mathrm{y}\ k_\mathrm{z}] = k_\mathrm{b}[\sin\theta\cos\phi\ \sin\theta\sin\phi\ \cos\theta]$. For each incident wavevector, we consider 5 different linear polarizations by rotating the electric field of a particular incident field evenly, with the rotation angle of 0.4π. The cross-sections from each direction are then weighted with the factor of $\cos\theta$. The comparison of the results obtained from manual averaging method as described here will then be compared to the results obtained from the direct extraction from the T-matrix.

Figure 4.3 (a) shows the rotationally averaged extinction cross-section of the meta-atom described in Fig. 4.2. From both methods (manual averaging and direct parameters extraction from the T-matrix), two peaks can be observed. A dominant peak around 775 nm and a hardly visible peak around 525 nm. The peak at 525 nm can be attributed to the resonance position of the electric quadrupole mode of each individual gold nanosphere, which resonates at 542 nm. The shift can be attributed to the coupling between different particles. On the other hand, the dominant peak at 775 nm can be attributed to the electric dipole mode of each particle, which resonates at 673 nm. Due to the fact that the radiation field of the electric dipole is usually stronger than the one produced by the electric quadrupole, stronger coupling between particles around this wavelength can be expected. This strong coupling will induce larger resonance shift, and, therefore, we observe larger shift of this mode compared to its quadrupole counterpart.

By comparing the rotationally averaged scattering cross-section in Fig. 4.3 (a), we see that for a smaller number of plane waves used for the averaging procedure, we still see a notable quantitative disagreement for the values obtained directly from the T-matrix and the direct averaging method. For a larger number of incident field scenarios, however, a very good agreement can be found. This fact can be seen in more details in Fig. 4.3 (b). There,we plot the averaging value of the scattering cross-section at the wavelength of 730 nm for different numbers of illumination (NI) scenarios. At the beginning, large discrepancies between both methods occur. However,

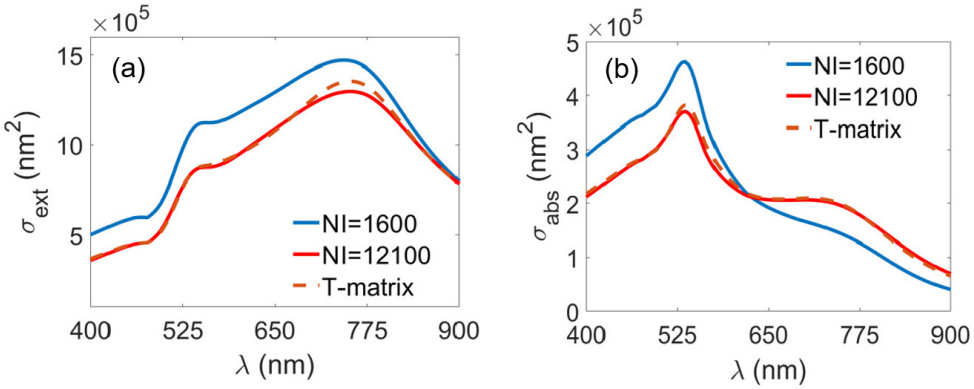

Figure 4.4 *Rotationally averaged (a) extinction cross-section and (b) absorption cross-section of gold nanospheres arranged in a helical structure. Blue and red straight lines denote the values obtained from manually averaging the response for different incident field scenarios while the brown dashed lines are values obtained directly from the T-matrix. Adapted from P.4.*

as the NI increases, the predicted value for the scattering cross-section obtained from the direct averaging procedure approaches the value obtained directly from the T-matrix.

By applying Eqs. 4.10 and 4.11, the rotationally averaged extinction and absorption can be obtained as well, as shown in Fig. 4.4. Once again, we compared the values obtained directly from the T-matrix and the values obtained from manual averaging with different NI scenarios. For a sufficient high number of incident field, the results from the manual averaging method match quite perfectly with the results extracted directly from the T-matrix. Based on these facts, we can conclude that the direct parameter extraction from the T-matrix offers a powerful and credible way to calculate the rotationally averaged responses of the meta-atom, which can be used to describe the responses of the ensemble of meta-atoms.

In this section, we have shown a formalism to predict the rotationally averaged responses of a meta-atom based on its T-matrix. These rotationally averaged responses correspond to the response of the self-assembled metamaterials made from the ensemble of this meta-atom.

4.1.2 Incident field has a well-defined helicity

The results presented in the previous section allow us to calculate the cross-sections of self-assembled metamaterials with a randomly polarized incident field, which we deduce from the T-matrix of its meta-atom constituent, in a very convenient way. For several number of applications, however, it is desirable to use a well-defined polarized incident field instead of a randomly polarized field.[118] Therefore, it is also important to be able to deduce the experimentally observable parameters that depend on the polarization of the incident field in a straightforward way as described in the previous section. For this purpose, we will show how to derive cross-sections if the incident field has a certain and well defined polarization. We will restrict ourselves to circularly polarized field, but the derivation can also be used for other type of polarization,

provided that the corresponding T-matrix is transformed into the respective basis set of the polarized field. In the helicity basis, the T-matrix can be written as:

$$\begin{pmatrix} \overline{T}_{\mathrm{LL}} & \overline{T}_{\mathrm{LR}} \\ \overline{T}_{\mathrm{RL}} & \overline{T}_{\mathrm{RR}} \end{pmatrix} = \frac{1}{2} \begin{pmatrix} \overline{I} & \overline{I} \\ \overline{I} & -\overline{I} \end{pmatrix} \begin{pmatrix} \overline{T}_{11} & \overline{T}_{12} \\ \overline{T}_{22} & \overline{T}_{22} \end{pmatrix} \begin{pmatrix} \overline{I} & \overline{I} \\ \overline{I} & -\overline{I} \end{pmatrix}. \tag{4.12}$$

The subscript L and R denote left and right circular polarization components of the T-matrix. The T-matrix at the left side denotes the T-matrix in the helicity basis while the T-matrix in the right side denote the T-matrix in the parity basis, as described as in Eq. 2.33. Armed with this transformation, now we are ready to describe the rotationally averaged responses of a meta-atom.

First, we will start by considering right circularly polarized (RCP) incident field. By restricting the incident field to only a RCP component, the following equation will hold:

$$\begin{pmatrix} \overline{T}_{\mathrm{LL}} & \overline{T}_{\mathrm{LR}} \\ \overline{T}_{\mathrm{RL}} & \overline{T}_{\mathrm{RR}} \end{pmatrix} \begin{pmatrix} 0 \\ |p_{\mathrm{R}}\rangle \end{pmatrix} = \begin{pmatrix} |a_{\mathrm{L}}\rangle \\ |a_{\mathrm{R}}\rangle \end{pmatrix}. \tag{4.13}$$

The scattering cross-section, therefore, can be written as:

$$\sigma_{\mathrm{sca}}^{\mathrm{k}} = \frac{4\pi}{k_{\mathrm{b}}^2} \left[\langle a_{\mathrm{L}} | a_{\mathrm{L}} \rangle + \langle a_{\mathrm{R}} | a_{\mathrm{R}} \rangle \right] = \frac{4\pi}{k_{\mathrm{b}}^2} \left[\langle p_{\mathrm{R}} | T_{\mathrm{LR}}^{\dagger} T_{\mathrm{LR}} | p_{\mathrm{R}} \rangle + \langle p_{\mathrm{R}} | T_{\mathrm{RR}}^{\dagger} T_{\mathrm{RR}} | p_{\mathrm{R}} \rangle \right]. \tag{4.14}$$

By applying the same procedure described in the previous section, the rotationally averaged scattering cross-section for RCP light as an incident field can be written as:

$$\sigma_{\mathrm{sca}}^{\mathrm{aver}} = \frac{4\pi}{k_{\mathrm{b}}^2} \mathrm{Re} \left(\mathrm{Tr} \left[T_{\mathrm{LR}}^{\dagger} T_{\mathrm{LR}} + T_{\mathrm{RR}}^{\dagger} T_{\mathrm{RR}} \right] \right). \tag{4.15}$$

The other rotationally averaged cross-sections can also be derived in the same way. Table 4.1 lists all rotationally averaged cross-sections for RCP and LCP as the incident field. Note that, the circular dichroism (CD) is usually defined as the difference of the attenuation coefficient between LCP and RCP. The relation between attenuation coefficient α^{pol} with the absorption cross-section is:

$$\alpha^{\mathrm{pol}} = M \sigma_{\mathrm{abs}}^{\mathrm{pol}}, \tag{4.16}$$

where M is the molar density of the particle inside the solvent. The superscript pol denotes the corresponding polarization of the incident field while calculating the absorption of the ensemble.

Table 4.1 *Rotationally averaged expressions for different observable quantities after measuring the responses to either Left Circularly Polarized (LCP) or Right Circularly Polarized (RCP) light in term of the components of the helicity based T-matrix of the individual meta-atom.*

no	parameter	average value
1	Scattering cross-section (LCP)	$\frac{4\pi}{k_b^2}\mathrm{Tr}[\overline{T}^{\dagger}_{\mathrm{LL}}\overline{T}_{\mathrm{LL}} + \overline{T}^{\dagger}_{\mathrm{LR}}\overline{T}_{\mathrm{LR}}]$
2	Extinction cross-section (LCP)	$\frac{4\pi}{k_b^2}\,\mathrm{Re}\left(\mathrm{Tr}[\overline{T}_{\mathrm{LL}}]\right)$
3	Absorption cross-section (LCP)	$\frac{4\pi}{k_b^2}\,\mathrm{Re}\left(\mathrm{Tr}[\overline{T}_{\mathrm{LL}}(\overline{I} - \overline{T}^{\dagger}_{\mathrm{LL}}) - \overline{T}^{\dagger}_{\mathrm{LR}}\overline{T}_{\mathrm{LR}}]\right)$
4	Scattering cross-section (RCP)	$\frac{4\pi}{k_b^2}\mathrm{Tr}[\overline{T}^{\dagger}_{\mathrm{RR}}\overline{T}_{\mathrm{RR}} + \overline{T}^{\dagger}_{\mathrm{RL}}\overline{T}_{\mathrm{RL}}]$
5	Extinction cross-section (RCP)	$\frac{4\pi}{k_b^2}\,\mathrm{Re}\left(\mathrm{Tr}[\overline{T}_{\mathrm{RR}}]\right)$
6	Absorption cross-section (RCP)	$\frac{4\pi}{k_b^2}\,\mathrm{Re}\left(\mathrm{Tr}[\overline{T}_{\mathrm{RR}}(\overline{I} - \overline{T}^{\dagger}_{\mathrm{RR}}) - \overline{T}^{\dagger}_{\mathrm{RL}}\overline{T}_{\mathrm{RL}}]\right)$
7	Circular Dichroism	$\frac{4M\pi}{k_b^2}\,\mathrm{Re}\left(\mathrm{Tr}[\overline{T}_{\mathrm{LL}}(\overline{I} - \overline{T}^{\dagger}_{\mathrm{LL}}) - \overline{T}_{\mathrm{RR}}(\overline{I} - \overline{T}^{\dagger}_{\mathrm{RR}})\right)$

After we obtain the formula to extract the average polarization dependent response of our meta-atom, now it is the time to implement them. Figures 4.5 (a-c) show the rotationally averaged extinction, scattering and absorption cross-sections of the same helical structure described in the previous section for different polarizations. Both polarizations have almost the same responses. This is due to the fact that the extinction, scattering, and absorption cross-sections are measure of power, and they do not strongly depend on the polarization of the incident field.

This fact, however, does not mean that the observable parameters of different polarization is useless. From the tiny differences between LCP and RCP absorption cross-section, an important parameter emerging only in the context of circularly polarized light for the illumination can be extracted, which is the circular dichroism (CD). Using the direct parameter extraction from the T-matrix allows us to calculate this parameter in a very exact way beyond the dipole approximation. Figure 4.5 (d) shows the CD we obtain by using expansion order $N = 4$. The biggest CD signal can be seen to appear around 538 nm and several weaker peaks or dips around 645 nm, 510 nm, and 716 nm. The CD signal around 538 nm has the strongest signal and can be explained using the fact that the absorption resonance of the individual gold nanoparticle happens to be at 532 nm. Based on this, the coupling between gold nanoparticles will be strongest around this wavelength, and by extension, the general absorption response (including CD).

In this section, we have shown that extracting parameters from the T-matrix of its constituent meta-atom offers a fast and reliable way to compute several experimental responses of metamaterials made from self-assembly approach. These parameters depend on the polarization of the incident field. This allows us to discuss the polarization dependent responses purely in term of the T-matrix of its individual constituent without the need to do manual averaging procedure.

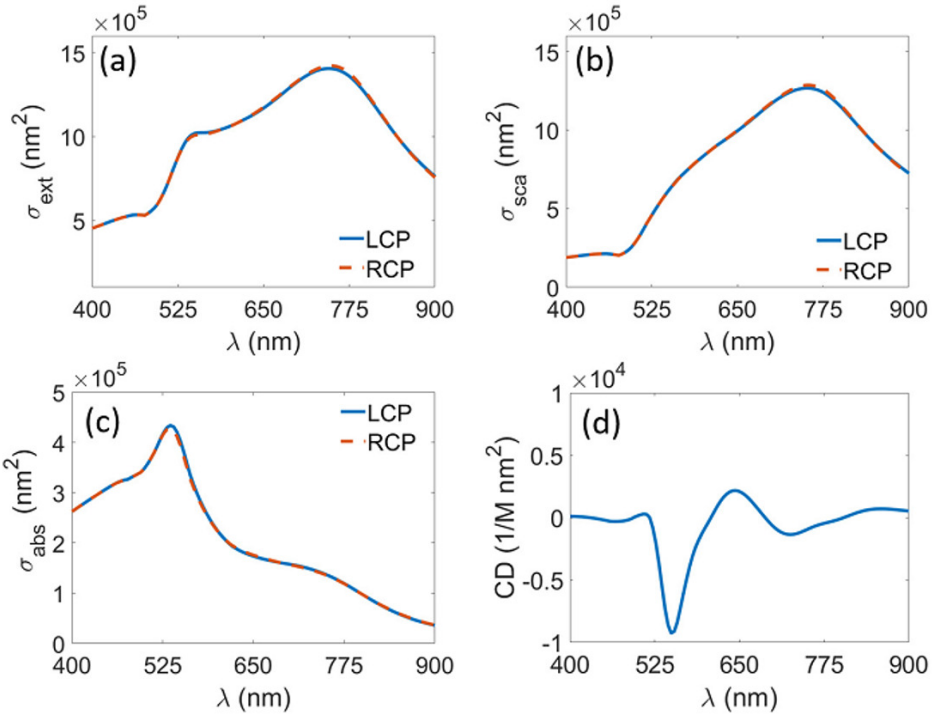

Figure 4.5 *Rotationally averaged (a) extinction, (b), scattering, and (c) extinction cross-sections of meta-atom described in Fig. 4.2.Different polarizations are denoted by different color. (d) Circular dichroism of the considered structure is obtained by the difference between absorption of left and right handed circularly polarized light. Adapted from P.4.*

4.2 Fano resonances in self-assembled metamaterials

In the previous section, we have shown how to extract several experimentally observables parameters of strongly diluted self-assembled metamaterials. Based on this development, in this section we will discuss Fano resonances and their signatures in metamaterials made from self-assembly methods.

Fano resonances are one of the most investigated phenomena in metamaterials research. This is mainly due to its sharp spectral features.[119–121]Their appearance is somewhat counterintuitive, particularly in the field of plasmonics, as the strong absorption prevents the observation of very sharp features. Fano resonances are often explained in terms of spectral interference between nonorthogonal modes sustained by the meta-atom. This requires the structure to supports multiple modes at a frequency range of interest. For a given incident field, at least two nonorthogonal modes have to be excited simultaneously. Frequently, one of the modes is assumed to be spectrally broad, and often called the bright mode. The other mode, on the hand, is spectrally relatively narrow compared to the previous mode, and often called the dark mode. The interaction between these nonorthogonal modes results in sharp spectral features in the optical response.[122,123]

For a structure made from several particles, it is quite challenging to identify the involved modes. This is because the properties of this structure cannot be explained in terms of modes supported by each of its constituent. Couplings between different constituents have to be taken into account. It is usually easier to analyze the modes involved as the collective modes of the ensemble rather than the individual modes of each constituent. These collective modes are often called supermodes.[124]

From the previous section, we have the ability to describe the optical response of self-assembled metamaterials directly from the T-matrix of its meta-atom. Additionally, in the previous chapter, modal analysis based on the T-matrix of a scatterer has been done. By combining these two ingredients, we have the necessary tools at hand to discuss Fano properties of metamaterials made from self-assembly methods, which will be the main content of this section. Due to the fact that the modes of the structure can be described in terms of eigenmodes or singular modes, as was discussed in the previous chapter, here we will present the analysis based on both approaches. For all cases presented in this section, an expansion order of N = 4 is used. This allows us to reach a convergence value with accuracy of more than 99 % for all parameters introduced in this section. In this section, we will focus our discussion onto the modes obtained from global coordinate T-matrix, which describes the collective modes of the meta-atom. However, this doesnt mean that the analysis presented here cannot be done with individual modes of the subsystems. We stress out that the choice of collective modes is done purely for the sake of simplicity and to ease our analysis, since less modes are needed compared to an analysis that relies on the individual mode picture.

4.2.1 Eigenvalue decomposition approach

First, let us start with EVD based approach, as described previously in section 3.1.1. By employing this spectral decomposition, the rotationally averaged scattering cross-section can be written as

$$\sigma_{\mathrm{sca}}^{\mathrm{aver}} = \frac{4\pi}{k_{\mathrm{b}}^2}\mathrm{Tr}[T^{\dagger}T] = \frac{4\pi}{k_{\mathrm{b}}^2}\mathrm{Tr}\left[\overline{X}^{-1\dagger}\ \overline{H}^{\dagger}\ \overline{X}^{\dagger}\ \overline{X}\ \overline{H}\ \overline{X}^{-1}\right]. \tag{4.17}$$

By applying the cyclic identity of matrix trace, $\mathrm{Tr}\left[\overline{A}\ \overline{B}\ \overline{C}\right] = \mathrm{Tr}\left[\overline{B}\ \overline{C}\ \overline{A}\right]$, the following equation can be deduced

$$\sigma_{\mathrm{sca}}^{\mathrm{aver}} == \frac{4\pi}{k_{\mathrm{b}}^2}\mathrm{Tr}\left[\overline{H}^{\dagger}\overline{X}^{\dagger}\overline{X}\ \overline{H}(\overline{X}^{\dagger}\overline{X})^{-1}\right]. \tag{4.18}$$

Whereas for the extinction cross-section, by applying Eq. 4.10, the following equation can be deduced:

$$\sigma_{\mathrm{ext}}^{\mathrm{aver}} = \frac{4\pi}{k_{\mathrm{b}}^2}\,\mathrm{Re}\left(\mathrm{Tr}[\overline{T}]\right) = \frac{4\pi}{k_{\mathrm{b}}^2}\,\mathrm{Re}\left(\mathrm{Tr}[\overline{E}]\right). \tag{4.19}$$

In summation form, these relations can be written as

$$\sigma_{\mathrm{sca}}^{\mathrm{aver}} = \frac{4\pi}{k_{\mathrm{b}}^2} \sum_{\mathrm{s}=1} \sum_{\mathrm{t}=1} \eta_{\mathrm{s}} \eta_{\mathrm{t}}^{*} \left\langle x_{\mathrm{s}} | x_{\mathrm{t}} \right\rangle \left\langle y_{\mathrm{t}} \middle| y_{\mathrm{s}} \right\rangle , \tag{4.20}$$

$$\sigma_{\mathrm{ext}}^{\mathrm{aver}} = \frac{4\pi}{k_{\mathrm{b}}^2} \mathrm{Re} \left(\sum_{\mathrm{i}=1} \eta_{\mathrm{i}} \right) . \tag{4.21}$$

From these equations, it can be inferred that the scattering cross-section of self-assembled metamaterials made from identical meta-atom contains direct terms, i.e, corresponding to an incoherent summation of contributions from the different modes, and cross terms, i.e, corresponding to the coherent summation between the modes. This fact can be easily understood if we rewrite the rotationally average scattering cross-section as

$$\sigma_{\mathrm{sca}}^{\mathrm{aver}} = \sigma_{\mathrm{sca}}^{\mathrm{dir,aver}} + \sigma_{\mathrm{sca}}^{\mathrm{cro,aver}}, \tag{4.22}$$

where

$$\sigma_{\mathrm{sca}}^{\mathrm{dir,aver}} = \sum_{\mathrm{s}=1}^{\mathrm{S}} |\eta_{\mathrm{s}}|^2, \tag{4.23}$$

denotes the incoherent summation of the contribution of independent eigenmodes of the meta-atom and

$$\sigma_{\mathrm{sca}}^{\mathrm{cro,aver}} = \frac{4\pi}{k_{\mathrm{b}}^2} \sum_{\mathrm{s}=1} \sum_{\mathrm{t}\neq\mathrm{s}} \eta_{\mathrm{s}} \eta_{\mathrm{t}}^{*} \left\langle x_{\mathrm{s}} | x_{\mathrm{t}} \right\rangle \left\langle y_{\mathrm{t}} \middle| y_{\mathrm{s}} \right\rangle , \tag{4.24}$$

denotes the contribution from the cross coupling between eigenmodes. It is the latter part which wil cause a Fano-type response. On the other hand, the extinction cross-section can be viewed as just the summation of modal strength from all modes. Therefore, it does not contain any cross coupling term.

To develop a framework where different scatterers can be compared directly, we introduce an average cross-coupling parameter C_{av}. This parameter describes how strong the cross-coupling terms are relative to the total scattering cross-section. It is defined as

$$C_{\mathrm{av}} = \frac{\sigma_{\mathrm{sca}}^{\mathrm{cro,aver}}}{\sigma_{\mathrm{sca}}^{\mathrm{aver}}}. \tag{4.25}$$

With this parameter, we are able to quantify how much mode cross coupling contributes to the total scattering cross-section of a given metamaterial made with a self-assembly method.

To demonstrate the applicability of the method, we choose a trimer structure described in the previous chapter as our example of the constituent meta-atom of the self-assembled metamaterial. The reason why we choose this structure is that the number of modes involved is rather small, which allows an easier analysis compared to a more complex structure. For the

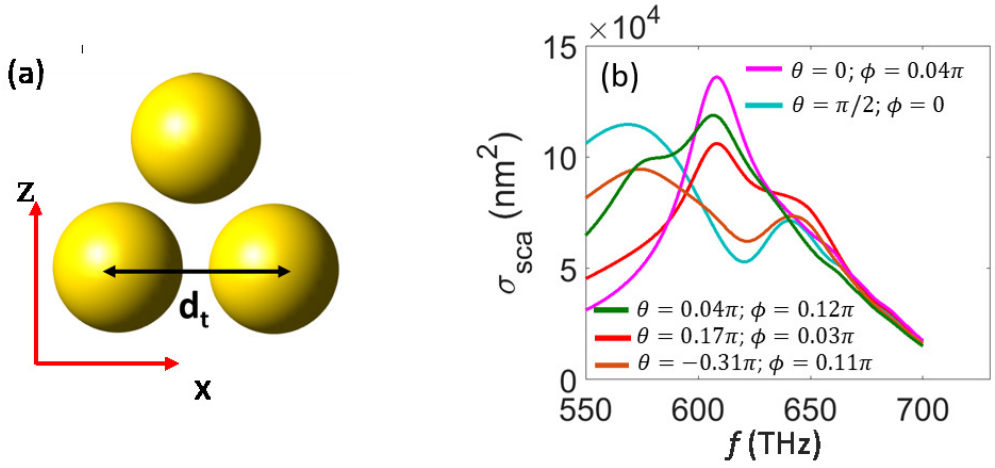

Figure 4.6 *(a) Sketch of the trimer stucture considered in this section. It is composed of three gold nanoparticles with a radius of 50 nm that are arranged equilaterally. Center to center distance between the nanoparticles, denoted as d_t is 120 nm. (b) Selected scattering cross-section resulted from different illumination scenarios, denoted by polar angle θ and azimuthal angle ϕ. The color denotes different incident field scenario, and correspond to the same color as in Fig. 4.1 Adapted from P.7.*

sake of clarity, we briefly describe the considered structure here again. Figure. 4.6 (a) shows the considered structure. Three identical gold nanoparticles are arranged at the corner of an equilateral triangle and the distance between each nanoparticle is 120 nm (center to center). The radius of the nanoparticles is 50 nm. Figure. 4.6 (b) shows the scattering cross-section of this structure for different illumination scenarios. The angle refers to incident field scenario in section 4.1.1. The different spectral behavior observed is the result of the interference between different modes, which are excited with different strength by the corresponding incident field. It has to be noted, however, that such spectral response can only be measured for a well-defined orientation between meta-atom and the incident field. In a solution which contains a large number of meta-atoms with random orientation, this well-defined spectral response cannot be observed and, therefore, one needs to resort to the averaging method to predict the observable response, as discussed in previous section of this chapter.

By applying Eq. 4.22, the rotationally averaged scattering cross-section of this trimer structure can be decomposed into direct and cross terms, as shown in Fig. 4.7 (a). The rotationally averaged scattering cross-section reaches its maximum, either a local or the global maximum, around 572, 602 and 645 THz. We also observe a notable dip around 592 and 628 THz. By looking into details of the behavior of $\sigma_{\text{sca}}^{\text{cro,aver}}$, we conclude that the dip at 592 THz only has the contribution from the incoherent summation between modes, as the cross-term value is negligible at this frequency. Therefore, the spectral feature is not due to a Fano resonance but rather the result of the incoherent contribution from different modes. In contrast, the other dip, which appears at 628 THz, occurs in a spectral region where the scattering cross-section has a notable contribution from the mode coupling in the structure. The value of $\sigma_{\text{sca}}^{\text{cro,aver}}$ reaches its maximum at this frequency, as can be seen in more detail in Fig. 4.7 (b). We observe that the

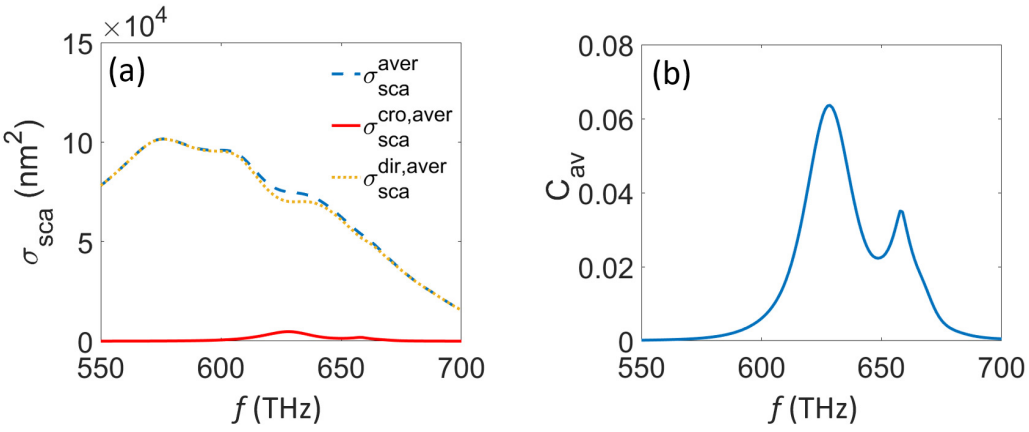

Figure 4.7 *(a) Rotationally averaged scattering cross-section and its decomposition into direct and cross terms. (b) mode coupling parameter C_{av} for the considered trimer structure as shown in Fig. 4.6(a). Adapted from P.7.*

cross-coupling parameter has two peaks, one around 628 THz, which match perfectly with the location of the spectral dip mentioned before, and a smaller one around 659 THz. The effect of the peak of C_{av} around 659 THz is quite small (around 0.04). As this frequency happens in the shoulder of the resonance of the rotationally averaged scattering cross-section, this effect is therefore quite negligible. Overall, it can be seen that now we are able to analyse the response of self-assembled metamaterials based on the coherent (cross terms) or incoherent (direct terms) contribution of the modes, which in turns enables us to discuss the emergence of Fano features in such system.

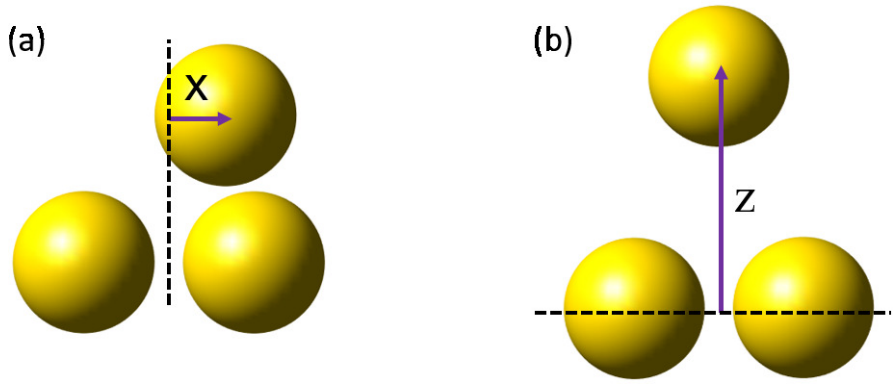

Figure 4.8 *(a) Geometry of the trimer when considering the impact of a symmetry breaking. We introduce the breaking of the symmetry by moving the upper sphere in (a) along the horizontal direction with the distance of x or in (b) along the vertical direction with the distance of z. Adapted from P.7.*

To enhance our understanding, here we also study the effect of a symmetry breaking of the structure. For metamaterials made from a top-down approach, it was reported that a more pronounced Fano effect can be observed by breaking the symmetry of the system.[122,125,126]

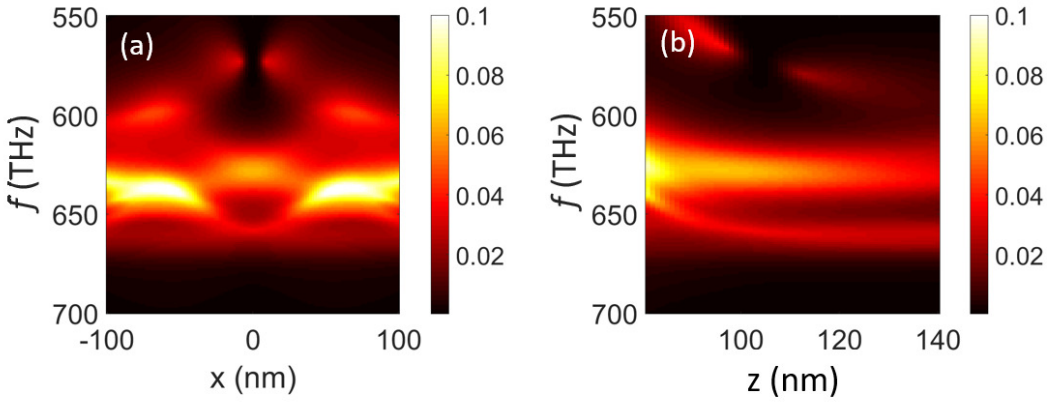

Figure 4.9 *(a) Cross-coupling parameter C_{av} when (a) moving the upper sphere in x direction and (b) moving the upper sphere in z direction, as described in Fig. 4.8. Adapted from P.7.*

Based on this fact, we will show that the same strategy can indeed enhance the Fano properties of the self-assembled metamaterials, which is associated with the mode cross coupling in its constituent meta-atom. The breaking of symmetry will be introduced by shifting the upper sphere in x or z direction, as shown in Fig. 4.8. We choose these ways of breaking the symmetry for two reasons. By moving the sphere in z direction, we preserve the mirror symmetry while rotationally symmetry is broken. On the other hand, moving the particle in x direction will break both the mirror and the rotational symmetry of the structure.

Figure 4.9 (a) shows the mode cross coupling parameter, C_{av}, for several displacements of the upper sphere in x direction, as was sketched in Fig. 4.8 (a). From this figure, in the case of the highest symmetry (x=0 nm), a very small C_{av} around 570 THz can be observed. On the other hand, C_{av} has a maximum value around 630 THz for a displacement of x=60 nm. This value can be attributed to strong coupling in this configuration, since in this case, one of the spheres has the shortest distance possible with respect to the other sphere. At this distance, the upper sphere is directly above another sphere, and the coupling between them is therefore at its maximum. This can also be analysed directly using the eigenmodes of the subsystem. For the case of a single sphere, only an electric dipole mode is supported, and the upper single sphere can be considered as a bright mode. On the other hand, the two dipole moments for the other two spheres will form either magnetic dipole or electric quadrupole mode, as discussed in section 3.1.2. Based on this fact, we can claim that the bottom spheres are going to support collectively a dark mode. For a minimum distance, the coupling between these two modes (bright and dark) increases, which therefore results in the increase of mode coupling.

The cross coupling parameter, C_{av} can also be affected by moving the particle in z direction, as shown in Fig. 4.9 (b). A stronger C_{av} can also be seen when the upper particle moves closer to the other two particles. This behavior is very similar to the behavior observed in Fig. 4.9 (a). Based on these two facts, it can be concluded that a stronger mode coupling occurs when the particles are very close to each other.

The previously mentioned analysis is based on the individual modes of the subsystem. Since the modes obtained from the global coordinate T-matrix as used in this section describe the collective modes of the scatterer, here we will present the underlying aspects of the increases of C_{av} due to the breaking of symmetry, as was shown in Fig. 4.9 (a). For this purpose, the modal strength of the 11 most dominant eigenmodes, denoted by their large modal strength compared to the other eigenmodes (> 50 times) are plotted in Fig. 4.10. The modal strength of the other eigenmodes are not shown here for the sake of clarity. The multipolar components of each eigenmode can be extracted directly from the corresponding eigenvector of the T-matrix. Figure 4.10 (a) shows its corresponding multipole moment components for the case of the perfect trimer structure at the frequency of 637 THz, as mentioned in the figure caption. Due to the symmetry, some of the modes are degenerate, as shown in the legend. The degeneracy can be attributed to the symmetry of the system. Due to the fact that several modes share the same multipolar moments, mode coupling between these modes might exist. The possible couplings are the coupling between blue mode (mode 1 and 2) and black mode (mode 7 and 8) and the coupling between red mode (mode 5 and 6) and green mode (mode 10 and 11). This is because they share the same multipole moments, which resulted in the nonorthogonality between these modes. By moving the upper particle in x direction, the symmetry of the system is broken, and these degenerate modes are no longer degenerate, as shown in Fig. 4.10 (b). We can observe that more modes are sharing the same multipolar components, which ultimately results in the increase of C_{av}, as was observed in Fig. 4.9 (a).

Further analysis of the origin of the behavior of C_{av} can be done by taking the mode nonorthogonality of selected modes. We define the mode nonorthogonality as

$$D_{\mathrm{ij}} = \frac{|\langle x_{\mathrm{i}}|x_{\mathrm{j}}\rangle|^2}{\langle x_{\mathrm{i}}|x_{\mathrm{i}}\rangle\langle x_{\mathrm{j}}|x_{\mathrm{j}}\rangle}. \tag{4.26}$$

The subscript denotes the index of the modes as shown in Fig. 4.10. First, let us concentrate on the mode coupling in the case of the perfect trimer structure. Modes nonorthogonality between selected pairs of modes is shown in Fig. 4.11. To simplify our discussion, in the case of the degenerate modes of the symmetric structure (modes 1,2 and 7,8 and modes 5,6 and 10,11), the mode nonorthogonality is defined as the sum of the mode nonorthogonality between all the modes, or mathematically speaking, $D_{\mathrm{Deg}} = (D_{17} + D_{27} + D_{18} + D_{28})$ and $D_{\mathrm{Deg2}} = (D_{5,10} + D_{6,10} + D_{5,11} + D_{6,11})$. From this plot, it is clear that the small peak at the frequency around 630 THz for the case of x=0 nm as was shown in Fig. 4.9 (b) as well as in the inset is due to the coupling between mode 1 and 2 and mode 7 and 8. On the other hand, the peak of C_{av} around 670 THz is due to the coupling between mode 5 and 6 and mode 10 and 11. The cross-coupling terms described in Eq. 4.24 contains the eigenvalue terms, which is the reason that the amplitudes of mode nonorthogonality presented in Fig. 4.11 are not the same as the amplitude of its corresponding C_{av}. Nevertheless, the origin of C_{av} peaks can be traced back to the nonorthogonality between these specific modes involved.

By employing the same analysis, the mode nonorthogonality for the case of x=60 nm can also be obtained, which is shown in Fig. 4.12. Here, the same convention as in Fig. 4.10 has been

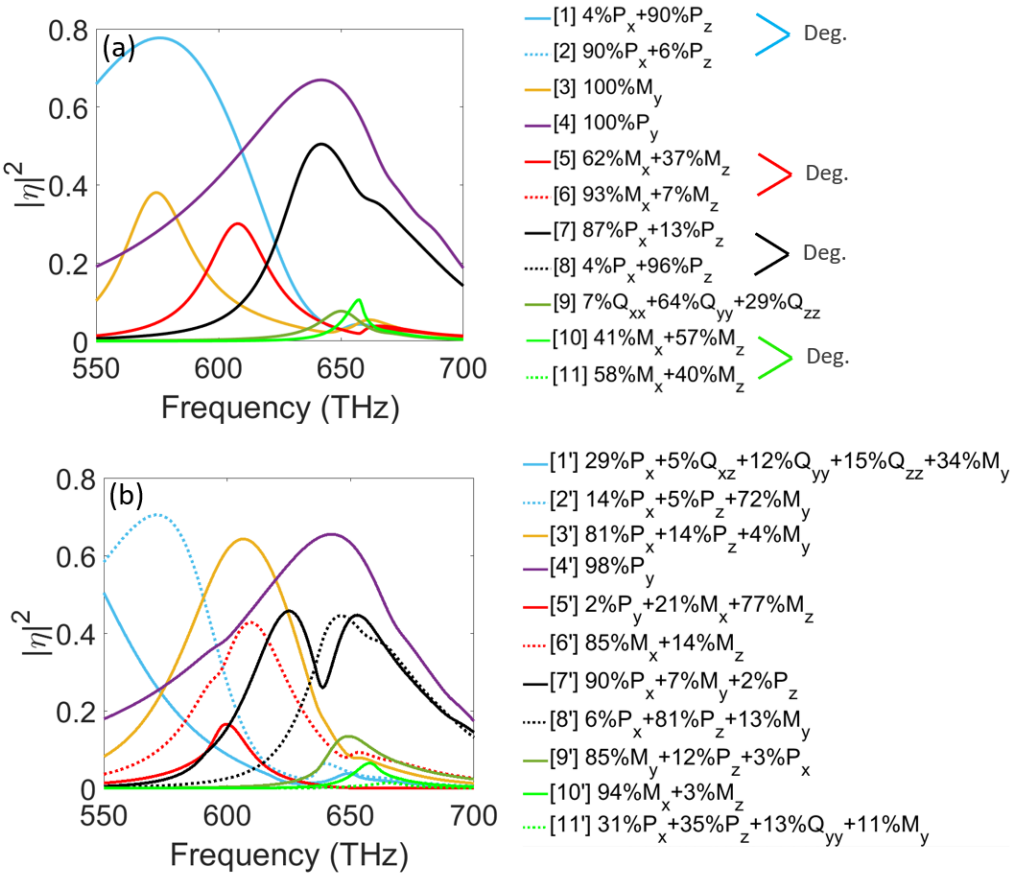

Figure 4.10 *Modal strength of 11 dominant eigenmodes of (a) perfect trimer structure and (b) asymetric trimer when x=60 nm. P, M,and Q denoted electric dipole, magnetic dipole, and electric quadrupole moments, while the subscript denotes its component. All multipolar decompositions presented here are analyzed at a frequency of 637 THz. For the case of mode 10, 10', 11, and 11', we multiply their modal strength by a factor of 10 for visibility. Adapted from P.7.*

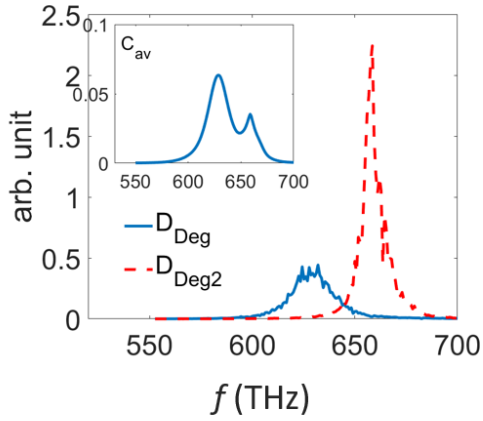

Figure 4.11 *Absolute value of the mode nonorthogonality between selected pairs of modes as described in Fig. 4.10 (a), which is the case for a perfect trimer structure. We define the mode nonorthogonality according to Eq. 4.26, while the subscript denotes the pair of modes, which is defined as* $D_{\mathrm{Deg}} = D_{17} + D_{27} + D_{18} + D_{28}$ *and* $D_{\mathrm{Deg2}} = D_{5,10} + D_{5,11} + D_{6,10} + D_{6,11}$. *The subscript denotes the pair of modes discussed in Fig. 4.10 (a). Adapted from P.7.*

used. Based on the value of C_{av} and mode nonorthogonality, it can be deduced that the C_{av} peak around 600 THz is mainly due to the coupling between modes 1' and 3' and also 1' and 7', while the dominant peak around 640 THz is the result of the coupling between these three modes.

Another interesting aspect is the appearance of a small peak around frequency of 570 THz when the upper sphere is shifted in x direction. A noticeable peak appears when the x value increases and reaches its maximum around x=8 nm before it starts decreasing. To understand this effect, Fig. 4.13 shows the modal strengths of 3 modes which evolve from the modes indicated by 1,2 and 3 in Fig. 4.10 (a), respectively. If the resonance frequencies of mode 1 (and 2) and 7 are close to each other, a stronger coupling is observed. This strong coupling will finally flip both modes, resulted in mode 3' has a general characteristic of mode 1 and 2 at a frequency of 637 THz, and *vice versa*. Note that, however, since the breaking of the symmetry in general will not preserve the mode characteristics, some of the initial characteristics (x=0 nm) will be altered, These are the reason why mode 3' has P_{x} component at frequency of 637 THz, which can be traced back to mode 2. This mode crossing is the main reason for the small peak of C_{av} around the frequency of 570 THz as described in Fig. 4.9 (a).

In this section, we have shown a method to analyze Fano properties of metamaterials fabricated using self-assembly approach using eigenmodes of the meta-atom. Fano properties, which are the results of coupling between different nonorthogonal modes, can be investigated from the modes of the individual meta-atom constituent in a very diluted limit. The Fano signature is only observed in the rotationally averaged scattering cross-section, while no signature can be expected in the rotationally averaged extinction cross-section. The mode coupling contribution can be described by a figure of merit parameter, C_{av}. By breaking the symmetry of the meta-

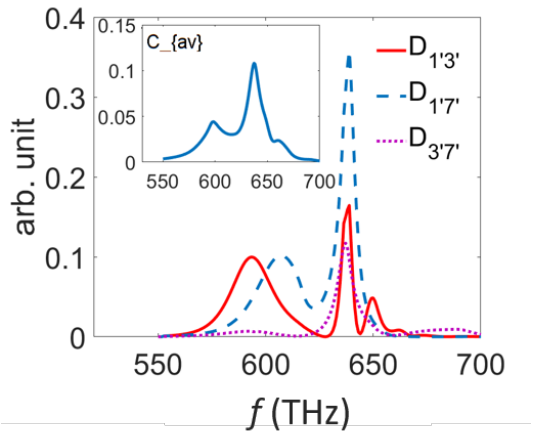

Figure 4.12 *Absolute value of the mode nonorthogonality between selected pairs of modes described in Fig. 4.10 (b). We define the mode nonorthogonality according to Eq. 4.26, while the subscript denotes the pair of modes discussed in Fig. 4.10 (b). Adapted from P.7.*

atom, we have shown that a stronger C_{av} can be obtained. This will pave a way to design an isotropic metamaterial with Fano properties.

4.2.2 Singularvalue decomposition approach

In the previous section, we discussed Fano resonances in terms of the mode coupling of the eigenmodes of the system. This is possible due to the fact that the EVD of a nonhermitian system will not always produce an orthogonal basis set. In this section, we will discuss the mode coupling in terms of another spectral decomposition, the SVD, as described in section 3.2. When analysing the singular modes, $\sigma_{\mathrm{sca}}^{\mathrm{aver}}$ and $\sigma_{\mathrm{ext}}^{\mathrm{aver}}$ can be expanded as

$$\sigma_{\mathrm{sca}}^{\mathrm{aver}} = \frac{4\pi}{k_{\mathrm{b}}^2}\mathrm{Tr}\left[\overline{T}^{\dagger}\overline{T}\right] = \frac{4\pi}{k_{\mathrm{b}}^2}\mathrm{Tr}[|\overline{\Sigma}|^2], \tag{4.27}$$

$$\sigma_{\mathrm{ext}}^{\mathrm{aver}} = \frac{4\pi}{k_{\mathrm{b}}^2}\,\mathrm{Re}\left(\mathrm{Tr}[\overline{T}]\right) = \frac{4\pi}{k_{\mathrm{b}}^2}\,\mathrm{Re}\left(\mathrm{Tr}[\overline{\Sigma}\ \overline{V}^{\dagger}\ \overline{U}]\right). \tag{4.28}$$

Or, in summation form

$$\sigma_{\mathrm{sca}}^{\mathrm{aver}} = \frac{4\pi}{k_{\mathrm{b}}^2}\sum_{\mathrm{j}}|\sigma_{\mathrm{j}}|^2, \tag{4.29}$$

$$\sigma_{\mathrm{ext}}^{\mathrm{aver}} = \frac{4\pi}{k_{\mathrm{b}}^2}\,\mathrm{Re}\left(\sum_{\mathrm{j}}\sigma_{\mathrm{j}}\left\langle v_{\mathrm{j}}\middle|u_{\mathrm{j}}\right\rangle\right). \tag{4.30}$$

The above equations tell us, in term of singular modes, that the average scattering cross-

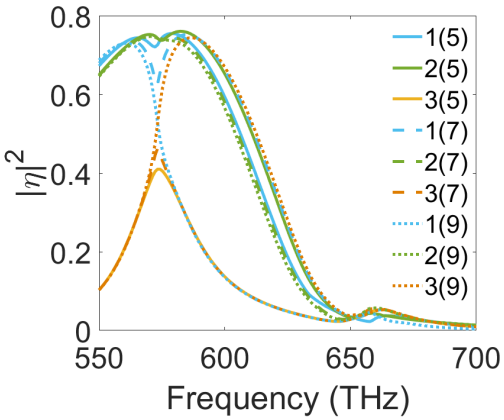

Figure 4.13 *Selected modal strength of the trimer structure for various horizontal displacement in x direction. The mode index corresponds to the index in Fig. 4.10, while the value in bracket denotes the displacement (in nm) with respect to the perfect trimer structure*

section is just the sum of the modal strength of the singular modes (singular values of the T-matrix). However, for the extinction cross-section, it is the sum of the overlap between singular modes v_i and u_i multiplied by the respective modal strength. Note that, however, from the discussion in chapter 3, Fano resonance can be basically understood as an inherent property of the singular modes. This means that in some cases, a single singular mode can exhibit Fano properties. We elaborate that in the following.

Recall that the singular vectors of a matrix are unitary matrices. This means that

$$\overline{V}\ \overline{V}^{-1} = \overline{V}\ \overline{V}^{\dagger} = \overline{I}. \tag{4.31}$$

Now, by considering eigenvalue and singular value decomposition simultaneously, the T-matrix can be expressed as

$$\overline{T} = \overline{X}\ \overline{E}\ \overline{X}^{-1} = \overline{U}\ \overline{\Sigma}\ \overline{V}^{\dagger}, \tag{4.32}$$

which can be rewritten as

$$\overline{X}\ |\overline{E}|\ \overline{\psi}\ \overline{X}^{-1} = \overline{U}\ \overline{\Sigma}\ \overline{V}^{\dagger}, \tag{4.33}$$

where $\overline{\psi}$ is a diagonal matrix and its components contain the information about the phase of the eigenvalues. In the special case of orthogonal eigenmodes as a basis set, the absolute value of both eigenvalues and singular values will be the same, $\overline{\Sigma} = |\overline{E}|$. This means that

$$\overline{X} = \overline{U}. \tag{4.34}$$

By using the unitary identity of singular modes, $\overline{V}^{\dagger}\ \overline{V} = \overline{V}\ \overline{V}^{\dagger} = \overline{I}$, the following equation can be obtained.

$$\overline{X}\ \overline{\psi}^{\dagger} = \overline{V}. \tag{4.35}$$

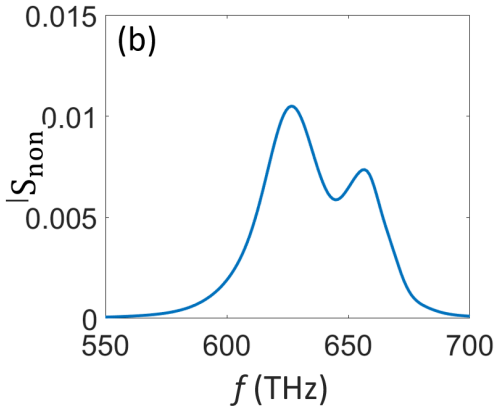

Figure 4.14 *Modes nonorthogonality parameter, S_{non}, for trimer structure described in Fig. 4.6 (a).*

Now, it is quite clear that, by comparing the singular vectors $\overline{V}$ and $\overline{U}$, the information about the nonorthogonality of the eigenmodes can be obtained.

As with the previous section, to enablea comparison of the modes nonorthogonality between different configurations, we introduce the mode nonorthogonality parameter, S_{non}, which is defined using the Frobenius distance between two matrices $\overline{A}$ and $\overline{B}$,[127,128]

$$S_{\text{non}} = \frac{(\text{Tr}[\overline{A} - \overline{B})(\overline{A} - \overline{B})^{\dagger}]}{2\text{Tr}[\overline{A}\ \overline{A}^{\dagger}] + \text{Tr}[\overline{B}\ \overline{B}^{\dagger}]}, \tag{4.36}$$

where

$$\overline{A} = \overline{U}\ \overline{\Sigma}\ \overline{U}^{\dagger}, \tag{4.37}$$

$$\overline{B} = \overline{V}\ \overline{\Sigma}\ \overline{V}^{\dagger}. \tag{4.38}$$

In Eq. 4.36, we normalize the Frobenius distance with the sum of the norm of matrices $\overline{A}$ and $\overline{B}$ such that our S_{non} has a value between 0 and 1. Note that in Eqs. 4.37 and 4.38, no phase in the complex plane is involved, since we define these parameters to describe the absolute value of our modes. This means that, compared to C_{av} introduced in the previous section, the physical meaning of S_{non} parameter is the following: it describes how easy mode coupling can occur for a certain structure, irrespective of the incident field. This is in contrast with C_{av}, which tells us the rotationally averaged Fano signal in the scattering cross-section.

As our study case, here we consider again the trimer structure considered in the previous section. First, we start with the perfect trimer structure, as described in Fig. 4.6 (a). The corresponding S_{non} is presented in Fig. 4.14. We observe two peaks in the spectral range of interest. The dominant peak happens around 620 THz, while a less pronounced peak can be observed around 660 THz. If we compare the spectral position of these two peaks with the peaks of C_{av} shown in Fig. 4.7 (b), we observe a very good agreement of peak positions between S_{non} and C_{av}. The dominant peak of C_{av} also translates to a dominant peak in S_{non} and the

spectral position of the less pronounced peak also matches perfectly.

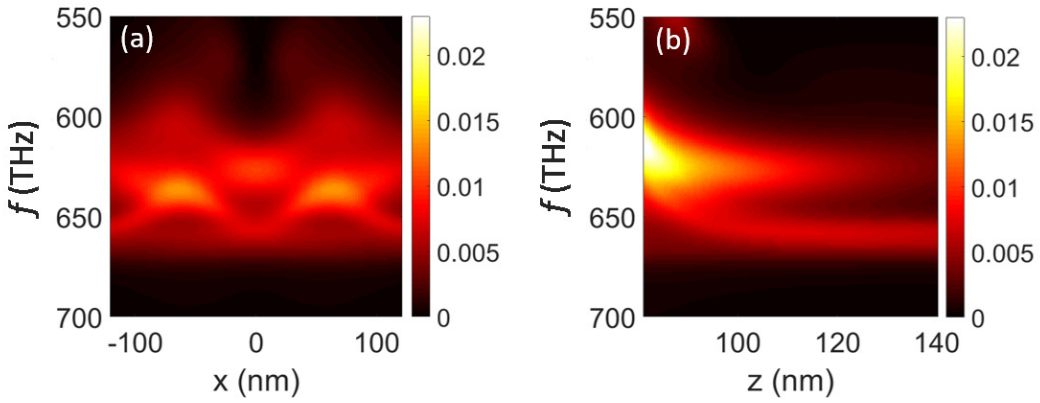

Figure 4.15 *modes nonorthogonality parameter, S_{non} for assymetric trimer structure described in Fig. 4.8, where the upper particle is moving in (a) horizontal x direction and (b) vertical z direction*

After we are done with a perfect trimer structure, as studied in the previous section, here we will also consider the case of a symmetry breaking, as described in Fig. 4.8. The corresponding S_{non} are presented in Fig. 4.15. Here, the same trends can be observed. In Fig. 4.15 (a), we show the contour map of S_{non} where the upper particle is displaced in x direction, as described in Fig. 4.8 (a). Here, as in the case of perfect trimer, a strong S_{non} around 640 THz can be observed, while breaking the symmetry resulted in a stronger peak of S_{non} around 645 THz for the case of x=60 nm. This behavior matches perfectly with the behavior observed for C_{av}, as shown in Fig. 4.9 (a).

By shifting the particle in z direction, as described in Fig. 4.8 (b), a stronger S_{non} can also be observed. This is shown in Fig. 4.15 (b). For the case of a large z, two peaks can be observed. A stronger S_{non} is also observed when the upper particle is shifted closer to the other two particles. These behaviors match with the behaviors of its related C_{av}, as shown in Fig. 4.9 (a). Based on these, we can conclude that both measures, C_{av} and S_{non}, can be used to describe the Fano resonances in metamaterials. They differ only in the respective spectral decomposition used for their calculation.

In this section, we have introduced another parameter, S_{non}, to describe Fano features in self-assembled metamaterials. This new parameter is obtained from the singular modes. Contrary to the C_{av} introduced in the previous section, S_{non} describes how easy mode couplings can occur for a certain structure, irrespective of the incident field.

4.3 Summary

In this chapter, the observable quantities of metamaterials fabricated using self-assembly technique were discussed. As opposed to conventional metamaterials, here the observables are often described by using rotationally averaged quantities extracted from the meta-atom in a very

diluted limit. In this chapter, we have shown that, by knowing the T-matrix of the constituting meta-atom, the observable quantities can be predicted directly without the need to do manual averaging procedure. Using this fact and the modal analysis presented in section 3.1.1, the decomposition of observable quantities of self-assembled metamaterials in terms of modes was done. We introduced a mode cross-coupling parameter C_{av}, which quantifies how much mode cross coupling terms contributed to the total rotationally averaged scattering cross-section. This parameter allows us to discuss different Fano features, which arises from coupling between non-orthogonal modes. This is followed by the discussion of singular modes in self-assembled metamaterials. Another parameter, which describes how much mode coupling terms can occur for a certain structure, which we call modes nonorthogonality parameter S_{non}, was introduced. These two parameters allow the discussion of the response of self-assembled metamaterials in terms of modes of the meta-atom.

Chapter 5
5 Optical Sensing Devices

In the previous chapter, we have shown the application of the T-matrix method to describe the optical response from metamaterials fabricated using self-assembly approach. In this chapter, we will shift now our attention to a specific application in an optical sensing device. In the first section, we will introduce some basic terms which are related to optical sensing devices in general. This allows us to understand the terminology and physical meaning behind it. Following this, we will discuss optical sensors that rely on either dielectric or metallic resonators. We will show the advantages and disadvantages of these two distinct sensors.

By combining the advantages of the dielectric and metallic based sensors, a hybrid sensor can be designed. This will be the focus of the discussion in the second section of this chapter. To be specific, we will discuss the combination of a plasmonic sensor and a sensor based on whispering gallery modes. The content of this chapter is mostly based on P.3.

5.1 Basics of an optical sensing device

In this section, we will review some basic terminology used in optical sensing devices.We will start by the discussion of Lorentzian response, which arises as the natural response of an optical resonator. Following this, Free Spectral Range, which is defined as the distance between two neighboring resonance frequencies and its impact to the readability of a resonator will be presented. This will be followed by the discussion on reactive sensing principle, which will be used extensively to analyze the behavior of an optical sensor.

In the second part of this section, a sensor based on a dielectric structure is presented. Here, whispering gallery modes, which arise naturally as the solution of a closed resonator, will be the main focus. We will discuss the advantage and disadvantage of this sensor based on the foundations laid down before. Finally, the last part will be dedicated to the discussion of metal based optical resonator, in the form of a sensor based on localized surface plasmon polaritons. As with its dielectric structure counterpart, we will also discuss the advantage and disadvantage of sensors based on localized surface plasmons.

5.1.1 Theoretical foundation of optical sensing device

The optical response,($R(\omega)$), of an optical resonator,, can be derived from the scattered or transmitted field outside of such a resonator. Usually, the amplitude of the scattered or transmitted

field can be described by a Lorentzian function with its linewidth Γ and resonance position ω_0. It can be written as:

$$R(\omega) = \left| A \frac{1}{\omega - \omega_0 + i\Gamma} \right|^2 . \tag{5.1}$$

In the above equation, A is the respective amplitude of the response of an optical resonator. Physically, the Lorentzian shape of the response of an optical resonator in the frequency domain is a direct consequence of the fact that the amplitude of the response of an optical resonator in the time domain decays over time. The Fourier transformation of an exponential decay function is a Lorentzian function.[129] This is the reason why the response of an optical resonator can be described as a Lorentzian function (or a sum of several Lorentzian functions in the case of multiple modes) in the frequency domain.

The quality factor (Q-factor), which is defined as $\frac{\omega_0}{2\Gamma}$, is usually used to characterize a resonator and it represents the energy loss-rate relative to the total energy stored inside the resonator. The energy loss can be attributed to several loss channels, such as radiation, bulk scattering, surface scattering, and material absorption.[60] All of these factors contribute to the total linewidth, and by extension, the Q-factor of the corresponding resonator. Based on this fact, Γ and Q-factor (Q) of a resonator can be decomposed as:

$$\Gamma = \Gamma_{\text{sca}} + \Gamma_{\text{abs}} + \cdots , \tag{5.2}$$

$$Q^{-1} = Q_{\text{sca}}^{-1} + Q_{\text{abs}}^{-1} + \cdots , \tag{5.3}$$

where the subscripts sca and abs denote the contribution from scattering and material absorption, respectively. Since most of the resonators support multiple modes, another parameter is important that defines the readability of optical response of the resonator, the Free Spectral Range (FSR). This parameter is defined as the spectral distance between the two nearest resonance positions, either in wavelength or in frequency domain.[130,131] The combination of linewidth and FSR is very important for the readability of the optical response of a resonator, as can be seen in Fig. 5.1 (a). Here, we consider only four resonances, but the analysis presented here can also be applied for higher number of resonances. In this figure, the response, which is the sum of several Lorentzian functions with the same linewidth but for different resonance frequencies, is shown. The resonance frequencies are separated by the FSR. We normalized the frequency with respect to the FSR. For the total signal, we plot the sum for different FSR/Γ ratios. We see that either by decreasing the FSR or increasing Γ, the resonance position of each Lorentzian becomes harder to distinguish relative to that of others. To be able to track the resonance frequency of each resonance, the response at the corresponding resonance freqeuency must be larger than the value of the response at other non resonant frequency. To be able to quantify this, we define a Figure of Merit (FOM), defined as the difference of the value of the response at the resonance (at a normalized resonance frequency of 35 in our case) and the middle frequency to its nearest resonance neighbor (at a normalized frequency of 35.5), and then normalized with the value of the response at the resonance. Two resonance frequencies can be distinguished if the value of the FOM is larger than 0, which in this case is valid if the ratio

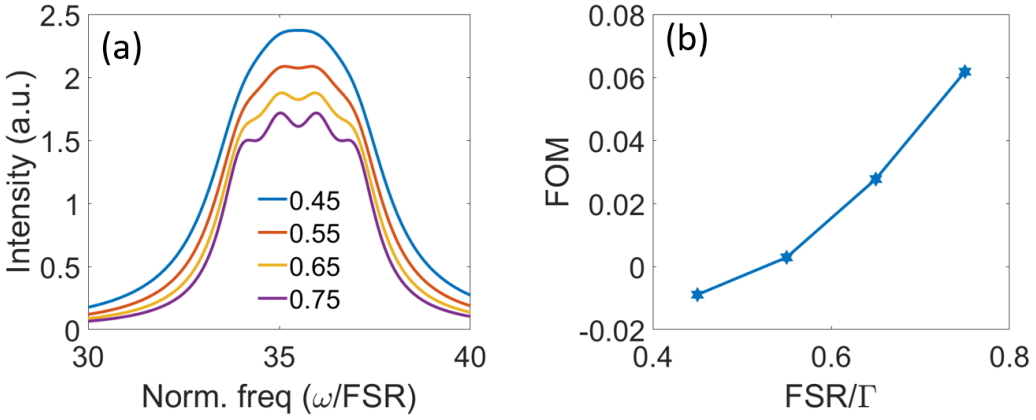

Figure 5.1 *Sum of 4 Lorentzians with normalized resonance frequency of 34, 35, 36 and 37 and an identical linewidth* Γ*. Two neighboring resonance frequencies are separated by the Free Spectral Range (FSR). Different ratio of FSR/*Γ *are plotted here with different color.(b) Figure of Merit (FOM), defined as the difference between the value of intensity at a normalized resonance frequency of 35 and the value of intensity at a normalized frequency of 35.5 divided by the intensity at a normalized resonance frequency of 35. Two resonance frequencies can be distinguished if the value of FOM is larger than 0, which in this case is valid for the case of the ratio of FSR/*Γ *smaller than 0.55.*

of FSR/Γ is smaller than 0.55. We can conclude that the resonances can be well distinguished when the value of FSR/Γ is above a certain threshold, which is 0.55.

After clarifying the terminology needed, in the following we will focus on the working principle of a resonator as an optical sensor. Basically, the resonator works as an optical sensor if we measure the shift/change of the resonance position of the optical response when the resonator is exposed to a modified environment. The changes in the surrounding environment can vary greatly, ranging from the addition of another particle/molecule up to a homogeneous change of the background environment. The details eventually do not matter as long as we assume that the modified optical environment can be simply represented as a modification of the dielectric properties of the ambient medium. For all of these possible cases, the resonance shift can be approximated by using perturbation theory (in the first order appproximation) as[132]

$$\frac{\delta\omega}{\omega_0} \approx \frac{\int_{V_\mathrm{p}} [\varepsilon_\mathrm{p}(\mathbf{r}) - \varepsilon_\mathrm{h}(\mathbf{r}))] |\mathbf{E}(\mathbf{r},\omega_0)|^2 d\mathbf{r}}{2\int_{V_\mathrm{all}} \varepsilon(\mathbf{r}) |\mathbf{E}(\mathbf{r},\omega_0)|^2 dV}. \tag{5.4}$$

Here, $\mathbf{E}(\mathbf{r},\omega_0)$ is the electric field of the mode sustained by the resonator, $\delta\omega$ denotes the resonance shift, ω_0 is the initial resonance frequency, $\varepsilon_\mathrm{p}(\mathbf{r})$ is the permittivity distribution of the system in the presence of the modified environment, $\varepsilon_\mathrm{h}(\mathbf{r})$ is the permittivity of the initial surrounding medium, and $\varepsilon(\mathbf{r})$ denotes the initial permittivity distribution across the entire spatial domain. The integration area V_p (V_all) denotes the area outside the resonator (across the entire space). Equation 5.4 tells us that if the background permittivity increases, it will induce

a redshift in the resonance, and *vice versa*. Equation 5.4 is also known as the reactive sensing principle. Equation 5.4 tells us that in order to have a stronger resonance shift, the evanescent electric field outside the resonator must be large, or the electric field decays weakly outside the resonator. If we consider the evanescent field as the only possible loss channel, this means that a broader linewidth of the optical response of the resonator can be expected. This means that there is always a trade-off between the sensitivity and the readability of an optical sensor. Note that, however, the conclusion we draw here is only valid in the first order approximation. By including the second order expansion, it is possible to obtain different conclusions.[133] However, this will not be the scope of this thesis, as the first order approximation is usually enough to explain the results presented here. If the additional inclusion in the surrounding medium consists of a very small molecule, a quasi-static approximation is valid. This means that Eq. 5.4 can also be approximated as:[134]

$$\frac{\delta\omega}{\omega_0} \approx \frac{\mathrm{Re}[\alpha]|\mathbf{E}(\mathbf{r}_\mathrm{p},\omega_0)|^2 d\mathbf{r}}{2\int_{V_\mathrm{all}} \varepsilon(\mathbf{r})|\mathbf{E}(\mathbf{r},\omega_0)|^2 dV}, \tag{5.5}$$

where α denotes the polarizability of the molecule and $\mathbf{r}_\mathrm{p}$ is the position of the molecule. This equation is often used for a biological particles, such as proteins or viruses.

In the case of a homogeneous change of the surrounding medium, the sensitivity of an optical sensor is usually written in terms of Bulk Refractive Index Sensitivity (BRIS), defined as

$$\mathrm{BRIS} = \frac{d\lambda_\mathrm{res}}{dn_\mathrm{b}} = -c\frac{2\pi}{\omega_0^2}\frac{d\omega_\mathrm{res}}{dn_\mathrm{b}} \tag{5.6}$$

where λ_res is the resonance wavelength of the resonator and n_b is the background refractive index. In the case of a single molecule sensing scenario, the resonance shift per each particle is usually enough to quantify the sensitivity of the device.

Another important parameter is the shot noise limit, which describes the minimum possible resonance shift of an optical sensing device, $\delta\omega_\mathrm{sh}$. It corresponds to the lower bound of the resolution of the signal that can be captured by a photodetector from the optical response of an optical sensor. This is due to the fact that in experiments, the optical response usually converted to an electrical signal. Due to the random fluctuations of the electric current in the photodetector, it is impossible to convert precisely the optical signal to an electrical signal without any error. Therefore, a parameter to describe the upper bound of the error, which corresponds to the minimum possible resonance shift, is needed. This parameter is given by:[135]

$$\frac{\delta\omega_\mathrm{sh}}{\omega_\mathrm{res}} = \frac{1}{Q}\sqrt{\frac{\hbar\omega_\mathrm{res}}{P_0\eta\beta\tau}}. \tag{5.7}$$

Here, P_0 is the optical power, η denotes the photodetector quantum efficiency, while β and τ denote transmission efficiency of the resonator and averaging time, respectively. It can be seen from this relation that a higher Q-factor corresponds to a smaller possible resonance shift that

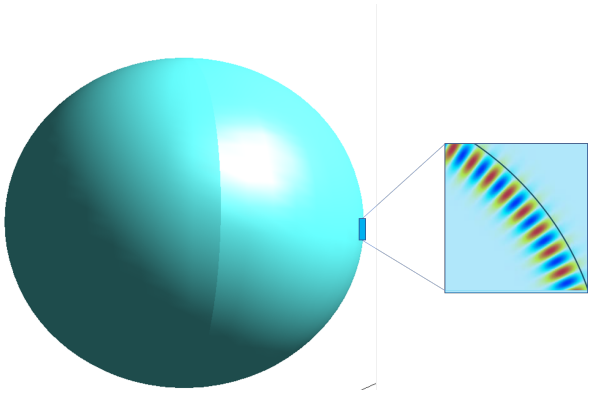

Figure 5.2 *Illustration of WGM supported in a sphere. The sphere has a radius of 5 μm and is made from silica with a permittivity of 2.25. The sphere is embedded in vacuum. Here, most of the field confined inside the resonator, resulted in a very high Q-factor.*

can be detected, therefore very high resolution can be obtained by using a resonator with high Q-factor. However, as mentioned before, a higher Q-factor means less sensitivity. This means that a higher resolution is always accompanied by a lower sensitivity of the resonator. Based on this, we arrive at one important conlusion: there is always a trade-off between the sensitivity and the resolution for an optical sensing device.

In this section, we have shown the basic terminology and the working principle of an optical sensing device. The response of an optical sensing device is usually characterized by a Lorentzian line shape. For the case of a resonator that supports multiple modes, the combination of Free Spectral Range and quality factor play an important role for the readability of the sensor. We also discussed the reactive sensing principle, which tells us that better sensitivity can be achieved by enlarging the field overlap at the background medium. Finally, the shot-noise limit was introduced to define the resolution of an optical sensor.

5.1.2 Sensor based on the whispering gallery mode resonator

Sensing based on a dielectric resonator, often called whispering gallery mode resonator, is one subclass for an optical sensing device. For a dielectric resonator, most of the field is confined inside the resonator, as illustrated in Fig. 5.2. For a large dielectric resonator, usually with dimensions that can be up to 1000 times the resonance wavelength, a very high Q-factor (above 10^7) can be achieved. This means that, based on Eq. 5.7, the resolution of this device can be quite high, as the minimum resonance shift that can be detected is very small. At the same time, the small sensitivity can be understood from Eq. 5.4. The modes of the WGM are strongly confined inside the resonator and the perturbation due to a modified dielectric environment is rather small.

Figure. 5.3 (a) shows the normalized scattering cross-section where various resonances can be seen due to the excitation of different modes with mode number n. Here, a sphere with a

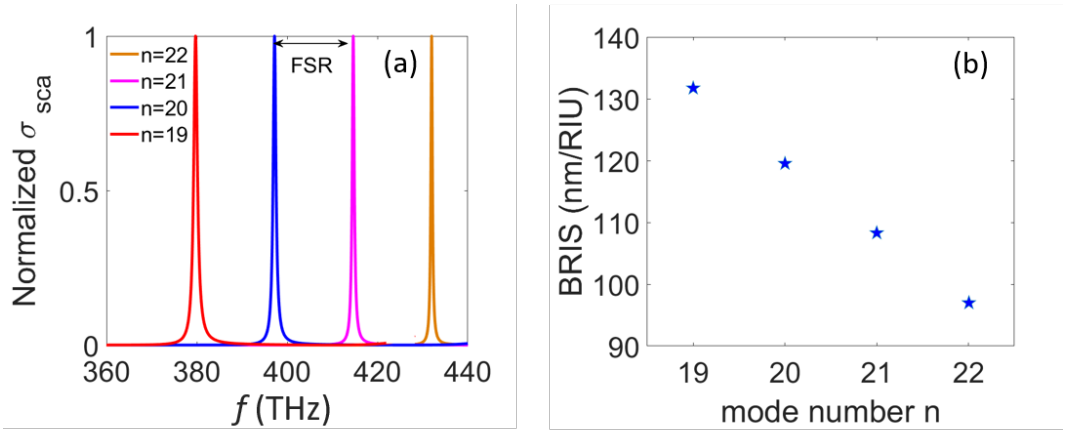

Figure 5.3 *(a) Fundamental mode of a silica sphere ($\varepsilon_{\mathrm{si}} = 2.25$) with a radius of 2 micron embedded in vacuum. Different color corresponds to different mode number as denoted in legend. FSR, which is defined as the distance between two resonance peaks, is also shown. (b) BRIS of the system, which is denoted by a star for each mode number.*

radius of 2 micron embedded in vacuum has been considered. The sphere is made of silica with a permittivity of 2.25. For the sake of clarity, we only consider modes with parity $k = 2$ and the fundamental mode of each mode number. The excitation field is always the corresponding VSH of each mode. It can be seen that the larger the mode number, the higher the resonance frequency. This is due to the fact that each resonance is the result of constructive interference of propagating WGM. The resonance frequency can be approximated by using standing wave approximation. We can imagine that the propagating WGM form a standing wave inside the resonator. This yields

$$\omega_0 \backsim \frac{\sqrt{\varepsilon_{\mathrm{eff}}}}{2\pi R}, \tag{5.8}$$

where R is the radius of the sphere and $\varepsilon_{\mathrm{eff}}$ is the effective permittivity experienced by the modes inside the resonator. Based on this approximation, the resonance frequency increases with respect to a higher mode number. Another conclusion that can be drawn from Eq. 5.8 is that the FSR of a spherical resonator is inversely proportional to the size of the sphere. The larger the sphere, the smaller its FSR.

Another thing worth to mention is the linewidth. Generally, modes with a lower mode number tend to have a broader linewidth. This fact can be understood since modes with a lower mode number tend to have longer evanescent tail outside the resonator. This fact makes the BRIS of modes with a lower mode number to be particularly high compared to modes with larger mode numbers, according to Eq. 5.4. To clarify this, Fig. 5.3 (b) shows the BRIS for modes with different mode numbers. We observe a drop of the sensitivity as the mode number increases. As previously mentioned, higher mode number exhibits a larger quality factor. These facts correlated very well with Eq. 5.4.

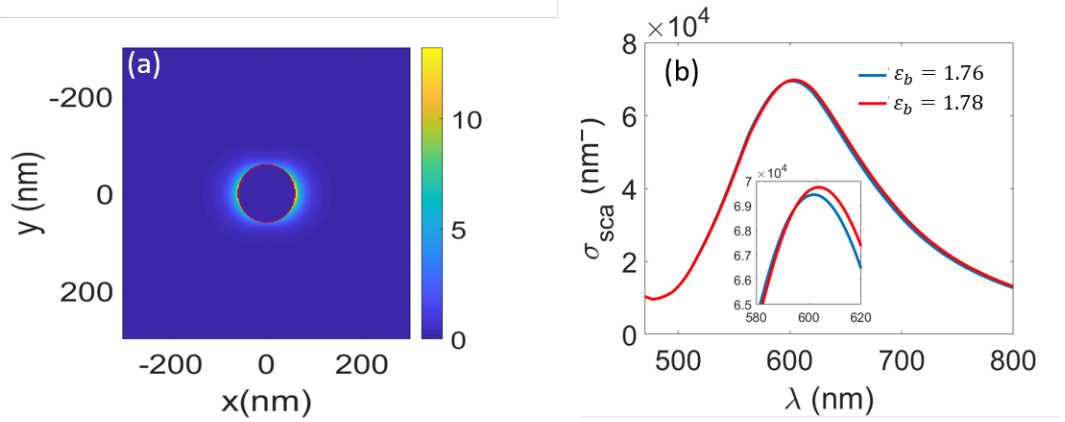

Figure 5.4 *(a) Intensity distribution of the modes for the case of a gold sphere with a radius of 60 nm embedded in a medium with refractive index of 1.76. The incident field is a VSH which corresponds to an electric dipole mode. The intensity is plotted at the resonance wavelength of 601.5 nm. (b) The scattering cross-section for different embedding media. The inset shows the spectral range around the resonance frequencies.*

5.1.3 Sensors based on plasmonic resonators

Another common type of optical sensors exploit metallic nanostructures that support surface plasmon polaritons. Depending on the general geometry of the metallic system, the supported plasmon polaritons can be divided into two classes, localized surface plasmon polaritons and propagating surface plasmon polaritons. In this chapter, however, we will focus our attention to the localized surface plasmon. Localized surface plasmon polaritons are supported when the size of the metallic resonator is very small compared to the wavelength. In this case, the quasi-static approximation is valid. They are excited at a specific frequency that depends (a) on the shape of the metallic nanostructure and (b) on the material from which the nanostructure is made. For a small spherical object, the resonance frequency is given by the Frölich condition,

$$(Re[\epsilon_{\text{metal}}(\omega_{\text{res}})] = -2\varepsilon_{\text{background}}. \tag{5.9}$$

Contrary to the dielectric resonators, where the maximum intensity of the mode is located inside the resonator, in plasmonic systems, the maximum intensity is always located at the interface between the metal and the background media. This fact can be seen in Fig. 5.4 (a), where the electric field amplitude around a small nanoparticle illuminated with a plane wave is shown.

In the case of localized surface plasmon polaritons, the modes are usually linked to the excitation of an electric dipole moment inside the particle because the size of the scatterer is quite small compared to the wavelength of interest. This is the reason that the intensity profile outside the scatterer has a dominant dipole radiation profile. By changing the background permittivity, the resonance position of the modes will shift, as can be seen in Fig. 5.4 (b) and can be easily explained from the aforementioned Fölich condition. In the case of a background permittivity equal to 1.76, the resonance occurs at 601.5 nm, and it is shifted to 603.6 nm when

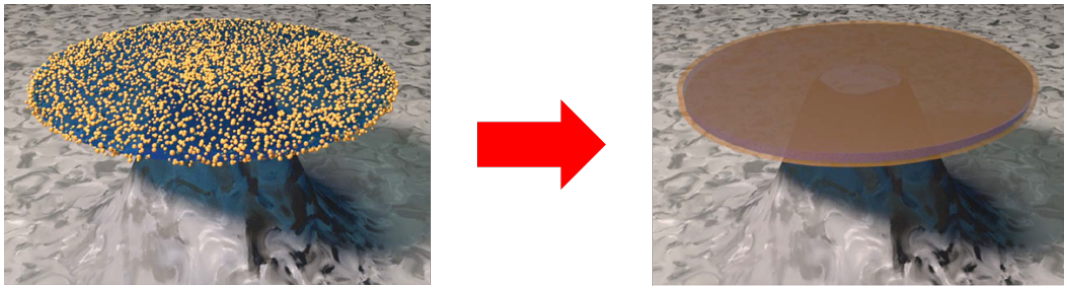

Figure 5.5 *Illustration of the hybrid disk resonator considered in this section. A silica microdisk is covered by gold NP at a rather high concentration (left). Using effective medium theory, the random asembly of gold NP can be modelled as a homogeneous layer with an effective permittivity (right). Adapted from P.3.*

the background permittivity is 1.78. This corresponds to a BRIS value of 279.4 nm/RIU, which is much larger compared to the BRIS values observed in WGM based resonators as presented in the previous section. This large BRIS value can be attributed to the fact that since the field is concentrated at the interface between the metal and the background medium, the field overlap with the surrounding medium is quite large. According to the reactive sensing principle, this translates directly to a large sensitivity. This, however, does not come for free. There are several important parameters which limit the applicability of this sensor. The linewidth of the resonance is quite broad because of the strong absorption of the light inside the particle, something that results in a less readable sensor. Another price that has to be paid is a large shot noise limit, meaning that this sensor resolution is quite low compared to its dielectric counterparts.

5.2 Combining whispering gallery mode resonator and plasmonic nanoparticles for biosensing application

In the previous sections, we see that the WGM based resonator usually has a high readability, but at the price of a lower sensitivity. On the other hand, plasmonic based sensors exhibit good sensitivity at the cost of less readability. In this section, we will show that by combining both types of sensors, a better performance can be achieved. The results presented here were developed in close collaboration with Carolin Klussman at AG Kalt in the Institute of Applied Physics (APH) at KIT. She calculated the field distribution and BRIS of the hybrid structure. This section is mainly based on P.3.

Here, we consider a microdisk made of silica with a permittivity of 2.25. The radius of the disk is 25 micron and it has a thickness of 1.2 micron. This microdisk is then covered with gold NPs with a radius of 25 nm. Using the effective medium approach, the problem can be simplified into a disk covered by a homogeneous layer with a certain effective permittivity, $\varepsilon_{\text{eff}}(\omega)$. The value of $\varepsilon_{\text{eff}}(\omega)$ can be calculated according to Eq. 2.4. The illustration of the considered scenario can

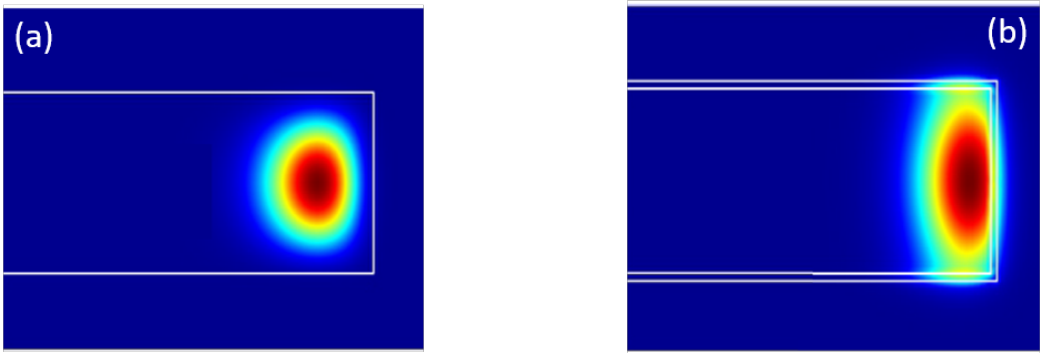

Figure 5.6 *Cross-sectional view of the field intensity of the fundamental mode of mode number 392 at the wavelength of 532 nm inside (a) a bare disk resonator with a radius of 25 µm and a height of 1.2 µm and (b) the same disk resonator which is covered by an effective shell with gold NP filling fraction 0.1. The radius of gold NP is 25 nm. The field is pulled outside due to the presence of the effective shell, resulting in the increase of the sensitivity. Here, the systems are embedded in water with a permittivity of 1.77. Adapted from P.3.*

be seen in Fig. 5.5.

The results presented in this section are based on Finite Element Simulation (FEM). We employ the eigenmode solver provided by JCMSuite for a direct calculation of the resonance frequency and Q-factors for several modes. The resulting complex eigenfrequency $\omega_{\text{res}} = \omega_{\text{real}} + i\omega_{\text{imag}}$ is then used to define the resonance frequency (ω_{real}) and its linewidth (ω_{imag}). The Q-factor can be computed directly from these two parameters, $Q = \omega_{\text{real}}/2\omega_{\text{imag}}$. In this section, we will focus our discussion on the fundamental TE mode for a selected mode number m, which denotes the azimuthal mode number.

Figure 5.6 (a) shows the cross-sectional view of the field intensity of the mode for the case of a silica disk only. This considered mode is the one with mode number $m = 392$. It can be seen that the electric field intensity is confined inside the disk, and the electric field intensity in the background medium is quite small. By adding an effective layer made from an ensemble of gold NPs, the mode intensity shifts outward. This results in a higher mode overlap with the surrounding medium, as can be seen in Fig. 5.6 (b). By analysing the intensity behavior from the reactive sensing principle point of view, as described in Eq. 5.5, which states that a higher mode overlap with the surrounding medium translates to a higher sensitivity, the analysis suggests that this dielectric core-effective shell structure is quite promising for a higher BRIS compared to the bare dielectric microdisk.

To understand the physics behind the shift of the spatial location where the intensity localizes, we need to understand the behavior of the effective permittivity obtained from Clausius-Mossotti effective medium theory. Figure 5.7 (a) shows the real part of $\varepsilon_{\text{eff}}(\omega)$ for several gold NPs filling fractions. A dispersion in the real part of the effective permittivity is observed for all filling fractions, where a stronger dispersion occurs for higher filling fractions. This stronger dispersion of the real part of the permittivity is always accompanied by a stronger loss, which is

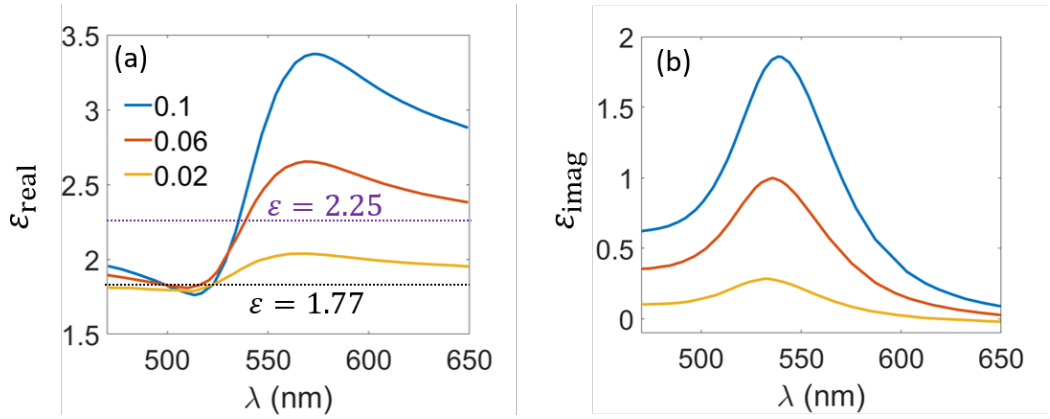

Figure 5.7 *(a) Real and (b) imaginary part of the effective permittivity of an effective homogeneous medium from an ensemble of gold NPs with a radius of 25 nm embedded in water for various filling fraction. The permittivity of water (silica) is denoted by black (purple) dotted line. Adapted from P.3.*

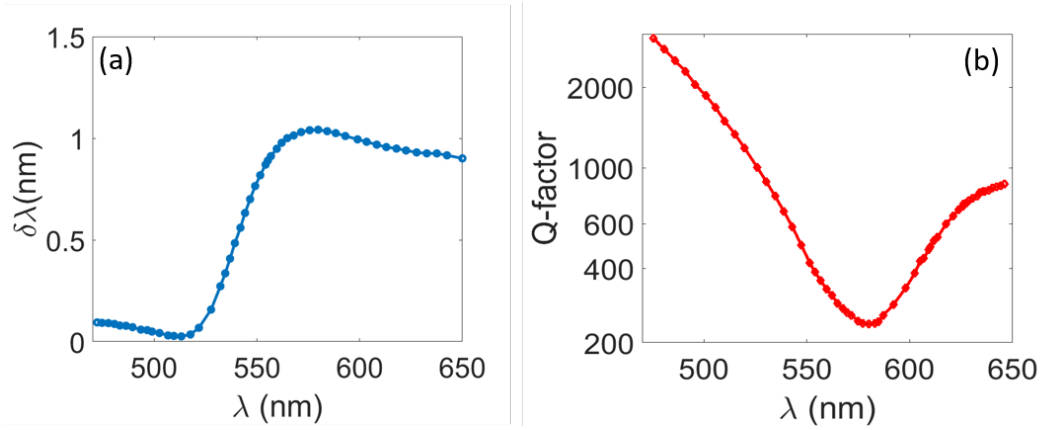

Figure 5.8 *(a) Shift of the resonance wavelength due to the effect of NP shell with a filling fraction of 0.023. The shift is determined by the difference between hybrid mode and bare disk with the same mode number. (b) Q-factor of hybrid disk. Adapted from P.3.*

described by the imaginary part of the effective permittivity, as shown in Fig. 5.7 (b). For our current purpose,we first consider a filling fraction of $f = 0.1$. Since the values of the effective permittivity for this filling fraction is larger than the disk permittivity (as denoted by green line) for wavelengths above 525 nm, this means that the mode will be more confined in the surrounding layer. However, due to the fact that the layer thickness is quite small, and the disk permittivity is larger than the background, This translates to the fact that the mode will be pulled outside compared to the mode of the bare disk. This analysis explains the result observed in Fig. 5.6 (b).

The next step is to analyse the effect of an effective layer on the sensing performance of the hybrid system. For this purpose, we fix the NP filling fraction to be $f = 0.023$. We choose this value to keep the absorption loss still relatively small, as can be seen in Fig. 5.7 (b). To

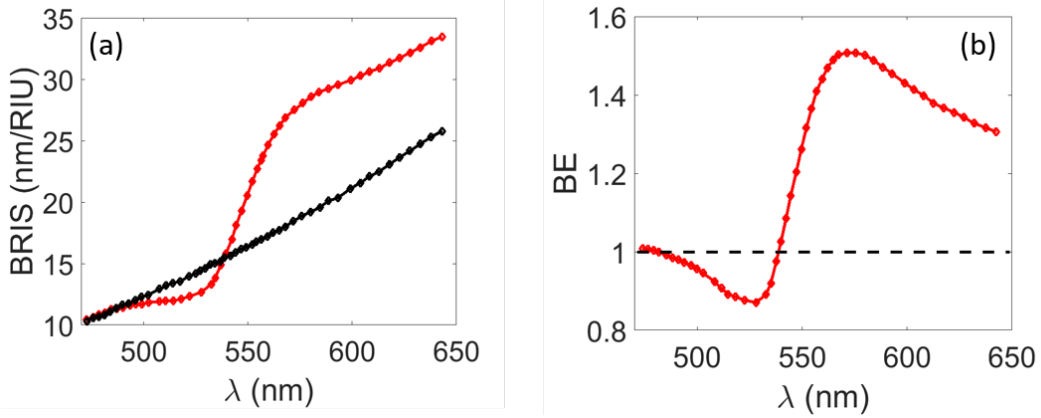

Figure 5.9 *(a) BRIS of a hybrid disk for the case of nanoparticles filling fraction f=0.023 (red) and the corresponding BRIS of bare disk with the same dimensions (black). (b) BRIS enhancement factor, BE, which quantifies the enhancement effect of the effective layer on the sensitivity. The black line represents the BE of bare disk. Adapted from P.3.*

understand the effect of this structure, we start by analyzing the behavior of the considered structure for the case of water ($\varepsilon = 1.77$) as the background medium. Note that, as we change the permittivity of the background medium, the effective permittivity of the shell will also change slightly, according to Eq. 2.4. This is a direct consequence of different Mie coefficients for the electric dipole moment in Eq. 2.47 when different background media are considered.

Contrary to the permittivity of the disk, in the spectral region of interest, the effective permittivity of the shell shows a strong dispersion. This fact affects the response of the hybrid system, as shown in Fig. 5.8. We plot the wavelength shift of the resonance of a hybrid system and its quality factor when compared to the bare disk without coating. Both quantities show a pronounced dependency with respect to the wavelength. A maximal change can be observed for a wavelength around 570 nm. This corresponds to the excitation wavelength where the real part of the effective permittivity of the shell material is close to its maximum. The underlying physics behind these relation can be explained by the fact mentioned previously, the higher the real part of shell permittivity, the more the mode pushed outside, which, in turn, increases the sensitivity of the system.

On the other hand, the modification of the resonance position is also accompanied by a strong decrease in the Q-factor of the system. This can be explained by examining Figs. 5.7 (a) and (b). Stronger resonance shift can be attributed to the stronger dispersion of the real part of the effective permittivity. This, in turn, implies stronger dispersion in the imaginary part of the effective permittivity. Higher imaginary part of the effective permittivity means higher absorption. Since the total Q-factor is the sum of the scattering and the absorption loss, as described in Eq. 5.3, this results in the reduced Q-factor of the system as observed in Fig. 5.8 (b). The reduction of the Q-factor can be several orders of magnitude compared to the Q-factor of a bare disk resonator (around 10^7).

After we are done with the analysis of the hybrid system for a fixed background medium, in the next step we will investigate the sensitivity of such a system. For this purpose, we consider the sensitivity with respect to the homogeneous change in the background medium, which is quantified by BRIS, as defined in Eq. 5.6. Recall that, by using the reactive sensing principle to analyze the intensity distribution shown in Fig. 5.6, we can expect a better sensitivity for our hybrid system. To confirm this initial guess, Fig. 5.9 (a) shows the BRIS values of a hybrid disk (red) and a bare disk (black). The BRIS of the hybrid system shows a different behavior compared to the BRIS of the microdisk. Depending on the WGM resonance position with respect to the NP resonance (at 532 nm), the BRIS of a hybrid system can be larger or smaller compared to the BRIS of an isolated microdisk structure.

To ease the comparison, we introduce the dimensionless BRIS enhancement factor BE. We define this parameter as the ratio of the BRIS of the hybrid system to the BRIS of an isolated microdisk with the same mode number. It allows us to extract and quantify the effect of the effective shell layer on the sensitivity enhancement, as plotted in Fig. 5.9 (b). The black line serves as the reference and it represents the BRIS of a bare dielectric structure. Whereas the BRIS of the hybrid system remains unchanged for a wavelength around 540 nm, the coupling to the effective layer induces a sensitivity enhancement for wavelengths longer than 540 nm and sensitivity reduction for wavelengths between 480-540 nm. By analysing this result and the value of the real part of the effective permittivity (shown in Fig. 5.7 (a)), we can conclude that these behaviors are the direct consequence of the effective permittivity of the shell. Between 480-540 nm, the value of the real part of the effective permittivity is lower than the permittivity of the background medium. This will result in a situation where the layer permittivity has a lower index contrast compared to the background medium. Because of this reason, the field intensity of the corresponding mode will be pulled inward, resulting in a lower field overlap with the surrounding medium. At a wavelength around 540 nm, the value of the real part of the effective permittivity is the same as the value of background permittivity. This means that the disk only see the effective layer as the background medium, resulting in the same sensitivity of hybrid disk and bare disk. For larger wavelengths, however, the value of the real part of effective permittivity is larger than the background permittivity, and due to this reason, the field will be pulled outward, resulting in a better sensitivity of the hybrid disk compared to the case of a bare disk.

The simulations presented here suggest that the sensing performance of a hybrid system is mainly dictated by the effective index of the shell. Depending on the operational wavelength, the sensitivity can be enhanced or decreased. This comes, however, at the cost of a strongly decreased quality factor of the modes, which affects the spectral resolution. To understand the effect of different NP density affecting the performance of our hybrid system, we plot in Fig. 5.10 the BRIS (black solid line) and Q factor (red solid line) of our hybrid microdisk with respect to the NP filling fraction. In the same figure, we also compare the performance of a fully gold coated disk with various thicknesses, as denoted by dotted lines. We fix our mode number to 392. We also plot the lowest tolerable Q-factor,$Q = 220$, as denoted by dashed black line. The lowest tolerable Q-factor is obtained from the discussion in section 5.1. The sensor is still readable if its FSR/Γ is larger than 0.55. In our case of a hybrid system, our FSR is

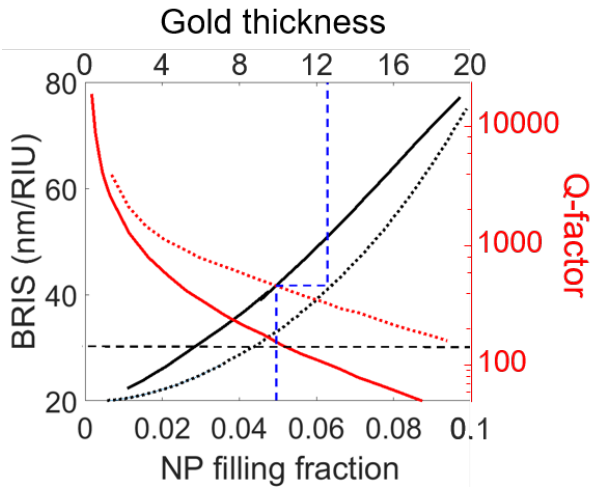

Figure 5.10 *(a) BRIS (black) and Q- factor (red) of a hybrid systems with mode number of 392. The solid lines denote the values for disk covered by NP with various filing fraction (lower x-axis), while the dotted lines denote the values for disk coated with gold layer for various layer thickness (upper x-axis). The black dashed line corresponds to the lowest tolerable Q-factor (Q=220). Blue lines shows one of the example where the BRIS of NP coated disk (with filling fraction of 0.05) matches the BRIS of gold coated disk (with metal thickness of 13.5 nm). Adapted from P.3.*

around 1.5 nm, which translates to the minimum tolerable Q-factor around 220. In Fig. 5.10 we denote this by the black dashed line. By analyzing this figure further, it can be concluded that the optimum enhancement without losing the readability is obtained if the value of the NP filling fraction is around 0.05.

As expected from the values of effective permittivities of the shell, the sensitivity of a hybrid system increases monotonically with increasing f due to the increase of the real part of the effective permittivity, as shown previously in Fig. 5.10. When the value of f exceeds 0.04, the value of the effective permittivity of the shell exceeds the permittivity of the core material, leading to higher mode overlap with the surrounding medium because the field is pulled to the outer region. However, the price to pay for this effect is the decrease of the Q-factor when the filling fraction is increased. This will restrict the readability of this hybrid system as it lowers the spectral resolution. Finding the optimum parameter, therefore, requires balancing the effect between high sensitivity and Q-factor.

In the same figure, we also plot the hybrid system with a fully coated gold layer, with its thickness denoted in the upper axis. The same trends are also observed. In this case, the maximum thickness for a good readability is found to be around 10 nm. From the experimental point of view, producing a smooth gold coating on a curved dielectric microdisk is a very challenging problem.[136–138] On the other hand, in the case of covering the bare disk with gold NPs, it can be easily done via self-assembly techniques and a good control of particle density can be achieved.[100,139] This means that using an ensemble of gold NPs, better performance and easier experimental realization can be expected compared to a fully coated gold layer. Overall,

we show better performance (higher BRIS and lower Q-factor) of an NP coated disk compared to a fully covered gold disk.

In this section, we investigated the hybrid sensing device comprised of a silica microdisk and ensemble of gold NPs. We treat the ensemble of NPs using effective medium theory. This allows us to investigate a large number of NP and explains the spectral behavior of the hybrid structure. By adding the effective layer onto a silica microdisk, it introduces different field distribution inside the resonator. This changes the sensitivity of the hybrid system relative to the sensitivity of a bare resonator. Depending on the value of the effective permittivity, the sensitivity of a hybrid system might be decreased or increased. Finally, we have shown the superiority of our system compared to a fully coated gold layer.

5.3 Summary

In this chapter, the basic principle of optical sensing devices was described. Generally, there always exists a trade-off between the sensitivity and the readability of the sensor, as the sensitivity depends on how much of the field is located outside the resonator. Two common types of optical resonators, which are often used as optical sensing devices, are presented. Dielectric-based sensors, which rely on field confinement inside the structure, with the main advantage of a sharp resonance profile, and plasmonic-based sensor, which rely on field confinement at the interface between metal and the surrounding medium. This results in high sensitivity due to larger field outside of the resonator when compared to the dielectric one. By combining both types of resonators, a better performance can be observed. The sensitivity of the resulting hybrid structure between a plasmonic based sensor and a dielectric based sensor can be analyzed conveniently from the field distribution of the modes supported by such a hybrid structure.

Chapter 6
6 Conclusions and Future Perspectives

6.1 Conclusions

Throughout this thesis, we have shown different formalisms of the T-matrix method. We start by the T-matrix formalism for an individual particle, and then build the T-matrix of multiple particles in their local coordinate system, before we shrink this T-matrix into the T-matrix in global coordinates system. These different formalisms are the main tools for the further explorations in this thesis.

First, we apply the T-matrix method to develop a framework for the description of the modes in form of eigenmodes and singular modes. By using eigenmodes, we have shown how to decompose the scattering cross section of different structures in terms of the contribution from each modes. We also discussed the eigenmodes from two different perspectives, the collective modes, which are obtained from the global coordinates formalism and the individual modes, which are obtained from local coordinates formalism. The method to transform the description from one perspective to the other perspective was also discussed. The second framework, singular modes, was also shown and the decomposition of the scattering cross section was done. Contrary to the eigenmodes framework, singular modes form an orthonormal basis set. This enables us to discuss the response with a minimum number of possible term. We have shown that Fano resonances, which arise due to the coupling between different nonorthogonal eigenmodes, can also be considered as an inherent property of singular modes.

Departing from this, we have shown the application of the T-matrix method in self assembled metamaterials. The experimentally observable responses of the bulk self-assembled metamaterials, which are usually described by averaging the response of its individual meta-atom rotationally, can be calculated directly from the T-matrix of its individual meta-atom. This provides a way for a fast calculation compared to the manual rotational averaging method. By using this extraction method, we developed a theoretical foundation to quantify Fano signature in the self-assembled metamaterials by using eigenmodes and singular modes framework. This allows us to discuss whether a particular response is due to incoherent summation of different modes or if it is due to the coupling between different nonorthogonal modes.

Lastly, we discussed the application of the T-matrix in an optical sensing device. We have shown that by hybridizing plasmonic and whispering gallery mode based sensors, the sensitivity of the sensing device can be tuned.

After all of these discussions, we may return to the two questions presented at the very beginning of this thesis. I will try to answer these questions based on what we have presented

in this thesis.

How to understand light interaction with an ensemble of objects?

The interaction between light and an ensemble of objects can be understood by using the concept of modes. Here, we show that different kind of responses can be decomposed in terms of modes, and the analysis of modes provides a convenient and powerful way to understand the response of the system for any arbitrary incident light.

Can we get something out of it?

In this thesis, we have shown several applications, which are based on the understanding of modes. Fano resonances, which are the result of the coupling between different nonorthogonal modes, is a useful phenomenon with direct applications in several fields, such as optical switches and enhanced Raman scattering. We also have shown another example of the application of the interaction between light and matter in the form of optical sensing devices, which might be useful for different applications, such as biomedicine. Of course, this list is far from over, as many other applications which are not discussed in this thesis are also possible. This shows that there is a large potential for applications out there.

6.2 Future Perspectives

Based on the content presented in this thesis, one might ask the following question: So, what's next? I will try to answer this question based on each chapter presented in this thesis.

The modal analysis presented in chapter 3 will be useful for designing metamaterials with the desired properties. The ability to transform modes from individual to collective modes provides a way to simplify the description of modes, albeit with less information. Designing scatterers which consist of multiple particles will benefit from this fact. Among them are: structures which support Fano type response, second harmonic generation from an ensemble of particles, and electromagnetically induced transparency. On the other hand, singular modes picture offers a way to design a particular type of the incident field for a desired optical response.

In chapter 4, the method to extract the experimentally observable parameters of the metamaterials fabricated from self-assembly approach directly from the T-matrix of its constituent meta-atoms proves to be a fast and powerful method. However, currently our limitation requires us to stay in the limit of high dilution. By considering an effective T-matrix of a particular meta-atom, which can be obtained by using the higher order corrections from the Born approximation, it will open up the possibility to extract the experimental parameters for the case of a higher filling fraction. The higher filling fraction offers a plethora of new applications, as the optical response of such systems is usually much stronger compared to its lower density counterparts. On the other hand, the analysis of Fano responses in self-assembled metamaterials will act as the theoretical foundation to design an isotropic Fano scatterer, which was previously thought to be impossible. In this thesis, we have shown the analysis of isotropic Fano response by using collective modes, where the description can be simplified tremendously, at the cost of

losing the details of each subsystem. The individual modes will prove to be useful to understand the behavior of subsystems and the analysis of Fano response can be extended by using the individual modes to gain more physical insight.

In chapter 5, the hybrid optical sensing device analysis employing the Clausius-Mossoti effective medium approach can also be applied to an ensemble of different particles, e.g. nanorods. The resonance position of a nanorod can be tuned by varying the length of the nanorod. Another important aspect is that the polarizability of a nanorod in one direction can be much stronger than that of a nanosphere, giving rise to a stronger dispersion in the effective permittivity of the ensemble. These two facts can help to build a hybrid sensor with better performance than the one discussed in chapter 5.

Bibliography

[1] A. F. Fercher, W. Drexler, C. K. Hitzenberger, and T. Lasser, "Optical coherence tomography-principles and applications," *Reports on Progress in Physics*, vol. 66, no. 2, p. 239, 2003.

[2] J. M. Schmitt, "Optical coherence tomography (OCT): A review," *IEEE Journal of Selected Topics in Quantum Electronics*, vol. 5, no. 4, p. 1205, 1999.

[3] C. Koos, P. Vorreau, T. Vallaitis, P. Dumon, W. Bogaerts, R. Baets, B. Esembeson, I. Biaggio, T. Michinobu, F. Diederich, W. Freude, and J. Leuthold, "All-optical high-speed signal processing with silicon–organic hybrid slot waveguides," *Nature Photonics*, vol. 3, no. 4, p. 216, 2009.

[4] A. V. Kildishev, A. Boltasseva, and V. M. Shalaev, "Planar photonics with metasurfaces," *Science*, vol. 339, no. 6125, p. 1232009, 2013.

[5] H. Elgala, R. Mesleh, and H. Haas, "Indoor optical wireless communication: potential and state-of-the-art," *IEEE Communications Magazine*, vol. 49, no. 9, p. 56, 2011.

[6] F. Morichetti, C. Ferrari, A. Canciamilla, and A. Melloni, "The first decade of coupled resonator optical waveguides: bringing slow light to applications," *Laser & Photonics Reviews*, vol. 6, no. 1, p. 74, 2012.

[7] B. Kuswandi, Nuriman, J. Huskens, and W. Verboom, "Optical sensing systems for microfluidic devices: A review," *Analytica Chimica Acta*, vol. 601, no. 2, p. 141, 2007.

[8] J. Verrelst, G. Camps-Valls, J. Muñoz-Marí, J. P. Rivera, F. Veroustraete, J. G. Clevers, and J. Moreno, "Optical remote sensing and the retrieval of terrestrial vegetation bio-geophysical properties–a review," *ISPRS Journal of Photogrammetry and Remote Sensing*, vol. 108, p. 273, 2015.

[9] N. Joshi, M. Baumann, A. Ehammer, R. Fensholt, K. Grogan, P. Hostert, M. Jepsen, T. Kuemmerle, P. Meyfroidt, E. Mitchard, J. Reiche, C. M. Ryan, and B. Waske, "A review of the application of optical and radar remote sensing data fusion to land use mapping and monitoring," *Remote Sensing*, vol. 8, no. 1, p. 70, 2016.

[10] M. Li, S. K. Cushing, and N. Wu, "Plasmon-enhanced optical sensors: A review," *Analyst*, vol. 140, no. 2, p. 386, 2015.

[11] J. L. West and N. J. Halas, "Engineered nanomaterials for biophotonics applications: Improving sensing, imaging, and therapeutics," *Annual Review of Biomedical Engineering*, vol. 5, no. 1, p. 285, 2003.

[12] J. D. Joannopoulos, S. G. Johnson, J. N. Winn, and R. D. Meade, "Molding the flow of light," *Princeton Univ. Press, Princeton, NJ [ua]*, 2008.

[13] C. A. Balanis, *Antenna theory: Analysis and design*. John wiley & sons, New Jersey, 2016.

[14] D. J. Griffiths, *Introduction to electrodynamics*. Cambridge university press, Cambridge, 2017.

[15] I. S. Nefedov and S. A. Tretyakov, "Photonic band gap structure containing metamaterial with negative permittivity and permeability," *Physical Review E*, vol. 66, no. 3, p. 036611, 2002.

[16] P. Parimi, W. Lu, P. Vodo, J. Sokoloff, J. Derov, and S. Sridhar, "Negative refraction and left-handed electromagnetism in microwave photonic crystals," *Physical Review Letters*, vol. 92, no. 12, p. 127401, 2004.

[17] M. A. Noginov and V. A. Podolskiy, *Tutorials in metamaterials*. CRC press, Florida, 2011.

[18] C. M. Soukoulis and M. Wegener, "Past achievements and future challenges in the development of three-dimensional photonic metamaterials," *Nature Photonics*, vol. 5, no. 9, p. 523, 2011.

[19] A. Poddubny, I. Iorsh, P. Belov, and Y. Kivshar, "Hyperbolic metamaterials," *Nature Photonics*, vol. 7, no. 12, p. 948, 2013.

[20] G. Kenanakis, A. Xomalis, A. Selimis, M. Vamvakaki, M. Farsari, M. Kafesaki, C. M. Soukoulis, and E. N. Economou, "Three-dimensional infrared metamaterial with asymmetric transmission," *ACS Photonics*, vol. 2, no. 2, p. 287, 2015.

[21] A. Starr, P. Rye, D. Smith, and S. Nemat-Nasser, "Fabrication and characterization of a negative-refractive-index composite metamaterial," *Physical Review B*, vol. 70, no. 11, p. 113102, 2004.

[22] S. Linden, C. Enkrich, M. Wegener, J. Zhou, T. Koschny, and C. M. Soukoulis, "Magnetic response of metamaterials at 100 terahertz," *Science*, vol. 306, no. 5700, p. 1351, 2004.

[23] S. Obrien, D. McPeake, S. Ramakrishna, and J. Pendry, "Near-infrared photonic band gaps and nonlinear effects in negative magnetic metamaterials," *Physical Review B*, vol. 69, no. 24, p. 241101, 2004.

[24] T. Bückmann, N. Stenger, M. Kadic, J. Kaschke, A. Frölich, T. Kennerknecht, C. Eberl, M. Thiel, and M. Wegener, "Tailored 3D mechanical metamaterials made by dip-in direct-laser-writing optical lithography," *Advanced Materials*, vol. 24, no. 20, p. 2710, 2012.

[25] W. Wu, Z. Yu, S.-Y. Wang, R. S. Williams, Y. Liu, C. Sun, X. Zhang, E. Kim, Y. R. Shen, and N. X. Fang, "Mid-infrared metamaterials fabricated by nanoimprint lithography," *Applied Physics Letters*, vol. 90, no. 6, p. 063107, 2007.

[26] J. Kaschke and M. Wegener, "Gold triple-helix mid-infrared metamaterial by sted-inspired laser lithography," *Optics Letters*, vol. 40, no. 17, p. 3986, 2015.

[27] S. Vignolini, N. A. Yufa, P. S. Cunha, S. Guldin, I. Rushkin, M. Stefik, K. Hur, U. Wies-

ner, J. J. Baumberg, and U. Steiner, "A 3D optical metamaterial made by self-assembly," *Advanced Materials*, vol. 24, no. 10, p. OP23, 2012.

[28] A. M. Urbas, Z. Jacob, L. D. Negro, N. Engheta, A. D. Boardman, P. Egan, A. B. Khanikaev, V. Menon, M. Ferrera, N. Kinsey, C. DeVault, J. Kim, V. Shalaev, A. Boltasseva, J. Valentine, C. Pfeiffer, A. Grbic, E. Narimanov, L. Zhu, S. Fan, A. Alù, E. Poutrina, N. M. Litchinitser, M. A. Noginov, K. F. MacDonald, E. Plum, X. Liu, P. F. Nealey, C. R. Kagan, C. B. Murray, D. A. Pawlak, I. I. Smolyaninov, V. N. Smolyaninova, and D. Chanda, "Roadmap on optical metamaterials," *Journal of Optics*, vol. 18, p. 093005, aug 2016.

[29] S. Mühlig, C. Rockstuhl, V. Yannopapas, T. Bürgi, N. Shalkevich, and F. Lederer, "Optical properties of a fabricated self-assembled bottom-up bulk metamaterial," *Optics Express*, vol. 19, no. 10, p. 9607, 2011.

[30] Z. Chen, X. Wang, Y. Qi, S. Yang, J. A. Soares, B. A. Apgar, R. Gao, R. Xu, Y. Lee, X. Zhang, J. Yao, and L. W. Martin, "Self-assembled, nanostructured, tunable metamaterials via spinodal decomposition," *ACS Nano*, vol. 10, no. 11, p. 10237, 2016.

[31] A. K. Wong, R. A. Ferguson, and S. M. Mansfield, "The mask error factor in optical lithography," *IEEE Transactions on Semiconductor Manufacturing*, vol. 13, no. 2, p. 235, 2000.

[32] Y. Nakajima, T. Sato, R. Inanami, T. Nakasugi, and T. Higashiki, "Aberration budget in extreme ultraviolet lithography," in *Emerging Lithographic Technologies XII*, p. 69211A, International Society for Optics and Photonics, 2008.

[33] H. J. Levinson, *Principles of lithography*, vol. 146. SPIE press, Washington, 2005.

[34] L. C. Glangchai, M. Caldorera-Moore, L. Shi, and K. Roy, "Nanoimprint lithography based fabrication of shape-specific, enzymatically-triggered smart nanoparticles," *Journal of Controlled Release*, vol. 125, no. 3, p. 263, 2008.

[35] M. S. Rill, C. Plet, M. Thiel, I. Staude, G. Von Freymann, S. Linden, and M. Wegener, "Photonic metamaterials by direct laser writing and silver chemical vapour deposition," *Nature Materials*, vol. 7, no. 7, p. 543, 2008.

[36] K. Sakoda, *Optical properties of photonic crystals*. Springer Science & Business Media, Berlin, 2004.

[37] C. Fietz, Y. Urzhumov, and G. Shvets, "Complex k band diagrams of 3D metamaterial/photonic crystals.," *Optics Express*, vol. 19, no. 20, p. 19027, 2011.

[38] A. Taflove and S. C. Hagness, *Computational electrodynamics: The finite-difference time-domain method*. Artech house, London, 2005.

[39] S. Rao, D. Wilton, and A. Glisson, "Electromagnetic scattering by surfaces of arbitrary shape," *IEEE Transactions on Antennas and Propagation*, vol. 30, no. 3, p. 409, 1982.

[40] B. T. Draine and P. J. Flatau, "Discrete-dipole approximation for scattering calculations," *Journal of Optical Society of America A*, vol. 11, no. 4, p. 1491, 1994.

[41] R. Mittra and U. Pekel, "A new look at the perfectly matched layer (PML) concept for

the reflectionless absorption of electromagnetic waves," *IEEE Microwave and Guided Wave Letters*, vol. 5, no. 3, p. 84, 1995.

[42] P. Waterman, "Matrix formulation of electromagnetic scattering," *Proceedings of the IEEE*, vol. 53, no. 8, p. 805, 1965.

[43] N. I. Landy, S. Sajuyigbe, J. J. Mock, D. R. Smith, and W. J. Padilla, "Perfect metamaterial absorber," *Physical Review Letters*, vol. 100, no. 20, p. 207402, 2008.

[44] E. E. Narimanov and A. V. Kildishev, "Optical black hole: Broadband omnidirectional light absorber," *Applied Physics Letters*, vol. 95, no. 4, p. 041106, 2009.

[45] N. Liu, M. Mesch, T. Weiss, M. Hentschel, and H. Giessen, "Infrared perfect absorber and its application as plasmonic sensor," *Nano Letters*, vol. 10, no. 7, p. 2342, 2010.

[46] B. Wang, T. Koschny, and C. M. Soukoulis, "Wide-angle and polarization-independent chiral metamaterial absorber," *Physical Review B*, vol. 80, no. 3, p. 033108, 2009.

[47] Y. Ye and S. He, "90° polarization rotator using a bilayered chiral metamaterial with giant optical activity," *Applied Physics Letters*, vol. 96, no. 20, p. 203501, 2010.

[48] E. Plum, V. Fedotov, and N. Zheludev, "Optical activity in extrinsically chiral metamaterial," *Applied Physics Letters*, vol. 93, no. 19, p. 191911, 2008.

[49] C. J. Stevens, C. W. Chan, K. Stamatis, and D. J. Edwards, "Magnetic metamaterials as 1-D data transfer channels: An application for magneto-inductive waves," *IEEE Transactions on Microwave Theory and Techniques*, vol. 58, no. 5, p. 1248, 2010.

[50] S. J. Franson and R. W. Ziolkowski, "Gigabit per second data transfer in high-gain metamaterial structures at 60 GHz," *IEEE Transactions on Antennas and Propagation*, vol. 57, no. 10, p. 2913, 2009.

[51] B. Wang, K. H. Teo, T. Nishino, W. Yerazunis, J. Barnwell, and J. Zhang, "Wireless power transfer with metamaterials," in *Proceedings of the 5th European Conference on Antennas and Propagation (EUCAP)*, p. 3905, IEEE, 2011.

[52] W. Cai, U. K. Chettiar, A. V. Kildishev, and V. M. Shalaev, "Optical cloaking with metamaterials," *Nature Photonics*, vol. 1, no. 4, p. 224, 2007.

[53] H. Chen, B.-I. Wu, B. Zhang, and J. A. Kong, "Electromagnetic wave interactions with a metamaterial cloak," *Physical Review Letters*, vol. 99, no. 6, p. 063903, 2007.

[54] M. G. Silveirinha, A. Alù, and N. Engheta, "Parallel-plate metamaterials for cloaking structures," *Physical Review E*, vol. 75, no. 3, p. 036603, 2007.

[55] N. Liu, T. Weiss, M. Mesch, L. Langguth, U. Eigenthaler, M. Hirscher, C. Sonnichsen, and H. Giessen, "Planar metamaterial analogue of electromagnetically induced transparency for plasmonic sensing," *Nano Letters*, vol. 10, no. 4, p. 1103, 2009.

[56] T. Chen, S. Li, and H. Sun, "Metamaterials application in sensing," *Sensors*, vol. 12, no. 3, p. 2742, 2012.

[57] R. Melik, E. Unal, N. Kosku Perkgoz, C. Puttlitz, and H. V. Demir, "Flexible metamaterials

for wireless strain sensing," *Applied Physics Letters*, vol. 95, no. 18, p. 181105, 2009.

[58] A. Ishimaru, S. Jaruwatanadilok, and Y. Kuga, "Generalized surface plasmon resonance sensors using metamaterials and negative index materials," *Progress In Electromagnetics Research*, vol. 51, p. 139, 2005.

[59] A. Alu and N. Engheta, "Dielectric sensing in ε-near-zero narrow waveguide channels," *Physical Review B*, vol. 78, no. 4, p. 045102, 2008.

[60] M. R. Foreman, J. D. Swaim, and F. Vollmer, "Whispering gallery mode sensors," *Advances in Optics and Photonics*, vol. 7, no. 2, p. 168, 2015.

[61] F. Vollmer and S. Arnold, "Whispering-gallery-mode biosensing: label-free detection down to single molecules," *Nature Methods*, vol. 5, no. 7, p. 591, 2008.

[62] L. He, Ş. K. Özdemir, J. Zhu, W. Kim, and L. Yang, "Detecting single viruses and nanoparticles using whispering gallery microlasers," *Nature Nanotechnology*, vol. 6, no. 7, p. 428, 2011.

[63] D. M. Rissin, C. W. Kan, T. G. Campbell, S. C. Howes, D. R. Fournier, L. Song, T. Piech, P. P. Patel, L. Chang, A. J. Rivnak, E. P. Ferrell, J. D. Randall, G. K. Provuncher, D. R. Walt, and D. C. Duffy, "Single-molecule enzyme-linked immunosorbent assay detects serum proteins at subfemtomolar concentrations," *Nature Biotechnology*, vol. 28, no. 6, p. 595, 2010.

[64] M. D. Baaske, M. R. Foreman, and F. Vollmer, "Single-molecule nucleic acid interactions monitored on a label-free microcavity biosensor platform," *Nature Nanotechnology*, vol. 9, no. 11, p. 933, 2014.

[65] J. D. Jackson, "Classical electrodynamics third edition," *Wiley, New York*, 1998.

[66] C. F. Bohren and D. R. Huffman, *Absorption and scattering of light by small particles*. John Wiley & Sons, New York, 2008.

[67] G. Mie, "Beiträge zur optik trüber medien, speziell kolloidaler metallösungen," *Annalen der Physik*, vol. 330, no. 3, p. 377, 1908.

[68] M. Fruhnert, I. Fernandez-Corbaton, V. Yannopapas, and C. Rockstuhl, "Computing the T-matrix of a scattering object with multiple plane wave illuminations," *Beilstein Journal of Nanotechnology*, vol. 8, p. 614, 2017.

[69] R. A. Horn, R. A. Horn, and C. R. Johnson, *Matrix analysis*. Cambridge university press, Cambridge, 1990.

[70] W. Chew, *Waves and fields in inhomogeneous media*. Electromagnetic waves, Willey, New York, 1996.

[71] J. Li, X. Wang, and T. Wang, "On the validity of Born approximation," *Progress In Electromagnetics Research*, vol. 107, p. 219, 2010.

[72] V. Twersky, "Multiple scattering of electromagnetic waves by arbitrary configurations," *Journal of Mathematical Physics*, vol. 8, no. 3, p. 589, 1967.

[73] A. Rusanu, G. M. Stocks, Y. Wang, and J. S. Faulkner, "Green's functions in full-potential

multiple-scattering theory," *Physical Review B*, vol. 84, no. 3, p. 035102, 2011.

[74] Y.-L. Xu, "Electromagnetic scattering by an aggregate of spheres," *Applied Optics*, vol. 34, no. 21, p. 4573, 1995.

[75] S. Stein, "Addition theorems for spherical wave functions," *Quarterly of Applied Mathematics*, vol. 19, no. 1, p. 15, 1961.

[76] Y.-L. Xu, "Efficient evaluation of vector translation coefficients in multiparticle light-scattering theories," *Journal of Computational Physics*, vol. 139, no. 1, p. 137, 1998.

[77] G. B. Arfken and H. J. Weber, *Mathematical methods for physicists*. Academic press, Massachusetts, 1999.

[78] C. Kittel, *Introduction to Solid State Physics*. Wiley, 8 ed., 2004.

[79] J. Mäkitalo, M. Kauranen, and S. Suuriniemi, "Modes and resonances of plasmonic scatterers," *Physical Review B*, vol. 89, no. 16, p. 165429, 2014.

[80] C. E. Baum, "The singularity expansion method," in *Transient electromagnetic fields*, Springer, 1976.

[81] R. Harrington and J. Mautz, "Theory of characteristic modes for conducting bodies," *IEEE Transactions on Antennas and Propagation*, vol. 19, no. 5, p. 622, 1971.

[82] R. Garbacz and R. Turpin, "A generalized expansion for radiated and scattered fields," *IEEE Transactions on Antennas and Propagation*, vol. 19, no. 3, p. 348, 1971.

[83] D. J. Bergman and D. Stroud, "Theory of resonances in the electromagnetic scattering by macroscopic bodies," *Physical Review B*, vol. 22, no. 8, p. 3527, 1980.

[84] X. Zheng, V. Volskiy, V. K. Valev, G. A. Vandenbosch, and V. V. Moshchalkov, "Line position and quality factor of plasmonic resonances beyond the quasi-static limit: A full-wave eigenmode analysis route," *IEEE Journal of Selected Topics in Quantum Electronics*, vol. 19, no. 3, p. 4600908, 2013.

[85] B. Hopkins, A. N. Poddubny, A. E. Miroshnichenko, and Y. S. Kivshar, "Revisiting the physics of Fano resonances for nanoparticle oligomers," *Physical Review A*, vol. 88, no. 5, p. 053819, 2013.

[86] B. Hopkins, D. S. Filonov, S. B. Glybovski, and A. E. Miroshnichenko, "Hybridization and the origin of Fano resonances in symmetric nanoparticle trimers," *Physical Review B*, vol. 92, no. 4, p. 045433, 2015.

[87] N. A. Gippius, T. Weiss, S. G. Tikhodeev, and H. Giessen, "Resonant mode coupling of optical resonances in stacked nanostructures," *Optics Express*, vol. 18, p. 7569, Mar 2010.

[88] D. A. Bykov and L. L. Doskolovich, "Numerical methods for calculating poles of the scattering matrix with applications in grating theory," *Journal of Lightwave Technology*, vol. 31, p. 793, Mar 2013.

[89] D. A. Powell, "Resonant dynamics of arbitrarily shaped meta-atoms," *Physical Review B*, vol. 90, p. 075108, Aug 2014.

[90] M. S. Khajeahsani, A. Shahmansouri, M. J. Armand, and B. Rashidian, "Plasmonic resonance mode extraction based on the T-matrix method," *Journal of the Optical Society of America B*, vol. 32, p. 2333, Nov 2015.

[91] C. Sauvan, J. P. Hugonin, I. S. Maksymov, and P. Lalanne, "Theory of the spontaneous optical emission of nanosize photonic and plasmon resonators," *Physical Review Letters*, vol. 110, p. 237401, Jun 2013.

[92] P. Lalanne, W. Yan, K. Vynck, C. Sauvan, and J.-P. Hugonin, "Light interaction with photonic and plasmonic resonances," *Laser Photonics Reviews*, vol. 12, no. 5, p. 1700113, 2018.

[93] W. Yan, R. Faggiani, and P. Lalanne, "Rigorous modal analysis of plasmonic nanoresonators," *Physical Review B*, vol. 97, no. 20, p. 205422, 2018.

[94] V. Myroshnychenko, J. Rodríguez-Fernández, I. Pastoriza-Santos, A. M. Funston, C. Novo, P. Mulvaney, L. M. Liz-Marzan, and F. J. G. de Abajo, "Modelling the optical response of gold nanoparticles," *Chemical Society Reviews*, vol. 37, no. 9, p. 1792, 2008.

[95] M. Fruhnert, S. Mühlig, F. Lederer, and C. Rockstuhl, "Towards negative index self-assembled metamaterials," *Physical Review B*, vol. 89, no. 7, p. 075408, 2014.

[96] A. H. Sihvola, "Character of surface plasmons in layered spherical structures," *Progress In Electromagnetics Research*, vol. 62, p. 317, 2006.

[97] C. Helgert, C. Rockstuhl, C. Etrich, C. Menzel, E.-B. Kley, A. Tünnermann, F. Lederer, and T. Pertsch, "Effective properties of amorphous metamaterials," *Physical Review B*, vol. 79, no. 23, p. 233107, 2009.

[98] M. Albooyeh, S. Kruk, C. Menzel, C. Helgert, M. Kroll, A. Krysinski, M. Decker, D. N. Neshev, T. Pertsch, C. Etrich, C. Rockstuhl, S. A. Tretyakov, C. R. Simovski, and Y. S. Kivshar, "Resonant metasurfaces at oblique incidence: interplay of order and disorder," *Scientific Reports*, vol. 4, p. 4484, 2014.

[99] C. G. Cullen, *Matrices and linear transformations*. Courier Corporation, New York, 2012.

[100] C. Rockstuhl and T. Scharf, *Amorphous nanophotonics*. Springer Science & Business Media, Heidelberg, 2013.

[101] H.-T. Chen, W. J. Padilla, J. M. Zide, A. C. Gossard, A. J. Taylor, and R. D. Averitt, "Active terahertz metamaterial devices," *Nature*, vol. 444, no. 7119, p. 597, 2006.

[102] G. Dolling, M. Wegener, C. M. Soukoulis, and S. Linden, "Negative-index metamaterial at 780 nm wavelength," *Optics Letters*, vol. 32, no. 1, p. 53, 2007.

[103] C. Enkrich, F. Pérez-Willard, D. Gerthsen, J. Zhou, T. Koschny, C. M. Soukoulis, M. Wegener, and S. Linden, "Focused-ion-beam nanofabrication of near-infrared magnetic metamaterials," *Advanced Materials*, vol. 17, no. 21, p. 2547, 2005.

[104] M. Esposito, V. Tasco, F. Todisco, A. Benedetti, D. Sanvitto, and A. Passaseo, "Three dimensional chiral metamaterial nanospirals in the visible range by vertically compensated

focused ion beam induced-deposition," *Advanced Optical Materials*, vol. 2, no. 2, p. 154, 2014.

[105] J. Henzie, M. Grünwald, A. Widmer-Cooper, P. L. Geissler, and P. Yang, "Self-assembly of uniform polyhedral silver nanocrystals into densest packings and exotic superlattices," *Nature Materials*, vol. 11, no. 2, p. 131, 2012.

[106] A. L. Rogach, "Binary superlattices of nanoparticles: Self-assembly leads to metamaterials," *Angewandte Chemie International Edition*, vol. 43, no. 2, p. 148, 2004.

[107] P. Wang, S. Gaitanaros, S. Lee, M. Bathe, W. M. Shih, and Y. Ke, "Programming self-assembly of DNA origami honeycomb two-dimensional lattices and plasmonic metamaterials," *Journal of the American Chemical Society*, vol. 138, no. 24, p. 7733, 2016.

[108] Y. Yin, Y. Lu, B. Gates, and Y. Xia, "Template-assisted self-assembly: a practical route to complex aggregates of monodispersed colloids with well-defined sizes, shapes, and structures," *Journal of the American Chemical Society*, vol. 123, no. 36, p. 8718, 2001.

[109] C. Simovski, "Material parameters of metamaterials (a review)," *Optics and Spectroscopy*, vol. 107, no. 5, p. 726, 2009.

[110] Y. Liu and X. Zhang, "Metamaterials: a new frontier of science and technology," *Chemical Society Reviews*, vol. 40, no. 5, p. 2494, 2011.

[111] A. Movchan and S. Guenneau, "Split-ring resonators and localized modes," *Physical Review B*, vol. 70, no. 12, p. 125116, 2004.

[112] J. A. Fan, C. Wu, K. Bao, J. Bao, R. Bardhan, N. J. Halas, V. N. Manoharan, P. Nordlander, G. Shvets, and F. Capasso, "Self-assembled plasmonic nanoparticle clusters," *Science*, vol. 328, no. 5982, p. 1135, 2010.

[113] B. Gong, X. Zhao, Z. Pan, S. Li, X. Wang, Y. Zhao, and C. Luo, "A visible metamaterial fabricated by self-assembly method," *Scientific Reports*, vol. 4, p. 4713, 2014.

[114] A. Kuzyk, R. Schreiber, Z. Fan, G. Pardatscher, E.-M. Roller, A. Högele, F. C. Simmel, A. O. Govorov, and T. Liedl, "DNA-based self-assembly of chiral plasmonic nanostructures with tailored optical response," *Nature*, vol. 483, no. 7389, p. 311, 2012.

[115] J. M. Slocik, A. O. Govorov, and R. R. Naik, "Plasmonic circular dichroism of peptide-functionalized gold nanoparticles," *Nano Letters*, vol. 11, no. 2, p. 701, 2011.

[116] W. H. Greub, *Linear algebra*. Springer Science & Business Media, Heidelberg, 2012.

[117] W.-K. Tung, *Group theory in physics: an introduction to symmetry principles, group representations, and special functions in classical and quantum physics*. World Scientific Publishing Company, Singapore, 1985.

[118] A. Lakhtakia, V. K. Varadan, and V. V. Varadan, *Time-harmonic electromagnetic fields in chiral media*. Springer, London, 1989.

[119] B. Luk'yanchuk, N. I. Zheludev, S. A. Maier, N. J. Halas, P. Nordlander, H. Giessen, and C. T. Chong, "The Fano resonance in plasmonic nanostructures and metamaterials," *Nature*

Materials, vol. 9, no. 9, p. 707, 2010.

[120] M. F. Limonov, M. V. Rybin, A. N. Poddubny, and Y. S. Kivshar, "Fano resonances in photonics," *Nature Photonics*, vol. 11, no. 9, p. 543, 2017.

[121] B. Luk'yanchuk, A. Miroshnichenko, and Y. S. Kivshar, "Fano resonances and topological optics: an interplay of far-and near-field interference phenomena," *Journal of Optics*, vol. 15, no. 7, p. 073001, 2013.

[122] B. Gallinet and O. J. Martin, "Influence of electromagnetic interactions on the line shape of plasmonic Fano resonances," *ACS Nano*, vol. 5, no. 11, p. 8999, 2011.

[123] B. Gallinet and O. J. Martin, "Ab initio theory of Fano resonances in plasmonic nanostructures and metamaterials," *Physical Review B*, vol. 83, no. 23, p. 235427, 2011.

[124] V. Flauraud, G. D. Bernasconi, J. Butet, M. Mastrangeli, D. T. Alexander, O. J. Martin, and J. Brugger, "Mode evolution in strongly coupled plasmonic dolmens fabricated by templated assembly," *ACS Photonics*, vol. 4, no. 7, p. 1661, 2017.

[125] R. Singh, I. A. Al-Naib, M. Koch, and W. Zhang, "Sharp Fano resonances in THz metamaterials," *Optics Express*, vol. 19, no. 7, p. 6312, 2011.

[126] V. Fedotov, M. Rose, S. Prosvirnin, N. Papasimakis, and N. Zheludev, "Sharp trapped-mode resonances in planar metamaterials with a broken structural symmetry," *Physical Review Letters*, vol. 99, no. 14, p. 147401, 2007.

[127] A. Y. Alfakih, A. Khandani, and H. Wolkowicz, "Solving Euclidean distance matrix completion problems via semidefinite programming," *Computational Optimization and Applications*, vol. 12, no. 1-3, p. 13, 1999.

[128] H. Wolkowicz, R. Saigal, and L. Vandenberghe, *Handbook of semidefinite programming: theory, algorithms, and applications*. Springer Science & Business Media, Heidelberg, 2012.

[129] R. Priemer, *Introductory signal processing*. World Scientific Publishing Company, Singapore, 1990.

[130] E. Hecht and A. Zajac, *Optics*. Addison-Wesley, Massachusetts, 1974.

[131] D. G. Rabus, *Integrated ring resonators*. Springer, Heidelberg, 2007.

[132] I. Teraoka and S. Arnold, "Theory of resonance shifts in TE and TM whispering gallery modes by nonradial perturbations for sensing applications," *Journal of the Optical Society of America B*, vol. 23, no. 7, p. 1381, 2006.

[133] F. Ruesink, H. M. Doeleman, R. Hendrikx, A. F. Koenderink, and E. Verhagen, "Perturbing open cavities: Anomalous resonance frequency shifts in a hybrid cavity-nanoantenna system," *Physical Review Letters*, vol. 115, no. 20, p. 203904, 2015.

[134] S. Shopova, R. Rajmangal, S. Holler, and S. Arnold, "Plasmonic enhancement of a whispering-gallery-mode biosensor for single nanoparticle detection," *Applied Physics Letters*, vol. 98, no. 24, p. 243104, 2011.

[135] R. Drever, J. L. Hall, F. Kowalski, J. Hough, G. Ford, A. Munley, and H. Ward, "Laser

phase and frequency stabilization using an optical resonator," *Applied Physics B*, vol. 31, no. 2, p. 97, 1983.

[136] A. Hammiche, R. Webb, and I. Wilson, "A scanning tunnelling microscopy study of thin gold films evaporated on silicon," *Vacuum*, vol. 45, no. 5, p. 569, 1994.

[137] P. Malinskỳ, P. Slepička, V. Hnatowicz, and V. Švorčík, "Early stages of growth of gold layers sputter deposited on glass and silicon substrates," *Nanoscale Research Letters*, vol. 7, no. 1, p. 241, 2012.

[138] J. Ju, Y. Yamagata, and T. Higuchi, "Thin-film fabrication method for organic light-emitting diodes using electrospray deposition," *Advanced Materials*, vol. 21, no. 43, p. 4343, 2009.

[139] Q. Xi, X. Chen, D. G. Evans, and W. Yang, "Gold nanoparticle-embedded porous graphene thin films fabricated via layer-by-layer self-assembly and subsequent thermal annealing for electrochemical sensing," *Langmuir*, vol. 28, no. 25, p. 9885, 2012.

Acknowledgments

This dissertation would not be possible without the work of many people sharing ideas, discussing the problems, presenting the results, and preparing the strategy for the next steps. During the time I spent for my PhD, I profited from many contributions of other people, scientifically and socially, to whom I want to express my sincere gratitude here.

First and foremost, I want to express my deepest gratitude to Prof. Dr. Carsten Rockstuhl, who guided me patiently, and for his wonderful support and stimulus throughout my time as his PhD student. He offers a great scientific guidance as well as friendly atmosphere in the group. He was also teaching me other aspects of life, such as lasertag. Thanks for being a great supervisor during my PhD time!!

Secondly, I also want to give my acknowledgement to Prof. Dr. Heinz Kalt for agreeing to be my co-referee and for a great collaboration. Thanks a lot!

Next, I want to thank Dr. Ivan Fernandez-Corbaton, who guide me whenever I have analytical problems and for his deep insight into the problems I had faced. Thanks for your guidance, Ivan!

Special thanks also go to Andreas Vetter, Aimi Abbas, and Karim Mnasri for their endless support, both academically and personally. Thanks for the accomodation when I was in Switzerland (Andreas) or when I was too lazy to go back home (Karim and Aimi), and especially for the great food the three of you cooked for me. It was really delicious!

I also want to express my gratitude to Carolin Klussmann, Stefan Nanz, and Yannick Augenstein, for the great friendships throughout my Ph.D. You three are wonderful friends!

My gratitude also goes to two people who act as my "big sisters" in Germany. Thanks a lot Dr. Maureen Linggarsari Nietiadi and Dr. Hui-Hsin Hsiao for all the good time and the advices.

I also want to give my thanks to the member of AG Rockstuhl for providing a nice, wonderful atmosphere, Specifically, I also want to mention the members of the group during my time there. Thanks a lot Xavier Garcia-Santiago, Aso Rahimzadegan,Marvin Müller, Martin Fruhnert, Ismail Abdelrahman, Steffen Alexander Schmid, Rasoul Alaee, Evgeniia Slivina, Florian Graf, Taavi Repan, Youngsun Yun, Patrizia Stehle, Achim Groner, Aristeidis Lamprianidis, Julian Münzberg, Changhyoup Lee, Karolina Slowik, Dominik Beutel, Joel Macht, Fernando Negredo, Keya Zhou, Jens Opperman, Christina Ioannou, Mirko Göddel, and Jakob Straubel for your help and support during my Ph.D time. I also want to give special thanks to the TFP secretaries, Evmarie Schwartz, Edith Herzog, and Rita Jung for their assistance regarding administrative issues. What a wonderful group!

Next, I also want to mention people from AG Kalt, especially Fabian Ruf, Simon Wowska, Tobias Siegle, Sarah Krammer, Jonas Schundelmeier, and Lwytiko Mwakyusa for their hospitality and friendship through my PhD time. Thanks for a lot of nice memories!

Special thanks also go to Karlsruhe School of Optics and Photonics for their support through my Ph.D and for a great time when I did an internship there. Stefanie Peer for her administrative support and also for Miriam Sonnenbichler, Claudia Alamo Masanet, David Kurzmann, and Denica Angelova-Jackstadt for being great officemates during my internship there. I enjoyed working together with all of you!

I also want to thanks Dr. Danays Kunka for being a great mentor and for her care and support during my PhD time. Thanks a lot Danays!

I also want to express my gratitude to Prof. Dr. Olivier Martin for hosting me in his group during my research stay at EPFL, Switzerland, and for the insightful discussion on Fano resonances. Special thanks go to Kevin Müller, Dr. Toralf Scharf, Karim Achouri, Hsiang-Chu Wang, Michail Symeonidis, Debdatta Ray, Mintae Chung, Dr. Christian Santschi, Jeonghyeon Kim, Marco Riccardi, Dr. Jeremy Butet, Dr. Madasamy Thangamuthu, and Gabriel Bernasconi for great discussions and activities we did together during my time there. I also want to thanks Rossella Grillo and Thomas Bürgi from the University of Geneva for the collaboration we did together.

Next, my thanks also go to Dr. Johannes Freudenreich from Helmholtz Association and the members of Helmholtz Juniors 2017-2018 for providing me with a lot of knowledge and organizational experiences. Special thanks go to Kristin Burmeister (Geomar) for being a great leader of the event group and for her support when I first joined the group, Jörg Ackermann (FZJ), Konstantin Kuhne and Xu Xiaomo (HZDR), Kevin Becker (HZI), Daniel Meza (HZB), Khwab Sanghvi (DKFZ), Vasiliki Anastasopoulou and Giulia Caglio (MDC), and Lennart Bock (IPP München) for great time and discussions about many things in life. Special thanks also given to Mirjana Gusic (HMGU) for her time guiding me through München. I was really lucky to be part of this awesome group!

My gratitude also goes to Karlsruhe House of Young Scientists (KHYS) for the fund through International collaboration package grant and the travel support during my time as a representative of KIT in Helmholtz Juniors. I want to express my thanks also to Verlag Der Tagesspiegel for the support through Young Changers-Scholarship 2018.

I want to mention my parents and my three sisters for their support through my life, which makes me what I am today. Thanks a lot for everything!

Lastly, I want to mention people from PPI Karlsruhe and Persekutuan Karlsruhe for their help. Special thanks go to Heru Salim, Rikco Hartanto, George Sebastian Tay, Jo Jevon Nova Dinata and Lukas Hadiyanto Winata for their help and assistance.